arXiv:0909.5691v1 [astro-ph.CO] 30 Sep 2009

Mon. Not. R. Astron. Soc. **000**, 000–000 (0000) Printed 1 October 2009 (MN LaTeX style file v1.4)

The TexOx-1000 redshift survey of radio sources I: the TOOT00 region

Eleni Vardoulaki[1]*, Steve Rawlings[1], Gary J. Hill[2], Tom Mauch[1], Katherine J. Inskip[3], Julia Riley[4], Kate Brand[1], Steve Croft[5], Chris J. Willott[6]

[1] *Astrophysics, Denys Wilkinson Building, Keble Road, Oxford, OX1 3RH, UK*
[2] *University of Texas at Austin, 1 University Station, C1402, Austin, TX 78712, USA*
[3] *Max-Planck-Institut fur Astronomie, Konigstuhl 17, D-69117 Heidelberg, Germany*
[4] *Cavendish Astrophysics, Department of Physics, Madingley Road, Cambridge, CB3 OHE, UK*
[5] *University of California, Berkeley, Dept. of Astronomy, 601 Campbell Hall #3411, Berkeley, CA 94720, USA*
[6] *Herzberg Institute of Astrophysics, National Research Council, 5071 West Saanich Rd, Victoria, BC V9E 2E7, Canada*

1 October 2009

ABSTRACT

We present optical spectroscopy, near-infrared (mostly $K-$band) and radio (151-MHz and 1.4-GHz) imaging of the first complete region (TOOT00) of the TexOx-1000 (TOOT) redshift survey of radio sources. The 0.0015-sr (~ 5 deg^2) TOOT00 region is selected from pointed observations of the Cambridge Low-Frequency Survey Telescope at 151 MHz at a flux density limit of $\simeq 100$ mJy, $\sim$ 5-times fainter than the 7C Redshift Survey (7CRS), and contains 47 radio sources. We have obtained 40 spectroscopic redshifts ($\sim 85\%$ completeness). Adding redshifts estimated for the 7 other cases yields a median redshift $z_{\rm med} \sim 1.25$. We find a significant population of objects with FRI-like radio structures at radio luminosities above both the low-redshift FRI/II break and the break in the radio luminosity function. The redshift distribution and sub-populations of TOOT00 are broadly consistent with extrapolations from the 7CRS/6CE/3CRR datasets underlying the SKADS Simulated Skies Semi-Empirical Extragalactic Database, S^3-SEX.

Key words: galaxies: active – galaxies: evolution – galaxies: formation – galaxies: jets – galaxies: luminosity function

1 INTRODUCTION

Radio observations of Active Galactic Nuclei (AGN) reveal some of the complexity of the AGN phenomenon. A central black hole accretes matter through an accretion disk, which along the plane of the disk is hidden by a dusty and gas-rich torus. Radio emission emerges from the immediate vicinity of the black hole through the synchrotron process (e.g. from the base of jets) and potentially other processes like optically thin bremsstrahlung from a slow, dense disk wind (Blundell & Kuncic 2007). Powerful jets can propagate to large scales and radio telescopes enable the study of these 'radio-loud' objects in detail, which are believed to live from $\lesssim 10^4$ yr for small GHz-peaked sources to $\sim 10^{7-8}$ yr for larger steep-spectrum sources. Best et al. (2005) found that 25% of the most massive galaxies show radio-loud AGN activity, and argued that such AGN activity is constantly re-triggered. Radio sources seem to have a 'duty-cycle', i.e. a recurrent radio-loud AGN activity, which is believed to play an important role in bal-

---

* Email: eleniv@astro.ox.ac.uk

© 0000 RAS

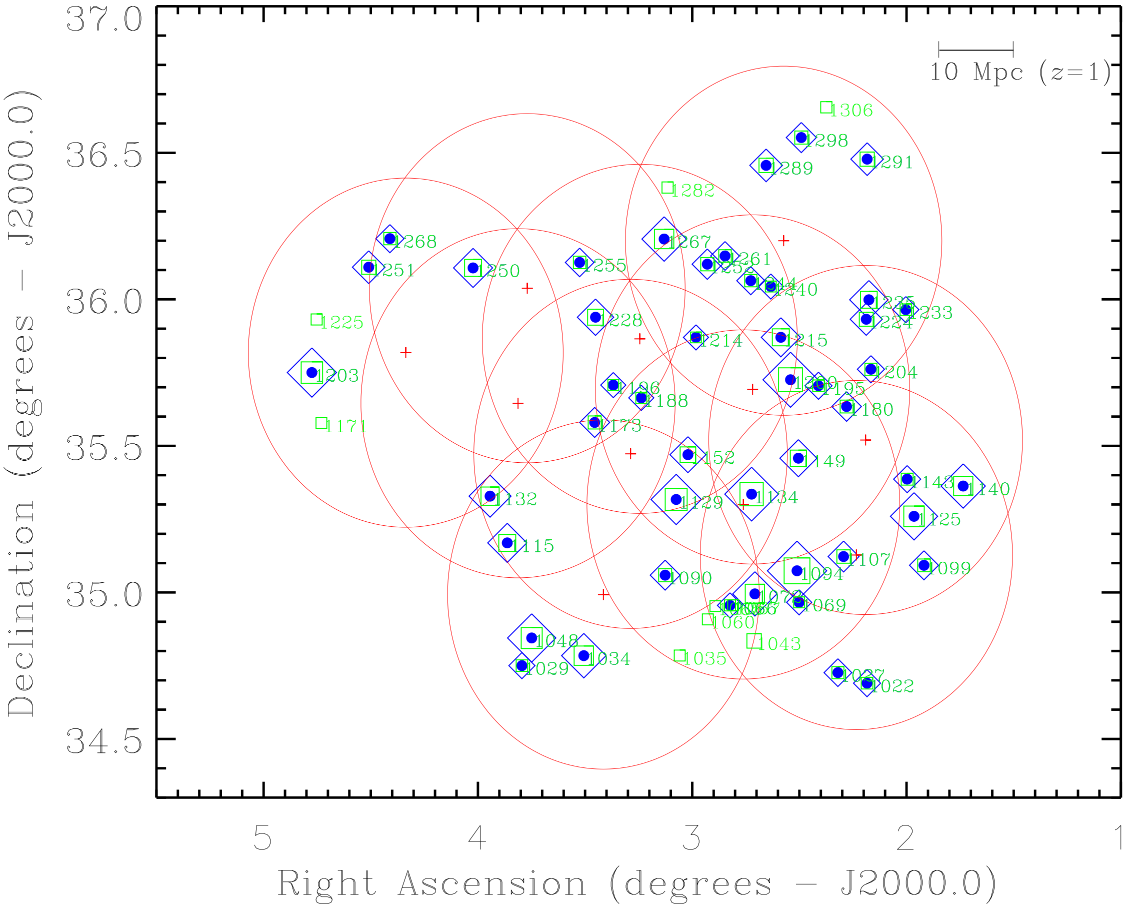

Figure 1. Sky area of the TOOT00 region with the bar showing the angle corresponding to a proper distance of 10 Mpc observed at redshift $z = 1$. Symbols: blue diamonds show the 47 TOOT00 radio sources, where their size is proportional to the base-10 logarithm of the 1.4-GHz flux density of each object; objects detected in the 74-MHz VLSS survey (Cohen et al. 2007) are indicated with a solid blue circle. Green boxes represent the 56 objects of the 7C sample in the same sky area with $S_{151\mathrm{MHz}} > 95$ mJy; their size is proportional to the base-10 logarithm of the 151-MHz flux density of each object. The 11 A-array 1.4-GHz VLA pointings are shown as red crosses '+', where the circles around them have a radius of 35.7 arcmin in order to include all the TOOT00 objects, and corresponding roughly to the 32-arcmin-diameter primary beam of the VLA. The 9 'off-edge' objects described in Section 2 are: TOOT00_1306 at 00 11 50.33 +36 39 19.34 with $S_{151\mathrm{MHz}}$ = 0.11 Jy, TOOT00_1043 at 00 13 12.77 +34 50 04.78 with $S_{151\mathrm{MHz}}$ = 0.21 Jy, TOOT00_1067 at 00 13 42.51 +34 57 22.04 with $S_{151\mathrm{MHz}}$ = 0.10 Jy, TOOT00_1065 at 00 14 06.90 +34 57 12.28 with $S_{151\mathrm{MHz}}$ = 0.097 Jy, TOTO00_1060 at 00 14 16.62 +34 54 28.83 with $S_{151\mathrm{MHz}}$ = 0.10 Jy, TOOT00_1035 at 00 14 53.67 +34 47 04.59 with $S_{151\mathrm{MHz}}$ = 0.10 Jy, TOOT00_1282 at 00 15 28.61 +36 22 53.84 with $S_{151\mathrm{MHz}}$ = 0.11 Jy, TOOT00_1171 at 00 23 15.84 +35 34 39.66 with $S_{151\mathrm{MHz}}$ = 0.098 Jy, TOOT00_1225 at 00 23 28.63 +35 55 52.86 with $S_{151\mathrm{MHz}}$ = 0.10 Jy.

ancing the energy losses from hot gas that surrounds massive elliptical galaxies (Best et al. 2006). This is done by re-heating the cooling gas inside the galaxy halo, in a way that provides a self-regulating feedback mechanism capable of controlling the rate of growth of galaxies (Tabor & Binney 1993). The 'duty-cycle' or, in other words the lifetime of radio sources, differs according to radio-source type.

Fanaroff & Riley (1974) were the first to divide radio sources according to radio structure and radio luminosity: FRIs are bright close to the core whereas FRIIs are edge-brightened radio sources. The radio luminosity divide is at $\log_{10}(L_{178\mathrm{MHz}}/\mathrm{WHz}^{-1}\mathrm{sr}^{-1}) \approx 25$ ($H_0 = 50$ km s^{-1}Mpc^{-1}, $\Omega_\mathrm{M} = 1$ and $\Omega_\Lambda = 0$)†; above this value lie the FRIIs, and below that the FRIs. Kaiser & Best (2007a, 2007b) suggest that all sources start out with an FRII structure, and the final form they take depends on the host galaxy. On the other hand, Parma et al. (2002) studied a sample of FRI and FRII radio sources with a double-double

---

† This corresponds to $\log_{10}(L_{151\mathrm{MHz}}/\mathrm{WHz}^{-1}\mathrm{sr}^{-1}) \approx 25$ in our adopted cosmology ($H_0 = 70$ km s^{-1}Mpc^{-1}, $\Omega_\mathrm{M} = 0.3$ and $\Omega_\Lambda = 0.7$ for an $\alpha \simeq 0.8$ radio source) at the typical redshift ($z \simeq 0.1$) of objects defining the FRI/FRII division of the Fanaroff & Riley (1974) study.

structure and argued that it is unlikely that many FRIIs evolve to FRIs.

Bird et al. (2008) argue that the average FRII-type (Fanaroff & Riley 1974) radio-source lifetimes are $\sim 1.5 \times 10^7$ yr with a duty cycle[‡] ~ 0.02 (for $\sim 8 \times 10^8$ yr time off). Parma et al. (2002) claim that the ages of FRIs are $\sim$ 5-10 times larger than the ages of FRII radio sources, consistent with the Best et al. (2005) inference that massive galaxies are active in either an FRI or FRII phase roughly 25% of the time.

The difference in FRI and FRII radio-source lifetimes may be linked to studies of HI gas as probe of the host environment of these objects. Emonts et al. (2008) studied a sample of nearby FRI radio sources up to redshift of $z \sim 0.04$ and a sample of FRIIs with $z \lesssim 0.06$, and found that different types of radio sources contain different large-scale HI properties; the HI detection rate in FRIIs is significantly higher than the detection rate for the FRI radio galaxies. These findings suggest a different triggering history for different types of radio sources: FRIIs are likely triggered by galaxy mergers and collisions as the large-scale HI is often distributed in tail- or bridge-like structures; FRI radio sources are likely fed in other ways, such as steady accretion from a hot IGM.

Radio sources can be observed throughout different cosmic epochs. Studies of radio galaxies and radio-loud quasars (RLQ) can determine the evolution of the radio-source population by defining the Radio Luminosity Function (RLF; e.g. Dunlop & Peacock 1990; Rawlings, Eales & Lacy 2001; Willott et al. 2001), i.e. the number density of sources per co-moving volume. The sharp decline in the (co-moving) space density of radio sources from epochs corresponding to $z \sim 2.5$ to those corresponding to $z \sim 0$ was inferred from early counts of radio sources by Longair (1966). By combining constraints from radio source counts with surveys of bright high-radio-frequency-selected samples, using spectroscopic and estimated redshifts, Dunlop & Peacock (1990) were the first to map out the cosmic evolution of this population in any detail. They claimed to detect a measurable drop, or redshift-cutoff, in the space density of sources at $z \gtrsim 2.5$. Returning to this problem with virtually-complete spectroscopic redshift information on low-radio-frequency-selected samples, Willott et al. (2001) measured a RLF in rough agreement with that of Dunlop & Peacock, but differing in important aspects such as a factor ~ 2 lower normalisation at $z \sim 2.5$. Such seemingly subtle differences, attributable largely to biases in the redshift estimates used by Dunlop & Peacock, removed any convincing evidence for the redshift cut-off, a finding in agreement with work focused on the most luminous steep-spectrum radio sources (Jarvis et al. 2001).

It seems clear, therefore, that spectroscopic redshift surveys of radio sources are of the utmost importance in making robust measurements of the cosmic evolution of the RLF at high redshift. It is also clear that, as emphasised by Willott et al. (2001), the next generation of radio source redshift surveys should be carefully targeted on those objects which make the dominant contribution to the radio luminosity density Π[§]. Evaluated as a function of cosmic time t, $\Pi(t)$ encodes the information needed to estimate crucial physical quantities like the quantity of heat, or entropy, radio sources inject into the inter-galactic medium (Yamada & Fujita 2001; Gopal-Krishna & Wiita 2001; Rawlings 2002). Current estimates of $\Pi(t)$, even at epochs corresponding to the supposedly well-studied redshift range $2 \lesssim z \lesssim 3$, are highly uncertain because they rely on extrapolating from measurements of the most luminous radio sources down a very steep RLF. Robust luminosity density measurements require that space densities are measured for objects much closer to the break in the RLF.

The RLF is often modelled as a broken power law. The break luminosity is close to, but above, the dividing line between the two FR structural classes for the large-scale radio structure of these objects. Willott et al. (1998) found that the break in the RLF for radio-loud quasars is at $\log_{10}(L_{151MHz}/\mathrm{WHz^{-1}sr^{-1}}) \lesssim 27$[¶] ($H_0 = 50$ km s^{-1}Mpc^{-1}, $\Omega_{\mathrm{M}} = 1$ and $\Omega_\Lambda = 0$), while there is no evidence for a decline in the co-moving space density of RLQs at higher redshift than the peak of the RLF at $z \sim 2$. This is important for radio galaxies, since from unified AGN schemes RLQs and radio galaxies are the same objects where the apparent difference in their properties is a result of the orientation of the radio jets (e.g. Antonucci 1993).

Surveys such as the 3CRR, 6CE and 7CRS (Laing, Riley & Longair 1983; Rawlings, Eales & Lacy 2001 and Willott et al. 2003, respectively) were designed in order to study complete, down to a certain flux density limit, spectroscopic samples of radio sources. The goal was to study the RLF. However, at $z > 2$ these surveys are not deep enough to make a good estimate of the density of radio sources close to the RLF break. In order to target the radio-source population responsible for the bulk of the cosmic heating, one needs to study a deeper low-radio-frequency-selected sample around redshift $z \sim 2$. Willott et al. (2001) suggested a new study that would target a large sample (~ 1000) of radio sources selected from the 7CRS survey at a flux density limit of 100 mJy at 151 MHz.

[‡] We define duty cycle as the dimensionless ratio of time active to the sum of time active and dormant.

[§] We define the radio luminosity density by $\Pi = \int\int L_\nu [\mathrm{d}\rho/\mathrm{d}\log_{10} L_\nu]\mathrm{d}(\log_{10} L_\nu)\mathrm{d}\nu$, where $\mathrm{d}\rho/\mathrm{d}\log_{10} L_\nu$ is the co-moving space density (in units of Mpc^{-3}) of radio sources.

[¶] This corresponds to $\log_{10}(L_{151\mathrm{MHz}}/\mathrm{WHz^{-1}sr^{-1}}) \approx 26$ in our adopted cosmology ($H_0 = 70$ km s^{-1}Mpc^{-1}, $\Omega_{\mathrm{M}} = 0.3$ and $\Omega_\Lambda = 0.7$ for an $\alpha \simeq 0.8$ radio source) at the typical redshift ($z \simeq 1$) of the 3CRR/6CR/7CRS datasets.

The TexOx-1000 (TOOT; Hill & Rawlings 2003) survey is the realisation of a hypothetical survey proposed by Willott et al. (2001). The primary aim of the TOOT survey is to measure spectroscopic redshifts for ≈ 1000 radio sources from a low-frequency-selected sample reaching a flux-density limit $S_{151} \sim 0.1$ Jy over several separate sky patches totalling ~ 0.03 sr (see Tables 1 & 2 of Hill & Rawlings 2003, for details on the TOOT regions and status of the survey). Another objective of the TOOT survey was to target radio sources at redshift $z \sim 2$ where the density of the radio source population is at its maximum (e.g. Rawlings 2003).

In this paper we study the $00^{\rm h}$ targeted sky area of the TexOx-1000, hereafter TOOT00, which includes 47 radio sources with a flux density limit of $\simeq 100$ mJy at 151 MHz. In Section 2 we present the 151 MHz and 1.4 GHz radio imaging and optical spectroscopic and near-infrared (mostly $K-$band) imaging data on the TOOT00 sample. In Section 3 we present a basic analysis on the TOOT00 sample: a comparison of spectroscopic and photometric redshifts in Section 3.1; an analysis of radio spectral indices in Section 3.2; an investigation of relationships between radio structure, radio luminosity and redshift in Section 3.3; and a discussion of the quasar fraction in Section 3.4. In Section 4 we present the redshift distribution of the TOOT00 sample (Figure 7) and compare it to simulations of the radio sky from the SKADS Simulated Skies Semi-Empirical Extragalactic Database ($\mathrm{S^3}$-SEX; Wilman et al. 2008). In Section 5 we make some concluding remarks. In the Appendix A we present notes on each object, photometry in the optical and near-IR, as well as a figure with near-IR/radio overlays, optical spectroscopy and Spectral Energy Distributions (SEDs) for the 47 TOOT00 objects.

We use J2000.0 positions and the convention for all spectral indices, α, that flux density $S_\nu \propto \nu^{-\alpha}$, where ν is the observing frequency. We assume throughout a low-density, Λ-dominated Universe in which $H_0 = 70$ km s^{-1}Mpc^{-1}, $\Omega_{\rm M} = 0.3$ and $\Omega_\Lambda = 0.7$.

2 DATA AND OBSERVATIONS

The 7C radio source survey was performed using the Cambridge Low Frequency Synthesis Telescope (CLFST) operating at 151 MHz with a resolution of 70×70 cosec(Dec) arcsec^2. General principles of its operation are described by Rees (1990). The instrument was used to survey about one hundred fields north of declination 30 degrees and well away from the galactic plane. The rms noise and hence the limiting flux density of the survey varies both within any one field and between different fields owing to beam distortion, primary beam and ionospheric effects. Some data on individual fields and groups of fields have been published in various papers (see Riley, Waldram & Riley 1999 and references therein). The construction of a final unified catalogue is described in Hales et al. (2007) and is available via the 7C website[‖]. The final 7C catalogue lists 43683 sources over an area of about 1.7 sr.

The TOOT00 radio-source sample was selected from the 7C survey to include sources with peak flux densities above $\simeq 100$ mJy at 151 MHz; the final lower limit was 95 mJy. The area studied is illustrated in Figure 1; 56 sources lie in this area. All of the TOOT00 objects were observed with the VLA, in A and B configurations at 1.4 GHz, where 11 pointings were used to cover the TOOT00 area (Figure 1). The A-array observations were performed on 12 August 1999 and the B-array on 25 June 2002. To avoid excessive bandwidth smearing these observations were made using seven 3.125-MHz channels centred on 1.370 GHz plus seven 3.125-MHz channels centred on 1.444 GHz. Following standard reduction procedures in AIPS we synthesised maps of all our objects using both separate and combined A- and B-array visibilities. In this paper we present B-array images of the TOOT00 radio sources (Figure A1 in Appendix A), unless the A-array maps reveal important information about the radio structure.

In the final sample selection all sources with flux densities $S_{\rm 151MHz} > 220$ mJy were included, as well as a sub-set of sources with 95 mJy $< S_{\rm 151MHz} \leq$ 220 mJy, close enough to the VLA pointing centres to have good maps in the VLA A-array observations. The 9 sources excluded are characterised as 'off-edge' objects and are typically ~ 30 arcmin away from the centre of the positions where the VLA was pointed. These are faint enough that no reasonable map could be made. Note that this introduces a selection bias against fainter radio sources in the TOOT00 survey. The final TOOT00 sample includes 47 radio sources.

The sky area of TOOT00 was measured using a Monte-Carlo approach: random numbers were generated, uniform in RA and with a $\sin\theta$ distribution in Dec, within a rectangle enclosing the all 56 original TOOT00 sources. We tested whether the randomly selected points lay within 35.7 arcmin (see Figure 1) of any of the 11 VLA pointing positions. The ratio of points passing this test to the total number of random points (0.68) was multiplied by the sky area of the rectangle. The result is 0.0015 sr or ~ 5.0 deg^2.

Table 1 gives the basic radio data on the 47 TOOT00 radio sources. The flux densities used subsequently are shown in bold, and were chosen accord-

---

[‖] *http://www.mrao.cam.ac.uk/surveys/7C* ing to the following criteria: (i) if the integrated flux density has a significantly larger value than the peak flux density and is not the result of confusion, we use the former and (ii) in the case of a compact radio source we always use the peak flux density. The radio spectral indices $\alpha_{151\mathrm{MHz}}^{1.4\mathrm{GHz}}$ were calculated using the 1.4 GHz (NRAO/VLA Sky Survey - NVSS; Condon et al. 1998) and 151 MHz (7C) flux densities for the TOOT00 sources. We also obtained 74 MHz flux densities for 12 out of 47 TOOT00 radio sources from the VLA Low-frequency Sky Survey (VLSS; Cohen et al. 2007). The VLSS has a resolution of 80 arcsec (FWHM), a noise level of ≈ 0.1 Jy beam^{-1} and a typical catalogue point-source detection limit of 0.7 Jy beam^{-1}; the 74 MHz maps are available for searching for fainter sources. The angular sizes of the TOOT00 sources were measured from the VLA (A or B configuration) images. We use our VLA data and the Owen & Laing (1989) radio-source classification to place our objects in four categories: Classical Double (CD), Fat Double (FD), Twin Jet (TJ) and Compact (COM) radio sources. CDs correspond to FRIIs where there is at least one bright hotspot at the ends of the structure in both high- and low-resolution radio maps; FDs represent FRI/II division objects, where the radio structure is more diffuse on the high resolution radio maps than in the case of CDs, and no compact hotspot-like features are visible in the A-array radio map; TJs are FRI type radio sources which are brightest near the centre of the sources; COM radio sources don't show any evidence of extended radio emission on $\gtrsim$ 5-arcsec scales.

Optical spectroscopic observations were undertaken with the ISIS spectrometer on the William Herschel Telescope (WHT**) in August 2000, 2004, 2006 and 2009 (see Table 2); TOOT00_1134 was observed with the Marcario Low Resolution Spectrograph (LRS) on the Hobby-Eberly Telescope (HET††; Hill et al. 1998). All ISIS observations used the R158R and R158B gratings with the beam split using the 5400-Å dichroic; the R158B grating was used for the blue arm, providing 1.62 Å/pixel and 0.2 arcsec/pixel scales with the EEV12 detector. For the August 2000 observing run the R158R grating was used with the TEK4 detector on the red arm, which gave 2.90 Å/pixel and 0.36 arcsec/pixel scales. For the August 2004 and August 2006 observing runs the red MARCONI detector was used, which provides similar intrinsic spatial and spectral scales to the blue EEV12 detector. For the August 2009 observing run the EEV12 was used alongside the REDPLUS detector: after 3×2 (spectral $\times$ spatial) binning in the blue, and 3×1 binning in the red, this gave gave ≈ 5Å/pixel and $\approx 0.44/0.22$ (blue/red) arcsec/pixel scales. The LRS was used with a 2-arcsec-wide slit and 300 l/mm grism giving a resolution of 16.7 Å and coverage of 4150 to 10100 Å. Observations and data analysis followed the standard methods described by Rawlings, Eales & Lacy (2001). We offset from nearby bright stars to either optical or radio positions, choosing the position angle (PA) of the slit either on the basis of encompassing companion optical objects or to line up with the radio axis. All the targets were observed below an air mass of 1.2, and all but two were observed below an air mass of 1.1. All the data presented here were taken in photometric conditions with the seeing close to 1 arcsec. In most cases spectral features, emission lines and/or spectral breaks were detected, and the reduced 1D spectra are presented in Figure A1. For cosmetic purposes, most of the spectra have been smoothed by replacing the value of each spectral bin by the average of the values in the bin and its two neighbours. All measurements from the spectra were made prior to this process, and the results are tabulated in Table 4.

Multi-colour optical images from the INT Wide Field Camera data were obtained as part of the Oxford-Dartmouth 30-Degrees (ODT) survey (see MacDonald et al. 2004). The ODT survey is a multiband imaging survey, with limiting depths (5σ, $2''$ aperture Vega magnitudes) of $U = 25.3$, $B = 26.2$, $V = 25.7$, $R = 25.4$, $i' = 24.6$, $Z = 21.9$ and $K = 18.5$. In the case where ODT data were unavailable, estimates of the photometry were made from the optical spectrum of the object when available.

Near-IR imaging in the $K-$band was obtained at the United Kingdom Infrared Telescope UKIRT‡‡ by using either UIST (Howatt et al. 2004) in January 2003 or UFTI (the UKIRT Fast–Track Imager; Roche et al. 2002) in July 2000, December 2000, January 2001 and 2002 and September 2004. Further infrared observations of a $z \sim 1$ TOOT00 sub-sample were carried out at the UKIRT in 2003 with UIST and in 2004 with UFTI with typical exposures of $\sim$ 9-18 min; we term this the 'Inskip' sub-sample. UIST is a 1–5 μm imager-spectrometer with a 1024×1024 InSb array. The instrument is designed to switch quickly and accurately between imaging and spectroscopic modes. We used the imaging mode, where two plate scales are available, 0.12 arcsec / pixel or 0.06 arcsec / pixel,

---

[$\star\star$] The WHT is operated by the Isaac Newton Group of Telescopes (ING), at the Roque de Los Muchachos Observatory in La Palma, Spain.

[$\dagger\dagger$] The Marcario Low Resolution Spectrograph is a joint project of the Hobby - Eberly Telescope partnership and the Instituto de Astronomia de la Universidad Nacional Autonoma de Mexico. The Hobby - Eberly Telescope is operated by McDonald Observatory on behalf of The University of Texas at Austin, the Pennsylvania State University, Stanford University, Ludwig-Maximilians-Universitaet Muenchen, and Georg-August-Universitaet Goettingen.

[$\ddagger\ddagger$] The United Kingdom Infrared Telescope is operated by the Joint Astronomy Centre on behalf of the Science and Technology Facilities Council of the U.K.

giving fields of view of 2×2 or 1×1 arcmin^2. UFTI is a 1–2.5 μm camera with a 1024 × 1024 HgCdTe array and a plate scale of 0.091 arcsec / pixel, which gives a field of view of 92 arcsec. Each object in the 'Inskip' sub-sample was observed in the J, H and K infrared wavebands. The K-band observations were generally of ~ 2 hours duration in total. J-band observations were typically 18-63 minutes, and H-band observations typically 18-72 minutes (depending on source redshift). Table A1 (see Appendix A) shows the photometric data used to calculate photometric redshifts, and Table A2 shows complete photometry on each object.

All near-IR observations used a nine-point jitter pattern, with offsets of roughly 10 arcsec between each 1 minute exposure. The observational data were dark subtracted, and masked for bad pixels. A first-pass sky flat-field image was created from groups of roughly 60–100 consecutive frames of data, which were combined and median filtered. This accounted for the majority of the pixel-to-pixel variations of the chip, but some larger-scale illumination gradients remained, due to the changing position of the telescope through the course of the night. Smaller blocks of 9–18 first-pass flat-fielded images were similarly combined to create residual sky flat-field images, allowing us to remove the remaining variations. The first-pass flat-fielded data were used to generate masks for any bright objects in the images, and a repeat of the whole process allowed the data to be cleanly flat-fielded without any contamination from stars or galaxies.

The flat-fielded data for each source were sky-subtracted and combined using the IRAF package DIMSUM, creating a final mosaiced image of approximately 115×115 arcsec^2[§§], which was flux calibrated using observations of UKIRT faint standard stars. Astrometry corrections were performed to the finalised near-IR images using the package KARMA. Photometry was carried out within apertures ranging from 3 to 9 arcsec in diameter, using the IRAF routine APPHOT and a single sky annulus. All sources have been corrected for galactic extinction using the $E(B-V)$ for the Milky Way from the NASA Extragalactic Database (NED) and the parametrised galactic extinction law of Howarth (1983).

Optical and near-infrared photometric data were used to create SEDs for our objects as shown in Figure A1 (in Appendix A). Seven of our objects do not as yet have spectroscopically-confirmed redshifts. Table 3 summarises the results on the spectroscopic and photometric redshifts, as well as the K magnitude of each object and whether or not the IDs look resolved in the $K-$band. It also gives the Optical (see Section 3.1) and Radio-Optical (see Section 4) classification of the TOOT00 radio sources.

Table 4 presents the measured observed FWHM (in km/s) and EW (in Å) of each line, the radio luminosity at 151 MHz $L_{151\mathrm{MHz}}$ and the flux of the [OII]$_{\lambda3727}$ emission line, since it is the most frequently observed line in the optical in quasars and radio galaxies. In the case where the [OII] line was not present, we measured another narrow line (e.g. [OIII]$_{\lambda5007}$), or any narrow-line profile of the Lyα, [CIV]$_{\lambda1549}$, [CIII] or MgII emission lines. For objects without emission lines in the optical spectrum, a rough estimate of a limit on the [OII] line flux was made as follows: i) for galaxies, i.e. in the case the continuum is clearly strong and stellar, we took a limit of ~ 10 Å which corresponds roughly to lines clearly detectable in a typical spectrum of $z \sim 0.5$ ellipticals, observed with moderate S/N ratio; ii) for fainter objects in which the origin of the continuum is unclear, we supply as a limit the flux of the brightest, but probably spurious, line-like feature in the spectrum adjacent to the estimated location (given the photometric redshift) of the brightest expected narrow line.

[§§] The highest signal-to-noise level is restricted to the central 70×70 arcsec^2.

Table 1. Radio properties of the 47 TOOT00 radio sources; values in bold are those used in the analysis. **Columns 1, 2 & 3** give the name of the object and its 151-MHz radio position from the 7C survey (J2000.0). **Column 4** gives the angular size of the radio source (A- or B-array in line with Figure A1; the characters 'os' denote that the measurement was made from the core to the extent of an one-sided structure). **Columns 5 & 6** give the peak flux density and integrated flux density per beam at 151 MHz respectively. **Column 7** gives the signal-to-noise (S/N) ratio at 151 MHz. **Column 8** gives the flux density at 1.4 GHz as was measured from the B-array VLA maps using IMSTAT task in AIPS; the symbol '+' indicates that the flux density is the sum of two components. **Columns 9 & 10** give the flux density at 1.4 GHz taken from the NVSS survey; the symbol '+' indicates that the flux of each component was measured separately and then added together. **Columns 11 & 12** give the peak flux density and integrated flux density per beam at 74 MHz from the VLSS survey; objects that have flux densities below $\simeq 0.3$ Jy are marked as 2σ limits. Flux densities measured directly from the VLSS maps using the IMSTAT task in AIPS are marked with an 'm'. **Columns 13 & 14** give the spectral index of each object calculated from 1.4 GHz to 151 MHz and 151 MHz to 74 MHz respectively. Fluxes in bold have been used to calculate the spectral index, making use of the NVSS flux density for each one of the radio sources. **Column 15** gives the radio classification (R Cl) of each object (Owen & Laing, 1989): CD stands for classical double, TJ for twin-jet, FD for fat double and COM for a compact radio source.

(1)	(2)	(3)	(4)	(5)	(6)	(7)	(8)	(9)	(10)	(11)	(12)	(13)	(14)	(15)
Name	RA	Dec	θ (arcsec)	S_{151} peak (Jy)	S_{151} integ (Jy)	S/N 151 MHz	$S_{1.4\mathrm{GHz}}$ integ (mJy)	$S_{1.4\mathrm{NVSS}}$ peak (mJy)	$S_{1.4\mathrm{NVSS}}$ integ (mJy)	S_{74} peak (Jy)	S_{74} integ (Jy)	$\alpha_{151}^{1.4}$	α_{74}^{151}	R Cl
TOOT00_1140	00 08 30.81	+35 21 46.98	18	**0.58**	0.53	24.1	92.5	**109.5**	121.1	–	**0.58**$^{\mathrm{m}}$	0.75	0.0	FD
TOOT00_1099	00 09 22.76	+35 05 32.99	$<12^{\mathrm{os}}$	0.14	**0.17**	6.5	16.7	**17.90**	17.90	–	< **0.22**$^{\mathrm{m}}$	1.01	< 0.36	TJ?
TOOT00_1125	00 09 37.58	+35 15 34.76	96	**0.76**	0.76	32.3	86.9	66.10	**93.50**	**1.09**	1.09	0.94	0.40	CD
TOOT00_1143	00 09 47.92	+35 23 11.27	18	**0.12**	0.22	6.1	34.6	**6.400**	9.400	–	< **0.21**$^{\mathrm{m}}$	1.32	< 0.78	FD
TOOT00_1233	00 09 54.04	+35 57 53.41	<6	**0.11**	0.09	4.5	54.1	**51.20**	51.20	–	< **0.20**$^{\mathrm{m}}$	0.34	< 0.84	COM?
TOOT00_1022	00 10 37.58	+34 41 25.24	<7	**0.12**	0.15	6.4	15.5	**15.60**	15.60	–	**0.33**$^{\mathrm{m}}$	0.92	1.42	COM
TOOT00_1204	00 10 40.70	+35 45 41.40	17	**0.12**	0.12	6.1	15.2	19.90	**31.30**	–	< **0.23**$^{\mathrm{m}}$	0.60	< 0.91	FD
TOOT00_1235	00 10 45.45	+35 59 54.58	<6	**0.34**	0.34	20.2	101.9	**99.30**	99.30	–	< **0.24**$^{\mathrm{m}}$	0.55	< -0.49	COM?
TOOT00_1224	00 10 48.54	+35 55 55.46	<6	**0.19**	0.24	11.1	31.2	**32.60**	32.60	–	< **0.20**$^{\mathrm{m}}$	0.79	< 0.07	COM
TOOT00_1291	00 10 51.82	+36 28 42.19	63	**0.20**	0.20	9.7	25.5	23.50	**31.60**	–	< **0.22**$^{\mathrm{m}}$	0.83	< 0.13	CD?
TOOT00_1107	00 11 13.06	+35 07 20.77	25	**0.17**	0.17	9.6	5.71	**5.700**	5.700	–	< **0.16**$^{\mathrm{m}}$	1.52	< -0.09	TJ
TOOT00_1180	00 11 13.21	+35 38 03.49	15	**0.15**	0.11	7.8	16.0	**15.80**	15.80	–	< **0.16**$^{\mathrm{m}}$	1.01	< 0.09	CD?
TOOT00_1027	00 11 17.57	+34 43 34.64	<6	**0.13**	0.11	6.3	656.8	**664.3**	664.3	–	< **0.22**$^{\mathrm{m}}$	-0.73	< 0.74	COM
TOOT00_1195	00 11 52.55	+35 42 18.51	49	**0.12**	0.10	4.8	10.0	10.70	**15.10**	–	< **0.26**$^{\mathrm{m}}$	0.93	< 1.08	CD
TOOT00_1069	00 12 12.51	+34 57 58.20	10	**0.10**	0.09	2.8	3.89	**3.600**	3.600	–	< **0.17**$^{\mathrm{m}}$	1.49	< 0.74	COM?
TOOT00_1094	00 12 16.36	+35 04 25.82	<7	**2.30**	2.21	56.3	242.8	**248.0**	248.0	**3.37**	3.37	1.00	0.54	COM
TOOT00_1149	00 12 17.97	+35 27 28.60	26	**0.30**	0.27	12.7	17.3	27.70	**29.50**	–	**0.26**$^{\mathrm{m}}$	1.04	-0.20	TJ
TOOT00_1298	00 12 24.25	+36 33 07.32	16	**0.16**	0.14	7.0	29.1	27.70	**30.40**	–	**0.40**$^{\mathrm{m}}$	0.75	1.28	TJ
TOOT00_1200	00 12 31.33	+35 43 32.28	27	1.56	**1.59**	51.6	260.7	226.3	**272.4**	**2.60**	2.60	0.79	0.69	CD
TOOT00_1215	00 12 46.06	+35 52 13.70	15	**0.36**	0.35	14.4	38.3	39.80	**42.80**	**0.64**	0.64	0.96	0.81	TJ?
TOOT00_1240	00 13 01.62	+36 02 37.55	209	0.10	**0.13**	4.0	5.9	5.6	**7.4**$^{+}$	–	< **0.21**$^{\mathrm{m}}$	1.29	< 0.67	CD
TOOT00_1289	00 13 12.32	+36 27 25.61	15	**0.20**	0.17	11.3	21.0	19.80	**21.80**	–	**0.41**$^{\mathrm{m}}$	1.00	1.01	CD
TOOT00_1072	00 13 13.26	+34 59 42.15	27	**0.58**	0.55	21.9	102.6	97.80	**111.1**	**0.89**	0.89	0.74	0.60	CD
TOOT00_1134	00 13 21.09	+35 20 07.22	50	**1.37**	1.43	38.5	**119.2**	203.2	237.4	**2.38**	2.75	0.87	0.77	TJ
TOOT00_1244	00 13 29.58	+36 03 49.06	<6	**0.13**	0.10	6.4	32.3	**32.40**	32.40	–	**0.40**$^{\mathrm{m}}$	0.62	1.58	COM
TOOT00_1066	00 13 46.90	+34 57 20.69	19	**0.10**	0.19	2.7	14.8	**14.40**	14.40	–	< **0.18**$^{\mathrm{m}}$	0.87	< 0.82	CD
TOOT00_1261	00 14 06.19	+36 08 52.85	5	**0.14**	0.20	6.2	14.5	**14.20**	14.20	–	< **0.14**$^{\mathrm{m}}$	1.03	< 0.00	CD
TOOT00_1252	00 14 30.42	+36 07 11.83	52^{os}	**0.16**	0.13	7.7	19.3	**18.00**	18.00	–	< **0.19**$^{\mathrm{m}}$	0.98	< 0.24	CD?
TOOT00_1214	00 14 43.35	+35 52 12.64	15^{os}	**0.10**	0.14	4.7	9.4	**11.30**	11.30	–	< **0.19**$^{\mathrm{m}}$	0.98	< 0.90	CD?
TOOT00_1152	00 14 49.99	+35 28 11.78	30	**0.27**	0.24	10.6	35.3	33.80	**38.30**	–	< **0.19**$^{\mathrm{m}}$	0.88	< -0.49	CD
TOOT00_1129	00 15 04.41	+35 19 01.79	15	**1.01**	1.16	44.5	161.5	144.6	**156.6**	**1.45**	1.45	0.84	0.51	CD
TOOT00_1090	00 15 16.66	+35 03 32.07	59	0.16	**0.20**	5.8	19.5	25.70	**27.90**	–	< **0.24**$^{\mathrm{m}}$	0.88	< 0.25	FD
TOOT00_1267	00 15 31.30	+36 12 20.82	10	**0.59**	0.52	25.5	93.9	**99.50**	99.50	**0.83**	1.45	0.80	0.48	CD
TOOT00_1188	00 15 56.42	+35 39 50.04	17	**0.10**	0.11	4.7	13.6	**14.70**	14.70	–	< **0.15**$^{\mathrm{m}}$	0.86	< 0.57	CD
TOOT00_1196	00 16 35.57	+35 42 26.83	–	**0.10**	0.11	4.4	–	–	< **0.9**	–	–	> 2.11	–	FD?
TOOT00_1173	00 16 59.60	+35 34 47.92	41	**0.16**	0.15	7.4	16.6	23.90	**28.80**	–	**0.28**$^{\mathrm{m}}$	0.77	0.78	TJ
TOOT00_1228	00 17 03.05	+35 56 20.54	<4	**0.28**	0.25	10.5	80.1	**79.10**	79.10	–	< **0.16**$^{\mathrm{m}}$	0.57	< -0.78	COM
TOOT00_1034	00 17 04.49	+34 47 03.22	45	0.59	**0.61**	27.6	122.6	129.6	**140.5**	**0.80**	1.45	0.66	0.38	TJ
TOOT00_1255	00 17 27.53	+36 07 33.39	8	**0.14**	0.13	8.3	32.3	**33.80**	33.80	–	**0.29**$^{\mathrm{m}}$	0.64	1.02	CD?
TOOT00_1048	00 18 16.36	+34 50 40.53	7	**0.84**	0.86	38.4	103.4	**104.1**	104.1	**1.18**	1.18	0.94	0.48	CD
TOOT00_1029	00 18 28.43	+34 45 00.55	<5	**0.11**	0.11	5.0	20.5	**24.10**	24.10	–	< **0.21**$^{\mathrm{m}}$	0.68	< 0.91	COM?
TOOT00_1115	00 18 54.19	+35 10 08.54	8	**0.36**	0.32	14.7	55.5	**56.10**	56.10	–	**0.25**$^{\mathrm{m}}$	0.83	-0.51	TJ?
TOOT00_1132	00 19 20.03	+35 19 42.63	4	**0.47**	0.42	18.5	89.3	**88.30**	88.30	–	**0.62**$^{\mathrm{m}}$	0.75	0.39	TJ?
TOOT00_1250	00 19 55.00	+36 06 25.82	25^{os}	**0.36**	0.41	18.3	48.9	**54.00**	54.00	**0.51**	0.51	0.85	0.49	CD?
TOOT00_1268	00 21 51.92	+36 12 25.39	8	**0.13**	0.11	6.7	58.5	**61.20**	61.20	–	< **0.30**$^{\mathrm{m}}$	0.34	< 1.17	COM
TOOT00_1251	00 22 19.64	+36 06 34.89	25	0.20	**0.21**	11.1	20.2	17.30	**19.60**	–	**0.30**$^{\mathrm{m}}$	1.06	0.50	CD
TOOT00_1203	00 23 32.00	+35 45 00.84	5	0.91	**1.06**	38.9	153.2	**164.6**	164.6	**1.07**	1.07	0.84	0.01	CD?

Table 2. Observing log for the optical spectroscopy: In **Column 1** we give the name of the object. **Column 2** gives the observing date. **Column 3** gives the coordinates where the slit was centred. **Column 4** gives the exposure time (in seconds) in the blue 'B' and the red 'R' part of the WHT ISIS spectrum; 'LRS' denotes spectroscopy taken with the HET. **Columns 5 & 6** give the width and the position angle of the long axis of the slit respectively.

(1)	(2)	(3)	(4)	(5)	(6)
Object	Date	Position (J2000)	Exposures Time (s)	Slit Width (arcsec)	PA (°)
TOOT00_1140	28Aug2000	00 08 30.81 +35 21 47.9	(1x1450B, 1x600R + 1x900R)	1.5	278
TOOT00_1099	28Aug2000	00 09 23.73 +35 05 05.5	(1x1400B, 1x450R + 1x900R)	1.5	111
TOOT00_1125	28Aug2000	00 09 36.62 +35 15 43.4	(1x740B, 1x600R)	1.5	122
TOOT00_1143	31Aug2000	00 09 46.89 +35 23 45.2	(1x1000B, 1x600R + 1x900R)	1.5	80
TOOT00_1233	30Aug2000	00 09 53.26 +35 58 23.1	(1x600B, 1x250R + 1x300R)	1.5	160
TOOT00_1022	31Aug2000	00 10 37.69 +34 41 22.6	(1x1800B, 2x900R)	1.5	9
	19Aug2006	00 10 37.69 +34 41 22.8	(1x1800B, 2x900R)	2.0	140
TOOT00_1204	29Aug2000	00 10 40.53 +35 45 48.6	(1x1000B, 1x600R + 1x900R)	1.5	112
TOOT00_1235	29Aug2000	00 10 45.54 +35 59 51.7	(1x1100B, 1x450R + 1x600R)	1.5	272
TOOT00_1224	29Aug2000	00 10 48.80 +35 55 48.6	(1x1800B, 2x900R)	1.5	269
	20Aug2006	00 10 48.80 +35 55 48.6	(1x1800B, 2x900R)	2.5	28
TOOT00_1291	30Aug2000	00 10 52.97 +35 28 26.9	(1x1800B, 1x600R + 1x1200R)	1.5	125
	18Jul2004	00 10 52.97 +36 28 26.9	(1x1800B + 1x655B, 1x655R + 2x900R)	2.5	54
TOOT00_1107	14Jul2004	00 11 12.90 +35 07 19.9	(1x600B + 1x1200B + 1x1800B, 4x900R)	1.5	95
TOOT00_1180	29Aug2000	00 11 12.92 +35 37 59.8	(1x1800B, 2x900R)	1.5	160
TOOT00_1027	30Aug2000	00 11 17.00 +34 43 33.7	(1x1800B, 2x900R)	1.5	255
	13Jul2004	00 11 17.57 +34 43 33.7	(1x1200B + 2x1800B, 1x450 + 4x900R)	2.0	255
TOOT00_1195	31Aug2000	00 11 52.40 +35 42 19.2	(1x1800B, 1x600R + 1x1200R)	2.0	96
TOOT00_1069	15Jul2004	00 12 12.58 +34 58 30.9	(1x1800B, 1x450R + 1x600R)	4.0	0
TOOT00_1094	29Aug2000	00 12 16.30 +35 04 23.7	(1x1800B, 2x900R)	2.0	235
TOOT00_1149	28Aug2000	00 12 18.01 +35 27 29.1	(1x300B, 1x300R)	2.0	109
TOOT00_1298	28Aug2000	00 12 24.30 +36 33 10.2	(1x1100B, 1x565R + 1x600R)	2.0	90
TOOT00_1200	29Aug2000	00 12 31.21 +35 43 33.2	(1x1800B, 2x900R)	2.0	143
TOOT00_1215	30Aug2000	00 12 45.89 +35 52 20.5	(1x1800B, 2x900R)	1.5	95
TOOT00_1240	31Aug2000	00 13 05.91 +36 01 47.4	(1x500B + 1x142B, 1x300R+ 1x159R + 1x142R)	2.5	100
			(1x650B, 1x300R + 1x350R)	1.5	100
	15Jul2004	00 13 01.44 +36 02 12.0	(1x1100B, 1x450R + 1x600R)	2.0	19
	19Aug2009	00 13 05.33 +36 01 50.7	(1x1800B, 2x900R)	2.5	100
TOOT00_1289	31Aug2000	00 13 12.32 +36 27 16.3	(1x1800B, 2x900R)	2.0	75
TOOT00_1072	31Aug2000	00 13 13.32 +34 59 40.8	(1x1200B, 2x600R)	2.5	35
TOOT00_1134	17Oct2003	00 13 30.63 +35 20 52.7	(2x1200LRS)	2.0	126
TOOT00_1244	30Aug2000	00 13 29.91 +36 03 51.4	(1x1700B, 1x600R + 1x900R)	1.4	85
TOOT00_1066	31Aug2000	00 13 48.27 +34 56 57.7	(1x1800B, 1x600R + 1x1200R)	2.5	127
TOOT00_1261	30Aug2000	00 14 06.53 +36 08 28.1	(1x110B, 1x450R + 1x600R)	2.0	145
TOOT00_1252	28Aug2000	00 14 28.80 +36 06 52.2	(1x1800B, 2x900R)	2.5	109
	17Jul2004	00 14 30.57 +36 06 44.8	(1x1800B, 2x900R)	1.0	265
TOOT00_1214	28Aug2000	00 14 43.70 +35 52 04.2	(1x1800B, 2x900R)	2.0	116
TOOT00_1152	30Aug2000	00 14 49.61 +35 28 09.6	(1x1300B + 1x1800B, 1x300R + 3x900R)	3.0	65
TOOT00_1129	30Aug2000	00 15 04.40 +35 18 56.5	(1x1800B, 2x900R)	3.0	113
TOOT00_1090	31Aug2000	00 15 16.02 +35 03 26.5	(1x300B, 1x300R)	1.5	87
TOOT00_1267	31Aug2000	00 15 30.89 +36 12 14.4	(1x1800B, 2x900R)	2.0	40
TOOT00_1188	31Aug2000	00 15 56.58 +35 39 49.2	(1x1800B, 2x900R)	2.0	136
TOOT00_1196	16Jul2004	00 16 35.73 +35 42 23.0	(1x1800B, 2x900R)	1.5	256
TOOT00_1173	30Aug2000	00 16 59.54 +35 34 36.0	(1x1100B, 1x450R + 1x600R)	1.5	80
TOOT00_1228	30Aug2000	00 17 03.03 +35 56 18.1	(1x1500B, 1x600R + 1x900R)	1.5	103
	18Jul2004	00 17 03.11 +35 56 18.1	(1x1800B, 2x900R)	2.0	243
TOOT00_1034	30Aug2000	00 17 04.27 +34 46 59.1	(1x1800B, 1x600R + 1x1200R)	2.0	123
	16Jul2004	00 17 04.16 +34 46 59.8	(1x1800B, 2x900R)	2.0	111

Table 2. (continued)

(1) Object	(2) Date	(3) Position (J2000)	(4) Exposures Time (s)	(5) Slit Width (arcsec)	(6) PA (°)
TOOT00_1255	30Aug2000	00 17 28.32 +36 07 26.5	(1x1500B, 1x600R + 1x900R)	2.0	156
TOOT00_1048	31Aug2000	00 18 16.28 +34 50 35.5	(1x1800B, 2x900R)	1.5	28
	18Jul2004	00 18 16.37 +34 50 36.6	(1x1800B, 2x900R)	2.5	28
TOOT00_1029	30Aug2000	00 18 28.06 +34 44 49.2	(1x1450B, 1x450R + 1x900R)	2.0	123
TOOT00_1115	28Aug2000	00 18 53.88 +35 10 11.8	(1x1500B, 1x600R + 1x800R)	2.0	90
TOOT00_1132	30Aug2000	00 19 20.11 +35 19 35.8	(1x300B, 1x300R)	1.5	87
TOOT00_1250	30Aug2000	00 19 54.45 +36 06 20.4	(1x399B + 1x591B + 1x859B, 1x300R + 1x600R)	2.0	90
TOOT00_1268	29Aug2000	00 21 52.00 +36 12 18.2	(1x1300B, 2x600R)	1.5	57
TOOT00_1251	29Aug2000	00 22 19.42 +36 06 36.4	(1x1800B, 1x600R + 1x1200R)	2.0	10
TOOT00_1203	29Aug2000	00 23 31.63 +35 45 04.3	(1x1000B, 2x600R)	2.5	90
	30Aug2000	00 23 31.61 +35 45 02.6	(1x1200B, 2x600R)	1.5	0

Table 3. Spectroscopic and photometric redshifts: **Column 1** gives the name of the object and **Columns 2 & 3** give the RA and Dec of the near-IR K-band identification of each radio source respectively. **Column 4** gives the optical classification (OpCl) of the radio source, where 'G' stands for a galaxy and 'Q' for a quasar; 'a' denotes a broad-absorption-line QSO (BALQSO). **Column 5** presents the radio-optical classification (R-OpCl): FRIIs correspond to CD objects; FRIs to FD and TJ; Q-F corresponds to quasars with flat radio spectral index ('F' denotes flat radio spectral index $\alpha_{\rm 151MHz}^{\rm 1.4GHz} \lesssim 0.5$; a '?' denotes α close to 0.5); CSS-Q corresponds to quasars with compact radio structure; FRII-Q denotes a quasar that has FRII radio structure; CSS denotes a compact steep spectrum radio source. **Column 6** gives the spectroscopic redshift as measured from the spectra (Figure A1); a '?' denotes uncertainty or a featureless continuum. **Column 7** gives the photometric redshift calculated from HyperZ using BC templates (see Section 3.1); redshifts corresponding to secondary best-fit templates are marked with '2nd'. Values in brackets are deemed uncertain because there is no clear step change in flux associated with the 4000-Å break in the SED (see Figure A1). **Column 8** gives redshifts estimated from the $K-z$ relation of Willott et al. (2003) as described in Section 3.1. **Column 9** gives the K magnitude of each object in the Vega system, measured with 4-arcsec (or 3-arcsec in case of confusion) diameter aperture from the centre of its infrared position, denoted as '(4)' (or '(3)'); in the absence of such a measurement we use the one measured from the ODT survey (MacDonald et al. 2004), marked with an (O). The symbol 'p' is used in the case where the object is a point source at K; applicable for magnitudes $K < 18$ as a $\sim 10\sigma$ signal-to-noise ratio is necessary to clarify whether or not an object is a point source at K. The symbol '$*$' denotes data from the 'Inskip' near-IR sample (see Section 2).

(1)	(2)	(3)	(4)	(5)	(6)	(7)	(8)	(9)
Name	RA	DEC	OpCl	R-OpCl	$z_{\rm spec}$	$z_{\rm photBC}$	$z_{\rm photK-z}$	K (mag)
TOOT00_1140	00 08 30.8	+35 21 48.1	G	FRI	**0.911?**	1.155	0.821	17.0 (4)
TOOT00_1099	00 09 23.7	+35 05 05.5	G	FRI?	**1.397?**	0.470	0.646	16.5 (4*)
TOOT00_1125	00 09 36.6	+35 15 43.1	Q	FRII-Q	**1.916**	[2.540]	0.424	15.6 (4p)
TOOT00_1143	00 09 46.9	+35 23 44.8	G	FRI	**0.438**	0.370	0.505	16.0 (3)
TOOT00_1233	00 09 53.2	+35 58 23.4	Q$^{\rm a}$	Q-F	**1.244**	[2.255]	0.355	15.3 (4p)
TOOT00_1022	00 10 37.7	+34 41 23.1	G	CSS	?	[2.790]	**2.872**	19.4 (4)
TOOT00_1204	00 10 40.6	+35 45 48.3	G	FRI	**0.6395**	0.600	0.574	16.3 (4)
TOOT00_1235	00 10 45.5	+35 59 51.3	Q	Q-F?	**0.743**	1.720	0.833	17.0 (4*p)
TOOT00_1224	00 10 48.8	+35 55 49.0	G	CSS		[3.050]	**3.438**	19.7 (4*)
TOOT00_1291	00 10 51.4	+36 28 29.7	G	FRII?	?	[1.580]	**0.917**	17.3 (4)
TOOT00_1107	00 11 12.3	+35 07 20.6	G	FRI	**0.300**	2.615 (0.415)$^{\rm 2nd}$	1.426	18.1 (4)
TOOT00_1180	00 11 12.9	+35 38 00.1	G?	FRII?	**1.810**	1.345	1.624	18.3 (4)
TOOT00_1027	00 11 17.0	+34 43 33.8	G	CSS	**0.890**	0.655	3.015	19.5 (4)
TOOT00_1195	00 11 52.4	+35 42 20.0	G	FRII	?	[2.290]	**1.418**	18.1 (4*)
TOOT00_1069	00 12 12.6	+34 58 30.9	Q	CSS-Q	**2.300**	[0.050] (2.036)$^{\rm 2nd}$	4.840	> 20.3 (4)
TOOT00_1094	00 12 16.3	+35 04 23.4	G	CSS	**1.516?**	1.690	1.616	18.3 (4)
TOOT00_1149	00 12 18.0	+35 27 29.2	G	FRI	**0.260**	0.150	0.257	14.6 (O)
TOOT00_1298	00 12 24.2	+36 33 10.5	G	FRI	**1.287?**	[5.000] (1.491)$^{\rm 2nd}$	0.985	17.3 (4)
TOOT00_1200	00 12 31.3	+35 43 33.2	G?	FRII	**0.691**	0.775	1.031	17.4 (4)
TOOT00_1215	00 12 45.9	+35 52 19.1	G	FRI?	**0.278**	1.740	0.306	15.0 (O)
TOOT00_1240	00 13 05.3	+36 01 51.0	G?	FRII	**2.543?**	[4.990]	2.185	18.9 (4)
TOOT00_1289	00 13 12.2	+36 27 16.1	G	FRII	**1.784?**	[1.255]	1.227	17.8 (4)
TOOT00_1072	00 13 13.3	+34 59 40.8	G	FRII	**0.577**	0.715	0.441	15.7 (4)
TOOT00_1134	00 13 21.2	+35 20 07.6	G	FRI	**0.311**	0.365	0.259	14.6 (4)
TOOT00_1244	00 13 30.1	+36 03 51.0	Q	Q-F?	**1.358**	[0.440] (1.590)$^{\rm 2nd}$	2.081	18.8 (Op)
TOOT00_1066	00 13 48.3	+34 56 57.6	G	FRII	**0.926?**	1.395	1.382	18.0 (4*)
TOOT00_1261	00 14 06.6	+36 08 27.1	Q?	FRII-Q?	**2.544**	1.940 (2.696)$^{\rm 2nd}$	2.365	19.0 (4)
TOOT00_1252	00 14 30.2	+36 06 43.4	G	FRII?	?	[1.670]	**3.229**	> 19.6 (4)
TOOT00_1214	00 14 43.6	+35 52 05.3	Q?	FRII-Q?	**3.081**	[2.360]	1.882	18.6 (3)
TOOT00_1152	00 14 49.7	+35 28 11.1	G	FRII	?	[0.275]	**3.310**	19.6 (4)
TOOT00_1129	00 15 04.3	+35 18 56.9	Q?	FRII-Q?	**1.860**	[2.905]	4.508	20.2 (4)
TOOT00_1090	00 15 15.9	+35 03 27.7	G	FRI	**0.201**	0.290	0.253	14.6 (4)
TOOT00_1267	00 15 31.0	+36 12 16.5	G?	FRII	**0.968**	1.160	0.873	17.1 (4*)
TOOT00_1188	00 15 56.3	+35 39 52.1	G?	FRII	**1.417**	0.945	1.650	18.3 (4)
TOOT00_1196	00 16 35.7	+35 42 22.8	G?	FRII?	?	[1.030]	**1.662**	18.4 (4)
TOOT00_1173	00 16 59.5	+35 34 35.9	G	FRI	**0.332**	0.300	0.367	15.3 (4)
TOOT00_1228	00 17 03.0	+35 56 18.4	G	CSS	**1.135?**	0.100	1.658	18.4 (4)
TOOT00_1034	00 17 04.8	+34 46 56.5	G	FRI	**0.580**	0.695	0.523	16.1 (4)
TOOT00_1255	00 17 28.2	+36 07 27.2	G	FRII?	**0.582**	0.730	0.750	16.8 (4*)
TOOT00_1048	00 18 16.5	+34 50 36.2	G?	FRII	**1.943**	[0.945]	1.074	17.5 (4p)
TOOT00_1029	00 18 28.0	+34 44 49.5	G	CSS	**0.737**	0.835	0.472	15.9 (4)
TOOT00_1115	00 18 53.9	+35 10 11.4	G	FRI?	**0.416**	0.450	0.470	15.9 (4)
TOOT00_1132	00 19 20.1	+35 19 36.2	G	FRI?	**0.183**	0.155	0.312	15.0 (4)
TOOT00_1250	00 19 54.4	+36 06 22.2	Q	FRII?	**1.350**	2.310	1.346	18.0 (4p)
TOOT00_1268	00 21 52.0	+36 12 18.4	Q?	Q-F	**2.015**	[0.880]	1.142	17.6 (4p)
TOOT00_1251	00 22 19.0	+36 06 29.6	G?	FRII	**2.490**	[1.050]	2.408	19.1 (4)
TOOT00_1203	00 23 31.6	+35 45 04.2	G	FRII?	**1.397**	1.195	1.010	17.4 (4*)

Table 4. Emission line properties: **Column 1** gives the name of the object. **Columns 2 & 3** give the measured (observed) values of the equivalent width (EW in Å) and the FWHM (in km/s) of the most prominent emission line in the optical spectrum. **Column 4** gives the flux of the [OII]$_{3727}$ emission line, S_{line} in units of 10^{-19} Wm^{-2}, as measured from the spectrum of each object; in the case where the [OII] line is not present we use the brightest available line as shown; 'n' denotes measurement of a narrow line profile at FWHM using a Gaussian fit; a '—' is used when no spectroscopy is available. **Column 5** gives the emission line used in the calculations. **Column 6** gives the base-10 logarithm of the rest-frame luminosity at 151 MHz, which is used in Figures 4, 5 & 6.

(1)	(2)	(3)	(4)	(5)	(6)
Name	EW (Å)	FWHM (km/s)	$S_{\rm line}$ (10^{-19} W m^{-2})	Emission Line	log$_{10}$($L_{151\rm MHz}$/ [WHz^{-1}sr^{-1}])
TOOT00_1140			< 0.20	[OII]	26.21
TOOT00_1099	98	416	9.10	[OII]	26.21
TOOT00_1125	169	5253	70.0	Ly$\alpha^{\rm n}$	27.17
TOOT00_1143			< 0.52	[OII]	24.87
TOOT00_1233	17	1374	4.20	CIII]	25.66
TOOT00_1022			< 3.65	Lyα	26.77
TOOT00_1204	21	388	1.20	[OII]	25.14
TOOT00_1235	30	524	21.4	[OII]	25.72
TOOT00_1224			—		27.07
TOOT00_1291			< 0.91	[OII]	25.78
TOOT00_1107	15	198	0.31	[OII]	24.65
TOOT00_1180	98	434	2.30	Ly$\alpha^{\rm n}$	26.44
TOOT00_1027	22	954	0.22	[OII]	25.13
TOOT00_1195			< 0.20	[OII]	26.05
TOOT00_1069	1296	10870	1.30	Ly$\alpha^{\rm n}$	26.76
TOOT00_1094	290	1402	0.65	MgII	27.43
TOOT00_1149			< 2.05	[OII]	24.70
TOOT00_1298	27	574	1.11	[OII]	26.00
TOOT00_1200	198	738	5.70	[OII]	26.38
TOOT00_1215	23	743	2.70	[OII]	24.84
TOOT00_1240	145	1239	5.64	Lyα	26.89
TOOT00_1289	74	160	1.43	MgII	26.54
TOOT00_1072			< 0.68	[OII]	25.75
TOOT00_1134			< 1.79	[OII]	25.52
TOOT00_1244	336	4526	10.0	CIV$^{\rm n}$	25.92
TOOT00_1066	142	1342	1.14	[OII]	25.50
TOOT00_1261	606	4755	3.60	Ly$\alpha^{\rm n}$	26.78
TOOT00_1252					27.06
TOOT00_1214	444	2055	1.40	Ly$\alpha^{\rm n}$	26.80
TOOT00_1152			< 0.83	Lyα	27.24
TOOT00_1129	277	1185	31.2	Ly$\alpha^{\rm n}$	27.21
TOOT00_1090	12	2453	7.00	[OII]	24.26
TOOT00_1267	1324	104	0.94	[OII]	26.30
TOOT00_1188	113	1102	1.80	[OII]	25.94
TOOT00_1196			< 0.21	MgII	26.64
TOOT00_1173	17	2127	5.00	[OII]	24.64
TOOT00_1228	42	381	1.35	[OII]	26.06
TOOT00_1034	5	1004	0.37	[OII]	25.76
TOOT00_1255	28	361	0.52	[OII]	25.12
TOOT00_1048	454	1744	0.68	Ly$\alpha^{\rm n}$	27.23
TOOT00_1029	25	658	0.60	[OII]	25.26
TOOT00_1115	111	813	3.37	[OII]	25.22
TOOT00_1132	47	680	10.9	[OII]	24.53
TOOT00_1250	141	3865	0.75	CIII]$^{\rm n}$	26.44
TOOT00_1268	401	1285	6.30	Ly$\alpha^{\rm n}$	26.17
TOOT00_1251	225	933	0.14	Ly$\alpha^{\rm n}$	26.95
TOOT00_1203	134	649	35.8	[OII]	26.94

3 ANALYSIS

3.1 Optical classification and redshifts

The optical spectroscopy of the 47 TOOT00 radio sources provided 40 out of 47 redshifts. For the other 7 objects there was either a lack of emission lines, or the spectrum was totally blank. Thus the TOOT00 radio-source sample is 85% spectroscopically complete. Using the results of the spectroscopy, and in combination with individual characteristics for each of them, we classify the 47 TOOT00 radio sources according to the following optical criteria:
i) **Q**: Objects with definite broad lines in their optical spectrum (6/47); all of them have blue SEDs and all apart from one (TOOT00_1069) are point sources at K.
ii) **Q?**: Objects without definite broad lines in the optical spectrum, but that are either point sources at K, or there is a clear hint of broad lines in the optical spectrum, or both (4/47); all objects have a blue SED.
iii) **G?**: Evidence from the optical spectrum that at least one high-excitation (see e.g. Jackson & Rawlings 1997) narrow emission line exists (8/47).
iv) **G**: All the objects that don't fall in the previous categories (29/47); all cases are resolved at K.

One of the TOOT00 'Q' objects, TOOT00_1233, is possibly a broad-absorption-line QSO (BALQSO; see notes on objects in Appendix A), as shown in Figure A1.

We calculate photometric redshifts $z_{\rm photBC}$ with the HyperZ photometric code (Bolzonella et al. 2000) using photometry from $U-$band ($>$ 3600 Å) to the $K-$band (2.2 μm) and Bruzual-Charlot (Bruzual & Charlot 2003; BC) templates. In nearly all cases we let reddening (Calzetti et al. 2000) be a free parameter (see notes on objects in Appendix A for a few exceptions), but the derived values of $A_{\rm V}$ were typically small. Results are shown in Table 3. In many cases we put the value obtained in square brackets, as the probability density function for the redshift is not sharply peaked, typically because the SED is not galaxy-like or is too sparsely sampled above the putative 4000 Å break.

In Figure 2a we present a comparison of spectroscopic and photometric redshifts. The Q and Q? type objects fall off the correlation line, which is unsurprising because all but two of them have a highly uncertain photometric redshift due, presumably, to significant contributions to their SEDs from non-stellar light causing the galaxy HyperZ templates to be inappropriate; the exception is TOOT00_1244 for which the spectroscopic and photometric $z_{\rm photBC}$ have similar values. The 'G' type objects with high $z_{\rm spec}/z_{\rm photBC}$ typically fall off the correlation, because they have a highly uncertain $z_{\rm photBC}$; the exceptions being TOOT00_1099 and TOOT00_1228, although the latter has an uncertain spectroscopic redshift. In TOOT00_1215 the disagreement between spectroscopic and photometric HyperZ redshift probably reflects the fact that more photometric points are needed for an accurate fit of the BC template. In Figure 2b we see that quasars tend to have lower photometric redshifts than their spectroscopic ones, with the exception of TOOT00_1069, presumably because their K-band light is contaminated by non-stellar emission. Objects TOOT00_1027, TOOT00_1107, TOOT00_1129, TOOT00_1069 are all seemingly intrinsically faint objects in the near-IR K-band, which yields the high $z_{\rm photK-z}$ value (see Willott et al. 2003).

Due to a ∼85% (40 out of 47 objects) spectroscopic completeness we only need to use photometric redshifts for 7 out of the 47 objects. For these 7 objects we use a photometric redshift calculated from the $K-z$ relation of Willott et al. (2003; hereafter $K_{\rm W}-z$ relation). The $K_{\rm W}-z$ fits the 3CRR, 6CE and 7CRS data sets, where the K magnitude is aperture and emission line corrected:

$$K_W = 17.37 + 4.53 \times (\log_{10} z) - 0.31 \times (\log_{10} z)^2, (1)$$

where K is the $K-$band magnitude and z the redshift.

When using the $K_{\rm W}-z$ relation we kept in mind that the K magnitude of our sample is not emission-line or aperture corrected. This means that the $K_{\rm W}-z$ relation may give a slightly incorrect estimate for the photometric redshift of our objects. We believe, though, that these errors are negligible for our sample. According to Willott et al. (1999), one expects the line flux to scale with radio flux density at K-band, so the line contamination of the K-band magnitude should be small in TOOT. Additionally, we chose not to perform aperture or emission line corrections in our K magnitude for the following reasons: (i) above redshift $z > 0.6$ aperture corrections are $\sim$ 0.05 mag (Eales et al. 1997); (ii) most of the objects have K-band magnitude measured in the same aperture, apart from some exceptions due to confusion by a nearby object (see Table 1 and Appendix A) and any corrections would be highly dependent on the assumed light spatial profile which is uncertain. In our analysis, whenever we use the redshift calculated from the $K_{\rm W}-z$, it is only for objects at high redshift $z > 0.9$, where line and aperture corrections, although uncertain, are probably small.

3.2 Radio classification, spectral indices and sizes

Figure A1 (see Appendix A) presents near-IR/radio overlays for all the TOOT00 objects, where either the A- or B-array VLA maps were used. Another classification we use is based on their radio structure, as shown in Table 1. In the same figure we also present optical spectra and SEDs that were constructed from the photometric data (Table A1 in Appendix A), where the best fit BC templates are shown. In the

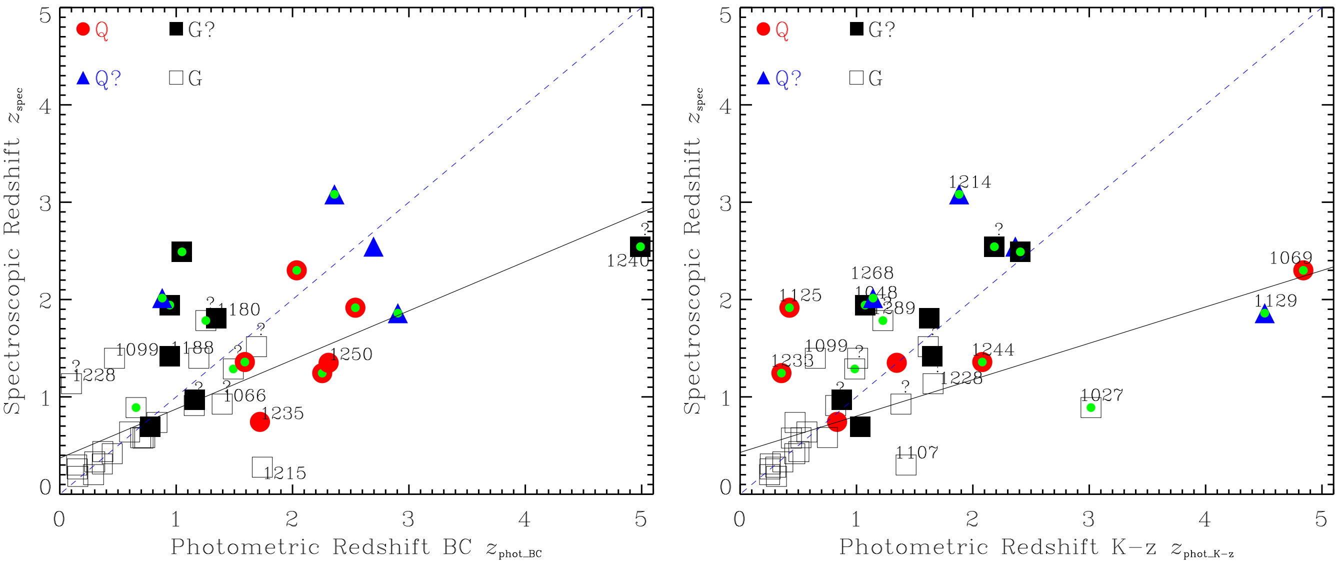

Figure 2. a) Left: Spectroscopic versus photometric redshift calculated from HyperZ. Symbols indicate optical classification as explained in Section 3.1: filled circles for quasars 'Q', blue filled triangles for possible quasars 'Q?', black filled squares for possible galaxies 'G?', and black squares for secure galaxies 'G'. The black solid line is the best fit line for G objects in the $z_{\rm spec}$ vs $z_{\rm photBC}$ correlation, and was calculated using the LINFIT function in IDL, where the objects without spectroscopic redshifts were not included in the calculation: $z_{\rm spec} = 0.50 \times z_{\rm photBC} + 0.37$; the linear Pearson correlation is 0.548 and the Spearman correlation is 0.568 with a 99.53% probability for a correlation. Objects with uncertain photometric redshift are marked with a filled green circle; the character '?' denotes objects with an uncertain spectroscopic redshift. Sources that fall off the dashed blue $z_{\rm spec} = z_{\rm phot}$ line, and do not have an uncertain photometric redshift, are marked with their name. The 7 objects without spectroscopic redshift have been omitted. **b) Right**: Spectroscopic versus photometric redshift calculated using the $K_{\rm W} - z$ relation. Symbols are the same as in figure **a** on the left. The black solid line is the best fit line for G objects in the $z_{\rm spec}$ vs $z_{\rm photK-z}$ correlation, and was calculated as stated above: $z_{\rm spec} = 0.37 \times z_{\rm photK-z} + 0.43$, where the linear Pearson correlation is 0.514 and the Spearman correlation is 0.762 with a 99.99% probability for a correlation. The character '?' denotes objects with an uncertain spectroscopic redshift; objects with uncertain photometric redshift from the HyperZ code are marked with a filled green circle. Sources with $|z_{\rm spec} - z_{\rm phot}| > 0.5$ are marked with their name. Again, the 7 objects without spectroscopic redshift have been omitted. The generalised Spearman correlation coefficient is calculated using survival analysis statistics ASURV (Lavalley et al. 1992).

cases where optical photometry was unavailable from the ODT, the optical magnitude was estimated directly from the spectrum; a mean value of the continuum was used to estimate the flux density in each optical band where the fluxes measured were approximately corrected for systematic errors due to light losses from the slit. This value is approximately 25% for a 1.5-arcsec wide slit; we chose to use a value calculated for each object of ∼ 10% to 40% dependent on the slit width (see Table 2). The errors on the magnitudes (see Table A1 in Appendix A) are taken to be equal to the percentage errors estimated for light losses from the slit.

In Figure 3 we present the $S_{\rm 74MHz}$ versus $S_{\rm 151MHz}$ diagram. The VLSS catalogue provides flux densities for 12 (out of 47) TOOT00 radio sources. Direct measurements from the 74-MHz maps were made for a further 11 TOOT00 objects that were not included in the VLSS catalogue, but appeared to be detected in the 74 MHz maps; the measurements were performed using the IMSTAT package in AIPS. For the other 24 TOOT00 objects, a 2σ detection was adopted as an upper limit (see Table 1). The median spectral index calculated between 74 and 151 MHz including the limits is $\alpha^{\rm 151MHz}_{\rm 74MHz} \sim 0.5$. This confirms, as expected, that the average low-frequency radio spectra approach the $\alpha \sim 0.5$ value expected in emission from un-aged electron populations at the low rest-frame frequency of ∼ 200 MHz (using the median redshift $z \sim 1.25$ of the sample; see Section 4). The fact that we have almost the same amount of limits above and below $\alpha = 0.5$ is re-assuring. The overplotted lines in Figure 3 indicate that the TOOT00 radio sources not detected at 74 MHz are mainly faint enough sources at 151 MHz that with any reasonable radio spectral index they would fall close to the limit of the VLSS survey. In Figure 3, we label three cases (TOOT00_1022, TOOT00_1244 & TOOT00_1298) which, in Table 1,

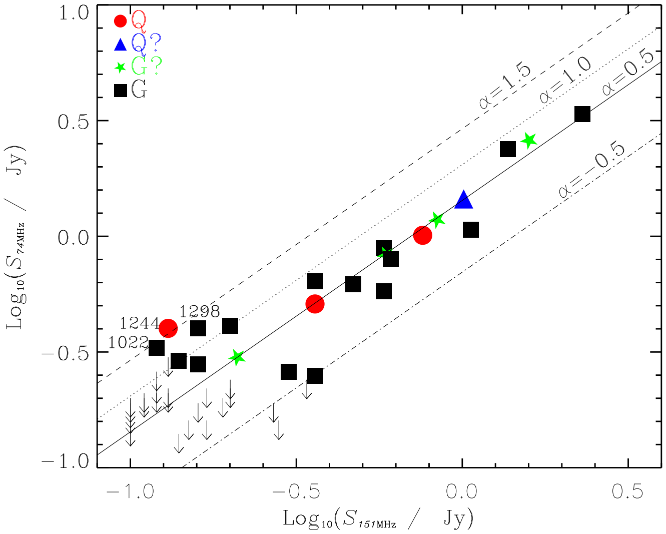

Figure 3. Flux density at 74 MHz $S_{74\mathrm{MHz}}$ versus flux density at 151 MHz $S_{151\mathrm{MHz}}$. Symbols: red circles denote quasars ‘Q’, blue triangles denote possible quasars ‘Q?’, green stars stand for possible galaxies ‘G?’, and black squares for secure galaxies ‘G’. 12 objects were detected by the VLSS and plotted with their symbol. Another 11 have flux densities at 74 MHz measured directly from the VLSS map (see Table 1). Thus, 23 out of 47 TOOT00 objects are detected both at 74 and 151 MHz. The other 24 objects, that have no measurement at 74 MHz, are indicated as 2σ upper limits and plotted with black arrows. The solid black line is for $\alpha = 0.5$, the dotted black line for $\alpha = 1.0$, the dashed black line for $\alpha = 1.5$ and the dotted-dashed line for $\alpha =$ -0.5.

have $\alpha^{151\mathrm{MHz}}_{74\mathrm{MHz}} > 1.2$. In all of these cases the signal-to-noise ratio is ≤ 7 at 151 MHz and ≤ 4 at 74 MHz meaning much lower true values of $\alpha^{151\mathrm{MHz}}_{74\mathrm{MHz}}$ are within the errors.

In Figure 4 we present the radio luminosity at 151 MHz versus the radio spectral index of our objects, calculated using the 1.4-GHz and 151-MHz flux densities presented in Table 1. The median spectral index is $\alpha^{1.4\mathrm{GHz}}_{151\mathrm{MHz}} = 0.86$. In Vardoulaki et al. (2008) we have shown that for a 1.4-GHz selected study of radio sources (SXDS) roughly 10 times fainter at 151 MHz than TOOT00 (see Figure 5), the fraction of flat-spectrum objects is higher. Some important differences between the TOOT00 and SXDS radio-source samples can be attributed to the lower radio-frequency selection of TOOT00 radio sources. One such difference is that there seem to be quite a few objects in the SXDS[¶¶] with flat radio spectral index (i.e. $\alpha < 0.5$). The fraction of SXDS objects with $\alpha <$ 0.5 is 35 ± 6% (13 out of 37), while ∼ 11 ± 3% (4 out of 37) have an inverted radio spectral index (i.e. $\alpha <$ 0). In the TOOT00 sample, only 3 radio sources (∼ 6 ± 3%) have a flat radio spectral index, and only one (2 ± 1%) of them (TOOT00_1027), a possible gigahertz-peaked spectrum (GPS) object, has an inverted radio spectral index (see Table 1). The other two flat-spectrum objects, TOOT00_1233 and TOOT00_1268, are Q and Q? objects respectively. TOOT00_1235 & TOOT00_1244 have radio spectral indices α close to 0.5 and are probably core-jet objects (e.g. Augusto et al. 1998). These radio sources are usually moderately-flat-spectrum sources ($\alpha \sim 0.5$ corresponds to freshly injected electrons) often with double-sided kpc-scale jet-like structures. Both these objects with $\alpha \sim 0.5$ have linear projected sizes $D \sim 100$ kpc, as can be seen in Figure 6a. The observed core-jet radio structure is probably caused by interactions with the intergalactic medium and projection effects (Paragi et al. 2000). The outlier, TOOT00_1196, is either an unusual source or a spurious 7C detection (see Appendix A).

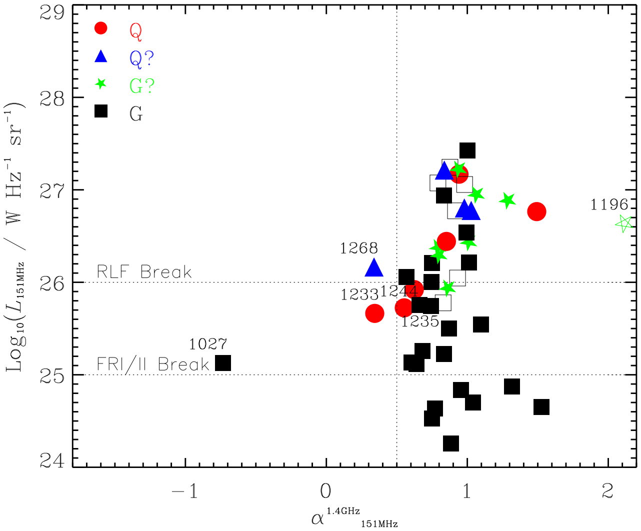

Figure 4. Radio Luminosity at 151 MHz $L_{151\mathrm{MHz}}$ versus the radio spectral index α. Symbols are the same as in Figure 3; filled symbols denote objects with spectroscopic redshifts and open symbols represent objects with photometric redshifts. The horizontal lines show the RLF and FRI/FRII breaks calculated from the Willott et al. (2003) and the Fanaroff & Riley (1974) values respectively using a typical steep-spectrum radio spectral index of 0.8. The vertical line at $\alpha = 0.5$ shows the conventional border between steep and flat-spectrum sources.

Figure 5 presents the radio luminosity at 151 MHz versus redshift for the TOOT00. The flux density limits of various radio surveys are shown: 3C, 6CE, 7CRS (12.4 Jy, 2.0 Jy and 0.5 Jy respectively; Willott et al. 2001), TOOT00 (0.1 Jy), and SXDS (≃ 0.01 Jy at 151 MHz[‖‖]; Vardoulaki et al. 2008).

[¶¶] The radio spectral indices for the SXDS sources were calculated using 1.4 GHz and 610 MHz (or 325 MHz) data, whereas for the TOOT00 we use 1.4 GHz and 151 MHz flux densities; note that is close enough for a rough comparison of the samples.

[‖‖] A typical steep spectrum radio spectral index $\alpha = 0.8$

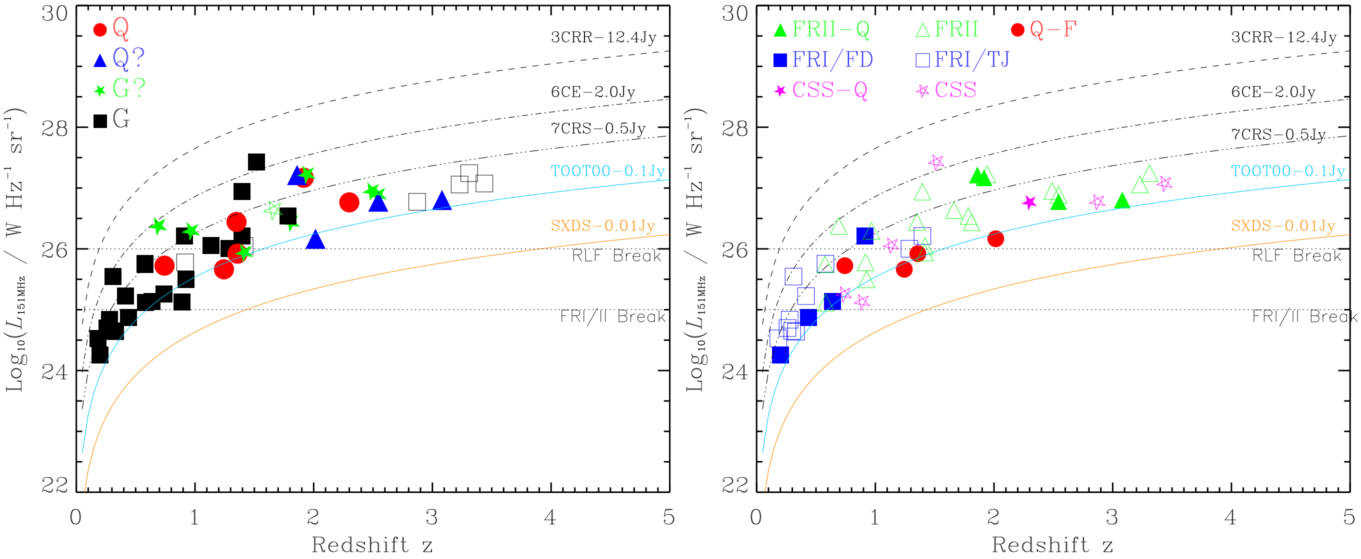

Figure 5. Radio Luminosity at 151 MHz $L_{151\mathrm{MHz}}$ versus redshift z for the TOOT00 sample. **a) Left**: Symbols are the same as in Figure 3; filled symbols represent objects with spectroscopic redshift and open symbols denote objects with photometric redshift. **b) Right**: Symbols denote radio-optical classification: green filled triangles denote FRII-Q objects; green open triangles denote FRIIs; blue filled boxes denote FD type FRIs; blue open boxes denote TJ type FRIs; red filled circles denote Q-F objects; purple filled stars denote CSS-Q objects; purple open stars denote CSS objects; a '?' denotes uncertainty in the radio-optical classification as stated in Table 3. In both plots, the horizontal lines show the RLF and FRI/FRII breaks calculated from the Willott et al. (2003) and the Fanaroff & Riley (1974) values respectively using a typical steep-spectrum index of 0.8. The flux density limits of 3C, 6CE, 7CRS (Willott et al. 2001), TOOT00 and SXDS (Vardoulaki et al. 2008) samples are shown (α = 0.8 was used to convert to 151 MHz flux density).

We note that 3 out of 4 objects above redshift $z = 3$ are galaxies with photometric redshifts derived from the $K_{\mathrm{W}} - z$ relation (see Section 4). The 3 galaxies with photometric redshift $z > 3$ are, TOOT00_1224, TOTO00_1252 & TOOT00_1152 and are very faint at K. According to Willott et al. (2003), the objects in the 7CRS are ≈ 0.3 mag fainter than the ones in the 3CRS and 6CE. Since the $K_{\mathrm{W}}-z$ relation fits all three datasets, it will over-predict the redshift of radio-faint objects. Thus, if we re-calculate the redshift using that correction of 0.3 mag for TOOT00_1224, TOOT00_1252 & TOOT00_1152, then we get redshifts $z = 2.900$, $z = 3.810$ and $z = 2.747$ respectively; only TOOT00_1152 still has a photometric redshift $z_{\mathrm{photK-z}} > 3$.

The angular size θ of the TOOT00 objects is presented in Table 1. This value was measured from the radio maps, A- or B-array, depending on the object (see notes on the objects in Appendix A). In cases where the radio structure was compact in the B-array map but there was evidence of extended structure in the A-array data, the latter was used to measure θ. In cases where the radio source had an one-sided structure, θ was measured from the core to the centre of that lobe. Lastly, in the case where the source presented a complex radio structure (e.g. TOOT00_1107; see Figure A1 in Appendix A), the distance from the core to each lobe was measured and then added together. The angular size θ was used in the calculation of the linear projected size D, which is plotted against the radio luminosity at 151 MHz in Figures 6a & 6b.

3.3 The FRI/FRII structural divide

The structure of radio sources at low redshifts is directly connected to their radio luminosity, where objects with $\log_{10}(L_{151\mathrm{MHz}}/\mathrm{WHz}^{-1}\mathrm{sr}^{1}) \lesssim 25$ are FRI type radio sources and those above that value are FRIIs (Fanaroff & Riley 1974). Another classification used in Table 1 is based on the Owen & Laing (1989) radio classification according to radio structure (see Section 1); in that way we classify the TOOT00 radio sources as CDs, FDs, TJs and COM. Finally, we classify the TOOT00 objects based on both radio and optical data, as presented in Table 3: FRIIs correspond to CD objects; FRIs to FD and TJ; Q-F corresponds to quasars with flat radio spectral index ($\alpha \lesssim$

---

was used to convert from the 2 mJy flux density limit at 1.4 GHz to 151 MHz.

0.5; a '?' denotes α close to 0.5); CSS-Q corresponds to quasars with compact radio structure; FRII-Q denotes a quasar that has FRII radio structure; CSS denotes a compact steep spectrum radio source.

In Figure 6a we present the radio luminosity at 151 MHz $L_{151\mathrm{MHz}}$ versus largest projected linear size D, where we make use of the radio-optical classification (FRI, FRII, Q-F, CSS; see also Figure 5b). Our aim is to investigate whether there is a significant number of FRI objects above the FRI/II and RLF break in radio luminosity. TOOT00 objects with radio luminosities at the FRI/II break are at redshift $z \sim 0.5$, while the ones with $L_{151\mathrm{MHz}} = L_{\mathrm{RLFbreak}}$ are at redshift $z \sim 1.5$ as can be seen in Figure 5. FRII type radio sources occupy the area above the FRI/II break, as is expected. It is interesting, however, that we find 7 FRI type (5 TJs and 2 FDs) radio sources above the FRI/II break with 3 out of 7 of the FRIs also above the RLF break. Although there is an uncertainty in the TJ radio structure of several cases, e.g. TOOT00_1099 and TOOT00_1115 (see Table 1 and Figure A1), we seem able to conclude robustly that there is some cosmic evolution between $z \sim 0$ and $z \sim 1$ in the FRI/II divide as has been commented on previously by Heywood, Blundell & Rawlings (2007).

3.4 The quasar fraction

Figure 6b shows the radio luminosity at 151 MHz versus the largest projected linear size D. The quasar fraction to the total number of objects, is $f_{\mathrm{q}} = 0.25$ (10 out of 40 objects) above the FRI/FRII break (we include Q and Q? type objects as quasars in this calculation; $f_{\mathrm{q}} = 0.13$ if we include only Q objects). Above the RLF break the quasar fraction is 0.27 (7 out of 26 objects); the quasar fraction drops to 0.12 if we exclude the Q? objects. Such values agree with previous studies (e.g. Willott et al. 2000) where the quasar fraction is $\sim 0.1 \rightarrow 0.4$ over the relevant range of radio luminosity $10^{25}\mathrm{WHz^{-1}sr^{-1}} \lesssim L_{151\mathrm{MHz}} \lesssim 10^{27}\mathrm{WHz^{-1}sr^{-1}}$.

Below the FRI/FRII break, the quasar fraction is $f_{\mathrm{q}} = 0$, which also agrees with previous studies. These values increase if one studies objects using 24 μm emission as an indicator of quasar activity, as has been done by Vardoulaki et al. (2008) on the SXDS radio-source sample. This is because hot dust emission at 24 μm is much harder to hide than optical broad lines which can be extinguished by small amounts of dust. The 'quasar-mode fraction' f_{QM}, i.e. the fraction of objects with 'significant' accretion rates, as determined from the observed 24 μm flux density, to the total number of objects, was found to be $\sim 0.5 \rightarrow 0.9$ above the FRI/FRII break and $f_{\mathrm{QM}} \lesssim 0.1$; some high-accretion-rate objects do exist at low radio luminosities. There are no 24 μm data available in the TOOT00 region on which to make a study of f_{QM} in the TOOT00 sample.

4 THE REDSHIFT DISTRIBUTION OF TOOT00

Figure 7a presents the redshift distribution of the 47 TOOT00 radio sources, with a binning of d$z = 0.05$. The median spectroscopic redshift is $z_{\mathrm{spec}} = 1.135$, whereas the median redshift including the photometric redshifts is $z_{\mathrm{med}} = 1.287$. This value is larger than the median redshift of the 6CE and 7CRS radio source surveys (Rawlings, Eales & Lacy 2001; Willott et al. 2003) of $z \sim 1.1$, but we have to take into account that the high-redshift objects of our sample tend to have uncertain photometric redshifts (see Section 3.1). If the $K_{\mathrm{W}} - z$ photometric redshifts are re-calculated for an increase of $\Delta\mathrm{m} = 0.3$ mag in all magnitudes (i.e. assuming a similar offset from the mean $K_{\mathrm{W}} - z$ relation for TOOT00 objects and 7CRS objects), then the median redshift drops to $z_{\mathrm{med}} = 1.244$; we adopt $z_{\mathrm{med}} \sim 1.25$. We note that only TOOT00_1252 could plausibly be at $z \gtrsim 3.5$.

A comparison of the TOOT00 radio-source distribution to any other distribution involves correcting for the 9 objects that were excluded from the original sample and for objects that are missing since the 7C data have significant incompleteness approaching the $S_{151\mathrm{MHz}} = 100$ mJy flux density limit (see Figure 8 of McGilchrist et al. 1990). The weighting factors needed to correct the sensitivity variations across the TOOT00 7C data area not available, so we can only approximately compare our source counts to those in 7C.

We compare the distribution of the TOOT00 radio sources to a simulation obtained from the SKADS Simulated Skies Semi-Empirical Extragalactic Database S^3-SEX (Wilman et al. 2008). This is a set of simulations of the radio sky suitable for planning science with the proposed Square Kilometre Array (SKA) radio telescope (Wilman et al. 2008), that are constructed to match results from the 3CRR, 6CE and 7CRS redshift surveys, as well as radio source counts. This simulation of the extragalactic radio continuum sky allows for large-scale structure in the cosmological distribution of radio sources, and the types included in the simulations are radio-quiet AGN, radio-loud AGN of 'FRI' and 'FRII' classes and star-forming galaxies. Core-jet radio sources are not explicitly included in the simulation. Furthermore, these 'FR classes' are determined directly by the radio luminosity[∗∗∗] and not the radio structure of the objects (see Wilman et al. 2008). Due to these imperfections, and the fact that our radio-optical classification of the TOOT00 radio sources is structural (see Section 3.2), we will name the 'FRI class' in S^3-SEX

[∗∗∗] In S^3-SEX (Wilman et al. 2008), the integration limits for the radio luminosity function of the FRI radio sources are $20.0 \lesssim \log_{10}(L_{151\mathrm{MHz}/\mathrm{WHz^{-1}sr^{-1}}}) \lesssim 28.0$ and those of the FRII radio sources are $25.5 \lesssim \log_{10}(L_{151\mathrm{MHz}/\mathrm{WHz^{-1}sr^{-1}}}) \lesssim 30.5$.

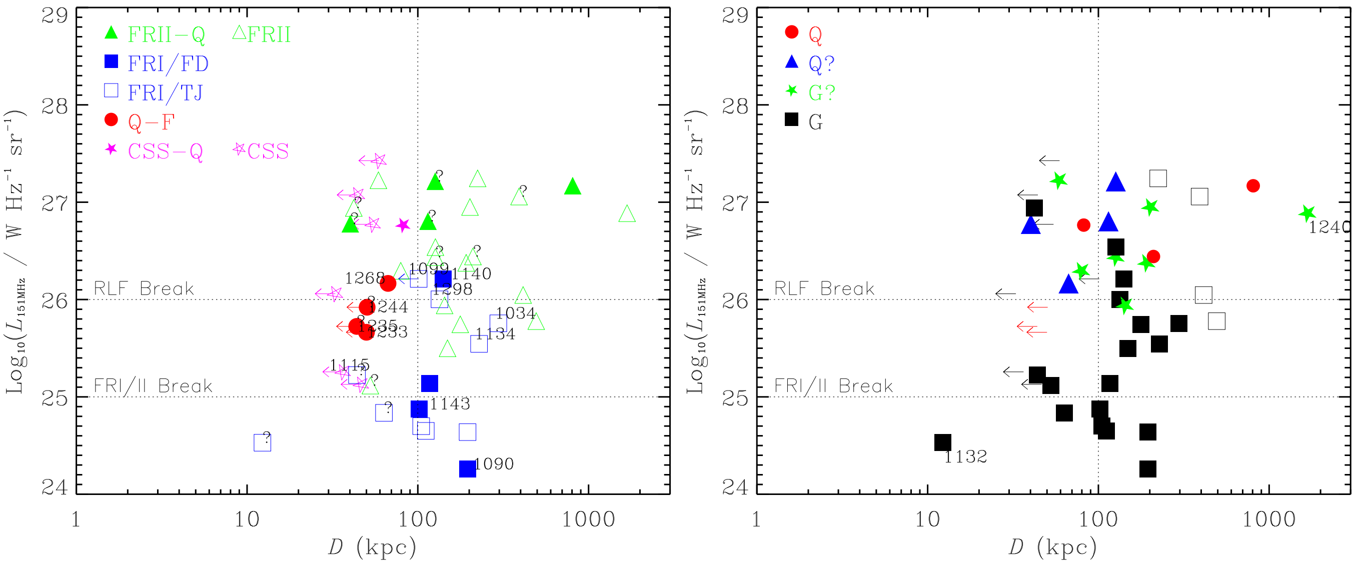

Figure 6. Radio Luminosity at 151 MHz $L_{151\mathrm{MHz}}$ versus the largest projected linear size D. **a) Left:** Symbols denote radio-optical classification as in Figure 5; a '?' denotes uncertainty in the radio-optical classification as stated in Table 3. The horizontal lines show the RLF and FRI/FRII breaks calculated from the Willott et al. (2003) and the Fanaroff & Riley (1974) values respectively using a typical steep-spectrum radio spectral index of 0.8. Objects marked with their name are discussed in the text. **b) Right:** Symbols denote optical classification and are the same as in Figure 3; filled symbols represent objects with spectroscopic redshifts and open symbols denote objects with photometric redshifts. The horizontal lines show the RLF and FRI/FRII breaks calculated from the Willott et al. (2003) and the Fanaroff & Riley (1974) values respectively using a typical steep-spectrum radio spectral index of 0.8. Note that TOOT00_1196 is not plotted since we cannot measure an angular size from the radio maps (see notes on the object in Appendix A).

as the low-L_{151} sub-population and the 'FRII class' as the high-L_{151} sub-population of radio sources. The simulation covers a sky area of 20×20 deg^2 or 0.1212 sr, out to a cosmological redshift of $z = 20$, and down to flux density limit of 10 nJy at 151 MHz, 610 MHz, 1.4 GHz, 4.86 GHz and 18 GHz.

We searched for objects in the S^3-SEX database with simulated 151 MHz total flux density greater than 100 mJy. We found 3139 radio sources above the flux density limit after rejecting those whose core components lay outside the 20×20 deg^2 area of the simulation. The total flux densities of multiple component radio sources (i.e. FRIs and FRIIs) were determined by summing together all of the individual components of each source, including the few components which were outside the 20×20 deg^2 area. Using this full list of radio sources we then constructed 100 circular sub-fields with the same area as TOOT00, namely 0.0015 sr (radius 1.27 deg.) centred at random positions within the simulation. The mean number of objects y from these 100-simulations is $<y> = 40.1$ with a standard deviation, dominated by Poisson errors and the effects of large-scale structure, $\sigma_y = 8.82$.

The flux density scale of TOOT00 was bootstrapped from 6C, so should be accurate at the ± 10% level. This is supported by Figure 3, which shows that the sources detected at both 74 MHz and 151 MHz have spectral indices ∼ 0.5, as expected at low frequencies where the spectral index should reflect the injected, i.e. un-aged, power-law index of the underlying distribution in electron energies (e.g. Alexander & Leahy 1987).

There has been no quantitative estimate of the incompletenesses and Eddington bias (e.g. Teerikorpi 2004) in the lower flux density bins of the TOOT00 7C data, which are extremely important effects given the low signal-to-noise thresholds adopted in the catalogue (see Table 1). The raw TOOT00 7C source counts are significantly higher than those inferred in the 7C survey of McGilchrist et al. (1990), largely because of lower significance sources. At the $S_{151\mathrm{MHz}} \simeq$ 100 mJy level, corrections for incompleteness and Eddington bias are highly uncertain. Most of the TOOT00 radio sources, apart from 9 (see Table 1) and the 9 'off-edge' objects, have a signal-to-noise ratio ∼ 5.5, a criterion similar to that adopted by McGilchrist et al. (1990); note that there is only one possible spurious source in our final list (TOOT00_1196; see Appendix A) as we have securely detected all bar this one source with the VLA. We find 56 sources in 5.0 deg^2 in the TOOT00 region. The source counts in the

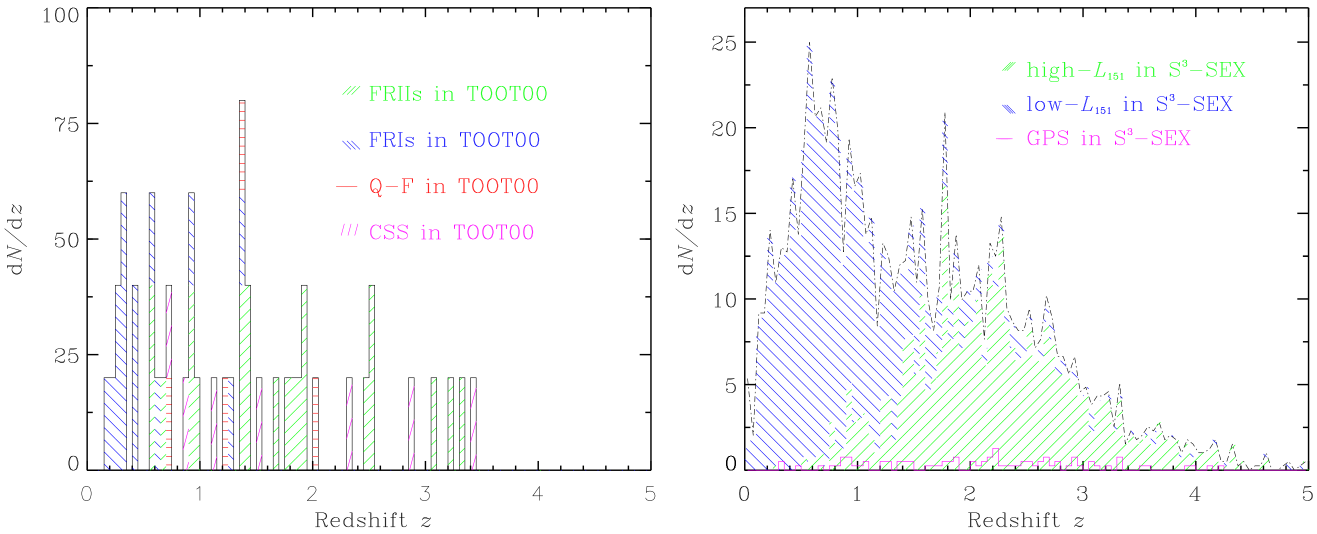

Figure 7. a) Left: Histogram of the redshift distribution for the 47 TOOT00 radio sources according to radio/optical class (see Table 3). The binning on the redshift axis is d$z = 0.05$. The green colour represents FRIIs, blue represents FRIs, red represents flat-spectrum quasars (Q-F) and purple represents CSS objects; the black histogram shows the TOOT00 distribution. FRIIs correspond to CD radio sources, FRIs to FD and TJ, Q-F to quasars with flat radio spectral index, Q-F? to quasars with α close to the critical value 0.5 ($0.5 < \alpha^{1.4\mathrm{GHz}}_{151\mathrm{MHz}} < 0.7$), Compact Steep Spectrum (CSS) to objects with steep radio spectral index ($\alpha > 0.7$) and compact radio structure, and CSS-Q to quasars associated with a compact steep spectrum ($\alpha > 0.7$) object. **b) Right:** Model predictions from the S^3-SEX simulation (Wilman et al. 2008) for an area of 0.1212 sr, which is scaled down to the TOOT00 area of 0.0015 sr. The binning on the redshift axis is d$z = 0.05$. Objects are marked according to their radio source classification as stated in Wilman et al. (2008); blue denotes high-L_{151} objects, green denotes low-L_{151} objects and purple stands for GPS sources in the S^3-SEX simulation; RQQ and normal galaxies are not presented for clarity.

TOOT00 7C region using only $> 5.5\ \sigma$ detections are 24.7 ± 1.6, and thus within the errors of the corrected McGilchrist et al. source counts.

Figure 8 presents the number of objects in the TOOT00 sample compared to the 7C objects in the same sky area that have flux density limits above 100 mJy at 151 MHz. This histogram shows that 47 out of the 56 objects from the 7C that have $S_{151\mathrm{MHz}} \gtrsim 100$ mJy are included in TOOT00 sample. Figure 8 shows that almost all the difference is confined to the lowest (95 mJy $< S_{151\mathrm{MHz}} <$ 115 mJy) bin for reasons explained in Section 2 and caption to Figure 1.

In Figure 8 we also plot the flux density distribution from the S^3-SEX simulation scaled down to the 0.0015-sr sky area of the TOOT00 sample. We note that the S^3-SEX simulation, with or without corrections similar to the McGilchrist et al. (1990) work, significantly under-predicts the 7C objects in the TOOT00 area in the lowest flux density bins (95 mJy $< S_{151\mathrm{MHz}} <$ 115 mJy).

We suspect that the Eddington bias in the 7C sample (which includes sources extracted from the 7C maps with signal-to-noise ratios as low as ~ 3; see Table 1) causes the spike in the lowest-$S_{151\mathrm{MHz}}$ bin, meaning that the exclusion of faint 'off-edge' sources (Section 2) in the construction of the TOOT00 survey, brings the flux density distribution closer in line between data and simulation. Modelling of the Eddington bias would be possible, given a known source count significantly deeper than the 7C survey, but this will only become available with the advent of LOFAR (e.g. Röttgering 2007).

We hereafter assume that the TOOT00 sample is close to the true distribution (i.e. the one in the TOOT00 area in the limit of infinite signal-to-noise ratio in the low-frequency survey data). We compare this to the S^3-SEX distribution in flux density and other properties without any, in any case highly uncertain, corrections for incompleteness and Eddington bias. With these assumptions, there is a reasonable agreement between the 47 TOOT00 radio sources and the 40 ± 8.8 objects expected from the simulation (the standard deviation is a combination of Poisson errors and genuine field-to-field variations due to the large scale structure enclosed in the S^3-SEX simulation).

In Figure 9 we compare the measured TOOT00 redshift distribution and that predicted by the S^3-SEX simulation. We calculated the two-sided Kolmogorov-Smirnov (K-S test) statistic and associated probability to investigate whether data and simulation are consistent (Press et al. 1993). The maximum deviation between the cumulative distribution

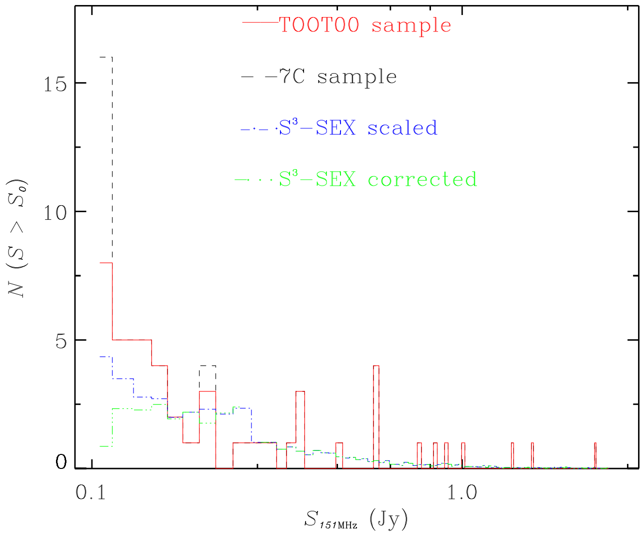

Figure 8. Histogram of the flux density distribution for objects in the TOOT00 sky area with flux density $S \gtrsim$ 100 mJy at 151 MHz. The black dashed line shows the 56 sources in the 7C sample that lie inside the area marked by the red circles in Figure 1. The red solid line indicates the 47 TOOT00 radio sources. The blue dotted-dashed histogram is the S^3-SEX simulation scaled down to 0.0015 sr. This includes $\sim$ 40 objects. The green 3-dotted-dashed line presents the S^3-SEX simulation scaled down to 0.0015 sr in which the lower bins ($S_{151\mathrm{MHz}} < 0.25$ Jy) are weighted according to Table 5 of the McGilchrist et al. (1990), plus an additional correction takes into account the missing 7C objects in TOOT00. The final number of objects in the scaled and corrected S^3-SEX simulation is $\sim$ 33.

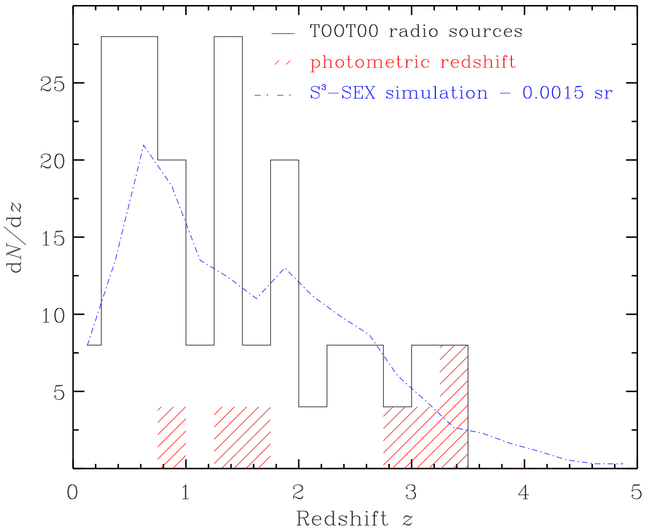

Figure 9. Histogram of the redshift distribution for the 47 TOOT00 radio sources with median $z_{\mathrm{med}} = 1.287$ (85% spectroscopic and 17% photometric redshifts, black & red lines respectively). The binning on the redshift axis is dz = 0.25. We overplot model predictions from the S^3-SEX simulation for an area of 0.1212 sr, which is scaled down to an area of 0.0015 sr (blue dotted-dashed line) to match the TOOT00 sky area, and includes $\sim$ 40 objects.

of the data and simulation is $\sim$ 0.12 and the significance level of the K-S test is $\sim$ 44.46%. This result suggests that the real TOOT00 and simulated S^3-SEX samples are consistent.

As a further note on the radio-source population, Figure 7 demonstrates that there is a broad agreement between the TOOT00 radio/optical classes of the TOOT00 data and the S^3-SEX simulation, allowing for known limitations in the simulation. In the TOOT00 sample (Figure 7a) we have 47 objects: 22 FRIIs, 14 FRIs, 4 Q-Fs and 7 CSS radio sources; one of the CSS objects is in fact a GPS radio source. The distribution on the right of Figure 7 shows the S^3-SEX simulation, scaled down to 0.0015 sr, which includes $\sim$ 40 objects: $\sim$ 18 high-L_{151} objects, $\sim$ 21 low-L_{151} objects, $\sim$ 0.1 RQQs and $\sim$ 0.2 normal galaxies and $\sim$ 1 GPS; the normal galaxies and RQQs are not plotted in this figure for clarity.

5 CONCLUSIONS

In this paper we presented optical spectroscopy and optical and near-IR imaging on the 47 TOOT00 radio-source sample from a survey covering 0.0015 sr. We have 85% spectroscopic completeness and we estimate photometric redshifts for the rest of the sample using the photometric redshift code HyperZ or the $K_{\mathrm{W}} - z$ relation from Willott et al. (2003). The key points of our analysis are:

- The median redshift for the whole sample is $z_{\mathrm{med}} \sim$ 1.25. This value is slightly higher than the the $z \sim 1.1$ of the 6CE and 7CRS surveys.
- The fraction of ‘naked’ quasars is $0.13 < f_{\mathrm{q}} < 0.25$ above the FRI/FRII break in the 151-MHz radio luminosity and below that break, the quasar fraction drops towards zero. These are similar results to the 3CRR, 6CE, 7CRS redshift surveys.
- The total number of TOOT00 objects and their distribution are consistent with a simulated distribution of radio sources from the SKADS Simulated Skies Semi-Empirical Extragalactic Database (S^3-SEX), simulations extrapolated from the 3CRR/6CE/7CRS datasets.
- The radio structures of the TOOT00 sample are broadly in line with those in the S^3-SEX sample with small exceptions, like the lack of core-jet sources in the simulation.
- There is observational evidence from TOOT00 that the ‘FRI/II’ structural divide depends on cosmic epoch. We conclude that there must be some cosmic evolution between redshifts $z = 0$ and $z = 1$.

It is interesting that the S^3-SEX 'FRIs' (or low-L_{151} sub-population) include objects in-between the classic FRI/II break and the RLF, which in real samples include some CD sources as well as the FD sources counted as FRI in this study.

- The low fraction of flat-spectrum objects in TOOT00 of 6% can be attributed to the low-frequency selection of the radio sample. The TOOT00 radio-source sample also includes 2 core-jet objects with radio spectral indices $\alpha \sim 0.5$.

ACKNOWLEDGEMENTS

EV would like to thank her parents for private funding. We would like to thank the anonymous referee for useful comments. We would like to thank Cristina Fernandes for help with WHT observing in 2009, and Matt Jarvis, Chris Simpson and Dan Smith for allowing this to happen. We also thank Gavin Dalton for help accessing ODT data.

REFERENCES

Alexander, P., Leahy, J. P., 1987, MNRAS, 225, 1
Antonucci, R., 1993, ARA&A, 31, 473
Augusto, P., Wilkinson, P. N., Browne, I. W. A., 1998, MNRAS, 299, 1159
Best, P. N., Kauffmann, G., Heckman, T. M., Brinchmann, J., Charlot, S., Ivezić, Ž., White, S. D. M., 2005, MNRAS, 362, 25
Best, P. N., Kaiser, C. R., Heckman, T. M., Kauffmann, G., 2006, MNRAS, 368, 67
Bird, J. C., Martini, P., Kaiser, C. R., 2008, ApJ, 676, 147
Blundell, K. M., Kuncic, Z., 2007, ApJ, 668, 103
Bolzonella, M., Miralles, J. M., Pell, R., 2000, A&A, 363, 476
Bruzual, A. G., Charlot, S., 2003, MNRAS, 344, 1000
Calzetti, D., Armus, L., Bohlin, R. C., Kinney, A. L., Koornneef, J., Strorchi-Bergmann, T., 2000, ApJ, 533, 682
Cohen, A. S., Lane, W. M., Cotton, W. D., Kassim, N. E., Lazio, T. J. W., Perley, R. A., Condon, J. J., Erickson, W. C., 2007, AJ, 134, 1245
Condon, J. J., Cotton, W. D., Greisen, E. W., Yin, Q. F., Perley, R. A., Taylor, G. B., Broderick, J. J., 1998, AJ, 115, 1693
Dunlop J. S., Peacock J. A., 1990, MNRAS, 247, 19
Eales, S., Rawlings, S., Law-Green, D., Cotter, G., Lacy, M., 1997, MNRAS, 291, 593
Emonts, B., Morganti, R., Oosterloo, T., van Gorkom, J., 2008, proceedings of "The Modern Radio Universe: From Planets to Dark Energy Conference", Manchester UK
Fanaroff, B. L., Riley, J. M., 1974, MNRAS, 167, 31
Gopal-Krishna & Wiita P. J., 2001, ApJ, 560, L115
Hales, S. E. G., Riley, J. M., Waldram, E. M., Warner, P. J., Baldwin, J. E., 2007, MNRAS, 382, 1639
Heywood, I., Blundell, K. M., Rawlings, S., 2007, MNRAS, 381, 1093
Hill, G. J., Nicklas, H. E., MacQueen, P. J., Tejada, C., Cobos Duenas, F. J., Mitsch, W., 1998, Proc SPIE, 3355, 37
Hill, G., Rawlings, S., 2003, NewAR, 47, 373
Howarth, I. D., 1983, MNRAS, 203, 301
Howatt, R. S. et al., 2004, "The commissioning of and first results from the UIST imager spectrometer", In Proc Spie 5492, UV and Gamma-Ray Space Telescope Systems, eds. Hasinger G, Turner M.J., p.1160
Jackson, N., Rawlings, S., 1997, MNRAS, 286, 241
Jarvis M. J., Rawlings S., Willott C. J., Blundell K. M., Eales S. A., Lacy M., 2001, MNRAS, 327, 907
Kaiser, C. R., Best, P. N., 2007a, MNRAS, 381, 1548
Kaiser, C. R., Best, P. N., 2007b, hvcg conf, 222
Laing, R.A., Riley, J.M., Longair, M.S., 1983, MNRAS, 204, 151
Lavalley, M., Isobel, T., Feigelson, E., 1992, ASPC, 25, 245
Longair M.S., 1966, MNRAS, 133, 421
MacDonald, E. C., Allen, P., Dalton, G., Moustakas, L. A., Heymans, C., Edmondson, E., Blake, C., Clewley, L., Hammell, M. C., Olding, E. et al. 2004, MNRAS, 352, 1255
McGilchrist, M. M., Baldwin, J. E., Riley, J. M., Titterington, D. J., Waldram, E. M., Warner, P. J., 1990, MNRAS, 246, 110
McLure, R. J., Willott, C. J., Jarvis, M. J., Rawlings, S., Hill, G. J., Mitchell, E., Dunlop, J. S., Wold, M. , 2004, MNRAS, 351, 347
Owen, F. N., Laing, R. A., 1989, MNRAS, 238, 357
Paragi, Z., Frey, S., Fejes, I., Venturi, T., Porcas, R. W., Schilizzi, R. T., 2000, PASJ, 52, 983
Parma, P., Murgia, M., de Ruiter, H. R., Fanti, R., 2002, NewAR, 46, 313
Press, W. H., Teukolsky, S. A., Vetterling, W. T., Flannery, B. P., Lloyd, C., Rees, P., 1993, Numerical Recipes, Cambridge U Press
Rawlings, S., Eales, S. A., Lacy, M., 2001, MNRAS, 322, 523
Rawlings, S., Eales, S., Warren, S., 1990, MNRAS, 243, 14
Rawlings, S. 2002, IAUS, 199, 34
Rawlings, S., 2003, NewAR, 47, 397
Rees, N., 1990, MNRAS, 244,233
Riley, J. M. W., Waldram, E. M., Riley, J. M., 1999, MNRAS, 306, 31
Roche, et al., 2002, Proc Spie 4841 Instrument Design and Performance for Optical/IR Ground Based Telescopes, eds. M Iye & A.F. Moonwood
Röttgering, H., 2007, AAS, 210, 6604
Sawada-Satoh, S., Inoue, M., Shibata, K. M., Kameno, S., Migenes, V., Nakai, N., Diamond, P. J., 2000, PASJ, 52, 421
Snellen, I. A. G., 2008, proceedings of the symposium "Approaching Micro-Arcsecond Resolution with VSOP-2: Astrophysics and Technology" (ISAS/JAXA, Sagamihara, Japan, 3-7 Dec 2007)
Snellen, I. A. G., Schilizzi, R. T., van Langevelde, H. J., 2000, MNRAS, 319, 429
Tabor, G., Binney, J., 1993, MNRAS, 263, 323
Teerikorpi, P., 2004, A&A, 424, 73
Vardoulaki, E., Rawlings, S., Simpson, C., Ivison, R. J., Ibar, E., 2008, MNRAS, 387, 505
Willott, C. J., Rawlings, S., Blundell, K. M., Lacy, M., 1998, MNRAS, 300, 625
Willott, C. J., Rawlings, S., Blundell, K. M., Lacy, M., 1999, MNRAS, 309, 1017
Willott, C. J., Rawlings, S., Blundell, K. M., Lacy, M.,

2000, MNRAS, 316, 449

Willott, C. J., Rawlings, S., Blundell, K. M., Lacy, M., Eales, S. A., MNRAS, 2001, 322, 536

Willott, C. J., Rawlings, S., Jarvis, M. J., Blundell, K. M., 2003, MNRAS, 339, 173

Wilman, R. J., Miller, L., Jarvis, M. J., Mauch, T., Levrier, F., Abdalla, F. B., Rawlings, S., Kloeckner, H. -R., Obreschkow, D., Olteanu, D., Young, S., 2008, MNRAS, 388, 1335

Yamada M., Fujita Y., 2001, ApJ, 553, L145

APPENDIX A: NOTES ON THE TOOT00 RADIO SOURCES

TOOT00_1140 is a galaxy 'G' and is resolved in the K-band. This FD radio source (the two components are not compact in the A-array map) is at a spectroscopic redshift $z = 0.911$. The NVSS data suggest the presence of diffuse radio emission that is absent in the A/B-array maps. Due to lack of ODT optical photometry, we measure the optical magnitudes directly from the spectrum, as explained in Section 3. The photometric redshift from HyperZ seems to be a good fit to the data (see Figure A1), although it does not agree perfectly with the spectroscopic one.

TOOT00_1099 is a possible TJ radio source, and a galaxy resolved in the near-infrared K-band. The optical spectrum reveals only one clear emission line at 8937Å, which is extended over ~ 5 arcsec ≈ 43 kpc. We believe that this is $[\mathrm{OII}]_{\lambda 3727}$ and not $[\mathrm{OIII}]_{\lambda 5007}$, since the weaker of that doublet, $[\mathrm{OIII}]_{\lambda 4959}$, does not appear in the spectrum. The [OII] emission line suggests a redshift $z = 1.397$. We are not concerned that other strong lines, like [CII], are not visible, since they fall near strong sky lines in the blue part of the spectrum. No other expected weak lines can be identified in the spectrum. The photometric redshift values estimated from HyperZ and the $K_{\mathrm{W}} - z$ differ from the spectroscopic value implying an under-luminous galaxy in which the 4000 Å break has not been securely identified in the SED.

TOOT00_1125 is a spectroscopically confirmed quasar at redshift $z = 1.916$, which is unresolved in the K-band. The B-array radio map reveals a CD radio source. The photometric redshift from HyperZ does not agree with the spectroscopic, and the $K_{\mathrm{W}} - z$ relation underestimates the photometric redshift, presumably, in both cases, because of a non-stellar contribution to the K-band.

TOOT00_1143 is a FD radio galaxy (the hot spots at the A-array radio map are not compact) at redshift $z = 0.438$, and is resolved in the K-band. We use the peak flux density at 151 MHz and 1.4 GHz in our analysis, since we believe the integrated flux density is affected by confusion as indicated by a NVSS map of the area. There is a fairly good agreement between spectroscopic and photometric redshifts.

TOOT00_1233 is a quasar at redshift $z = 0.438$ with a flat radio spectral index, and probably a COM radio source. A comparison of the VLA B-array and NVSS flux densities suggests time variability. This is possibly a broad-absorption-line QSO (BALQSO), although the fact that the blue and red spectra were joined where the MgII line is, causes some concern regarding this classification. The offset between the tentative 6000 Å absorption and the MgII resonance line indicates a speed of ≈ 0.1c of the outflow, which is not unreasonable. The BC galaxy templates obviously provide a very poor fit to the photometric data, since the SED is flat, as expected in an unobscured quasar.

TOOT00_1022 is a COM radio source. The optical spectrum taken on August 2000 (PA = 9°) is completely blank and not presented here. The optical spectrum taken on August 2006 (PA = 140°) shows a featureless faint continuum down to 4000 Å, putting a limit on the redshift of $\lesssim 3.4$. HyperZ provides a poor fit to the photometric data; more photometric points are needed in the near-infrared to estimate a more accurate photometric redshift. We use the $K_{\mathrm{W}} - z$ redshift for this object.

TOOT00_1204 is a FD radio galaxy at $z = 0.6395$. The high value of the NVSS flux density is not due to confusion, since there are no nearby radio sources in a 2-arcmin radius; significant amount of flux is invisible in the A- and B-array data. Due to the absence of ODT optical photometry we measure the optical flux directly from the spectrum (see Section 3.2). There is a fairly good agreement between spectroscopic and photometric redshifts.

TOOT00_1235 is a spectroscopically confirmed quasar and probably a COM radio source. In Figure A1 we present the A-array VLA map, where the radio structure looks stretched along one axis; this is an artifact caused by bandwidth smearing due to the position of the radio source at the edge of the VLA primary beam (see Figure 1). We classify this quasar as a Q-F?, since the value of α is close to 0.5, which also suggests that this is a core-jet radio source. There is a fairly good agreement between spectroscopic and $z_{K_{\mathrm{W}}-z}$ redshifts, contrary to the z_{BC} one; this result is expected since the BC templates do not fit a quasar SED well.

TOOT00_1224 is a compact radio source; the A-array map is bandwidth smeared since the object is at the edge of the VLA primary beam (see Figure 1). Two optical spectra taken at different PAs and with different slit widths (Table 2) are completely blank. As the photometric redshift indicates, this is probably due to the faintness of the object. We use the $z_{K_{\mathrm{W}}-z}$ redshift for our calculations since the photometric z_{BC} redshift is highly uncertain. As can be seen from Figure A1, the optical magnitudes from ODT are 'bright', but yet the spectrum is invisible. This can be explained by the fact that in spectroscopy the optical slit only captures a part of the light from the object, while in photometry more of the light gets observed due to the bigger apertures. The optical photometry goes down to $\sim$ 4000 Å, which puts a limit on the redshift of the object of $\lesssim$ 3.4.

TOOT00_1291 is a CD? radio source, since the eastern hotspot is compact in the A-array radio map. The optical spectrum is blank, so we use HyperZ to calculate a photometric redshift. The BC templates do not fit the data well; more near-IR photometric points are needed for a more accurate fit. We use the photometric redshift calculated from the $K_{\rm W} - z$ relation for the analysis.

TOOT00_1107 is a TJ radio galaxy at z = 0.300. The radio map shows a very diffuse source. From the radio overlay in Figure A1 we notice that the extended radio structure is bent backwards as expected if the source of the jets is moving with respect to an intra-cluster medium. We present the secondary best-fit photometric redshift from HyperZ, since that value is closer to the spectroscopic redshift; no reddening law was used to calculate the photometric redshift. The $z_{K_{\rm W}-z}$ does not agree with either spectroscopic or photometric redshifts, implying an intrinsically faint host galaxy.

TOOT00_1180 is probably a rather one-sided CD radio source and a reddened quasar at $z = 1.810$, since the expected broad emission lines (like Lyα and CIV) appear to be narrow in the spectrum of Figure A1. We present the A-array radio map since it reveals the extended structure of the radio source; the radio structure is not bandwidth smeared since the source is close to the VLA pointing position.

TOOT00_1027 is a compact radio source at z = 0.890, a point source at K and a possible GPS object, since it has an inverted radio spectral index. This spectral turnover might be caused by synchrotron self-absorption (e.g. Snellen et al. 2000) or free-free absorption (e.g. Sawada-Satoh et al. 2000). Apparent extended radio components in the maps of this source are almost certainly artifacts due to imperfect calibration. The photometric redshift calculated from the $K_{\rm W} - z$ is very high compared to the other two redshifts, implying a faint host galaxy. This agrees with the findings of Snellen (2008) that GPS radio sources correspond to fainter hosts than other radio sources.

TOOT00_1195 is a CD radio source with prominent hot spots at the end of the radio structure. The optical spectrum shows only a faint continuum without clear emission lines or any break. HyperZ provides a very poor fit to the data. We use $z_{K_{\rm W}-z}$ in the analysis.

TOOT00_1069 is a possible COM (or marginally extended) radio source and a spectroscopically confirmed quasar at $z = 2.300$ with prominent broad emission lines. Obtaining this redshift was a triumph of 'blind spectroscopy' (Rawlings, Eales & Warren 1990) as a wide (4-arcsec) slit was placed North-South in an attempt to cover all plausible radio components. The A-array radio map is bandwidth smeared, which is not helpful in making a reliable radio classification. We classify it as a compact-steep-spectrum quasar (CSS-Q), as indicated by the steep radio spectral index, $\alpha_{151\rm MHz}^{1.4\rm GHz} = 1.49$, and the optical spectrum of a quasar (see Figure A1). Both photometric redshifts are unrealistic as expected if the SED is dominated by non-stellar emission. We assign an upper limit to the K magnitude, since the signal-to-noise ratio is not high enough to distinguish any associated K object from the background noise.

TOOT00_1094 is a compact radio source with faint continuum and a probable emission line at 7040 Å in the red part of the optical spectrum. The photometric redshifts suggest that this emission line could be MgII, giving a redshift $z = 1.516$. The photometric redshift fit from HyperZ could be improved if more photometric points between I and K were available.

TOOT00_1149 has a TJ radio structure. This radio galaxy is at $z = 0.260$, where spectroscopic and photometric redshifts seem to be in excellent agreement. We don't have a K-band image from UKIRT for this object, so we use the K image from the ODT survey.

TOOT00_1298 is a TJ radio source probably at $z = 1.287$ from likely [OII] and associated red continua in the spectrum. We do not trust the photometric redshift estimated from HyperZ, since only three photometric points were used in the fit. The $z_{K_{\rm W}-z}$ value is slightly different from the spectroscopic and photometric redshift.

TOOT00_1200 is a CD radio source with prominent hot spots at both ends of the radio structure, that are visible in both B- and A-array VLA maps. The optical spectrum has a plethora of narrow emission lines, placing the object at redshift z = 0.691. There is a blue excess in the SED.

TOOT00_1215 is a galaxy at $z = 0.278$ with a compact radio component coincident with the galaxy and radio emission slightly elongated to the west; hence we classify it as TJ?. The value of the photometric redshift from the $K_{\rm W} - z$ is very close the spectroscopic one. The redshift calculated from HyperZ has a much higher value, probably because more photometric points are needed for an accurate fit; no reddening law was used to estimate $z_{\rm BC}$. We don't have a K-band image from UKIRT for this object, so we use the K image from the ODT survey.

TOOT00_1240 is a large CD radio source $\sim$ 2.5 arcmin long, possibly at spectroscopic redshift z = 2.543?. The exposure times used in the first attempt at spectroscopy (August 2000) of this object were accidentally far too short to detect it. The fact that the K position of the object is close to a spectroscopically confirmed M-star (RA: 00 13 05.2 & Dec: +36 01 48.1; marked with 'M' in Figure A1) also makes it hard to get a photometric redshift. We managed to get a spectrum of the M-star and the bright galaxy south-west of the object ID, marked with 'G' in Figure A1, at z = 0.191. In August 2004 we targeted the object north of the west radio lobe with an associated compact radio component (see Figure A1) which is a galaxy at $z = 0.556$. The blue spectrum from the August 2009 observing run has continuum emission blueward of 4290 Å, but, as this becomes increasingly contaminated by leakage from the M-star at redder wavelengths, it is hard to assess the colour of the object. We show in Figure A1 only the blue-arm spectrum in which there are possible Lyα and NV$_{\lambda\lambda1240}$ lines. Along the slit we measured a redshift of $z = 0.193$ for a galaxy close to the western hotspot at RA: 00 13 01.36 & Dec: +36 01 57.04. The $K-$band image of this area excludes the area where the east lobe is located. In Figure A1 we present the $K-$band/radio B-array overlay. Below it, we give a DSS image of the area, where the double radio structure is clearly visible. The photometric redshift from HyperZ is not reliable: more photometric points are needed to provide a better fit to the SED. The value of photometric redshift from the $K_{\rm W} - z$ relation ($z_{K_{\rm W}-z} = 2.185$) is close to the tentative spectroscopic redshift.

TOOT00_1289 is CD radio source, since the radio hot spots do not disappear in the A-array VLA map. The optical spectrum indicates a possible redshift of $z = 1.784$ although, if true, there are no hints of Lyα at the expected location. The photometric redshift from HyperZ is highly uncertain; more photometric points are needed for an accurate fit.

TOOT00_1072 is a giant elliptical galaxy with a CD radio structure, since the compact hot spots are also visible in the A-array map, and a clear absorption spectrum, suggesting a spectroscopic redshift $z = 0.577$. We have fairly good agreement between photometric and spectroscopic redshifts, and the best-fit BC template fits the photometric data points well.

TOOT00_1134 is a radio galaxy at $z = 0.311$. The photometric redshift from HyperZ is a good fit to the data and agrees with the spectroscopic value; no reddening law was used in the calculations. The integrated radio flux densities include a contribution from a separate radio source to the south-east (as indicated by a NVSS map of the area); this second object is associated with a galaxy that, from its SED, may well be in the same cluster. We use the peak flux densities at 74 MHz, 151 MHz for our analysis. For the 1.4-GHz flux density we use the value measured from the B-array VLA map using the package AIPS: we use a box around the radio source, excluding the radio source to the south-east of the object.

TOOT00_1244 is a spectroscopically confirmed quasar at $z = 1.358$ and a compact radio source. We classify it as a Q-F?, since the radio spectral index has a value close to 0.5, which also suggests this may be a core-jet radio source. The photometric redshift is not reliable, as is expected if its blue SED is dominated by non-stellar emission. We don't have a K-band image from UKIRT for this object, so we use the K image from the ODT survey.

TOOT00_1066 is a FD radio source, since the double radio structure seen in Figure A1 disappears in the A-array radio map. The spectroscopic redshift is probably $z = 0.926$, although different from the photometric redshifts. We use the peak flux densities at 151 MHz and 1.4 GHz, due to confusion as indicated by a NVSS map of the area.

TOOT00_1261 is a spectroscopically confirmed quasar that appears to be reddened, since the expected broad emission lines, like Lyα and CIV, are broad only in their wings. The A-array radio map reveals a CD radio structure. The apparent offset between the K and radio positions (Figure A1) is within the uncertainty of the astrometry. The SED secondary best-fit is surprisingly, and presumably fortuitously, good considering the BC templates are not expected to fit quasar SEDs very well. We use the peak flux densities at 151 MHz and 1.4 GHz, due to confusion as indicated by the NVSS map of the area.

TOOT00_1252 is a possibly one-sided radio source; we classify it as CD?. The west 'lobe' is $\sim$ 45 arcsec from the 'core' which may be a true core plus a short eastern lobe ($S_{\rm 1.4GHzint} = 18.9$mJy and $S_{\rm 1.4GHzpeak} = 14.4$ mJy). The K detection is $2.7''$ South-West of the peak radio position. We assign an upper limit to the K magnitude measured from the K-band image, since the signal-to-noise ratio is not high enough in order to distinguish any K object from the background. The optical spectrum taken on August 2000 (at PA = 109°) is blank in the blue and shows signs of continuum in the red. The spectrum taken on July 2004 (at PA = 265°) is completely blank, with confidence in correct pointing as the slit was pointed in a way to observe as many objects as possible along the slit. Deeper observations could provide a reliable optical spectrum and an accurate optical position for the object. The HyperZ fit gives only a lower limit to the photometric redshift since only upper limits are used in the calculations; more photometric points are needed to improve the fit. We use the photometric redshift from the $K_{\rm W} - z$ relation, since the photometric redshift from HyperZ is unreliable.

TOOT00_1214 is a one-sided radio source classified as CD?. It is a point source at K and a seemingly reddened quasar at $z = 3.081$. In the optical spectrum we can see evidence of a Lyα absorption system below 5000 Å. There is a very poor agreement between photometric and spectroscopic redshifts, as expected for a quasar SED. We use the peak flux densities at 151 MHz and 1.4 GHz, due to confusion as indicated by a NVSS map of the area.

TOOT00_1152 is a CD radio source with prominent hot spots at both ends of the radio structure, that do not disappear in the A-array map. The object most likely associated with the radio structure gives a weak featureless faint optical continuum in the spectroscopy, which puts a limit on the redshift of the object of $\lesssim 3$. We use the $K_{\rm W} - z$ redshift for our calculations since the formal output of the HyperZ code is clearly a very poor fit.

TOOT00_1129 is a CD radio source, since the hot spots do not disappear in the A-array map, and a possible reddened quasar, as indicated by the narrow Lyα and CIV lines. Neither of the two photometric redshifts agree with the spectroscopic value, as expected if non-stellar (e.g. dust scattered light from the obscured quasar) light is dominating the SED. The formal output of the HyperZ code is clearly a very poor fit.

TOOT00_1090 is a FD radio source, as can be seen by the diffuse radio structure in Figure A1. This galaxy is at redshift $z = 0.201$. There is a very good agreement between spectroscopic and photometric redshifts.

TOOT00_1267 is a CD radio source, since the radio hot spots are present in both the A- and B-array radio maps. The optical spectrum places this object at redshift $z = 0.968$. There is a fairly good agreement between photometric and spectroscopic redshifts.

TOOT00_1188 is a CD radio source (the radio hot spots do not disappear in the A-array map) with a spectroscopic redshift $z = 1.417$. The HyperZ fit is fairly good; more near-IR photometric points are needed for a more accurate fit. The redshift calculated from the $K_{\rm W} - z$ relation is slightly higher than the spectroscopic value.

TOOT00_1196 is the only object in the sample that may be a spurious 7C radio source. Its unusual properties means that if it is real it is a very diffuse 'FD?' radio source since there is no bright radio core nor a bright hot spot near the 7C radio position, as can be seen by the B-array map presented in Figure A1. Due to this fact, we cannot measure the angular size of the radio source. Any radio emission is probably associated with the galaxy shown in Figure A1, close to the 7C radio position. Since any radio source in the B-array map has a flux density below the detection limit, we use a 2σ detection from the NVSS, recalling that the rms noise of the NVSS is 0.45 mJy beam^{-1}. This gives a very steep radio spectral index of > 2.1. The object is not detected at 74 MHz, marginally surprising given a predicted detection at $\sim 4.5\sigma$. We cannot rule out the possibility that the 4.4σ 7C detection is spurious. Assuming the source is real and the galaxy ID shown in Figure A1, optical photometry provides only R- and I-band images, while it was not observed in the B-band, so the HyperZ fit is uncertain. The optical spectrum is blank in the blue, but shows a featureless continuum in the red with no clear lines. This object is classified as a possible galaxy G?, and we use the redshift calculated from the $K_{\rm W} - z$ for our analysis.

TOOT00_1173 is a TJ radio source at $z = 0.332$, with diffuse radio structure. The HyperZ fit is good and there is a good agreement between photometric and spectroscopic redshifts.

TOOT00_1228 is a COM radio source probably at redshift $z = 1.135$, and a point source at K. There is poor agreement between spectroscopic and photometric redshifts.

TOOT00_1034 is TJ radio source at $z = 0.580$, where the east radio emission is very diffuse. The photometric redshift agrees with the spectroscopic one, although more photometric points could improve the HyperZ estimate.

TOOT00_1255 is probably a CD radio source since the hot spots do not disappear in the A-array radio map. Here we present the B-array map (see Figure A1). This galaxy is at redshift $z = 0.582$, which does not agree well with the photometric redshift. The one estimated from the $K_{\rm W} - z$ relation has a higher value, presumably because it is an unusually underluminous galaxy.

TOOT00_1048 is a CD radio source since the radio hot spots do not disappear in the A-array map, with a secure redshift $z = 1.943$. The optical spectrum indicates a reddened quasar and it is unresolved in the K-band. The ID in the K is 0.6 arcsec away from the centre of the classical double radio structure, which is within the uncertainty of the astrometry and the radio position. We classify it as a G?. We do not trust the photometric redshift from HyperZ since we have only four photometric points for the calculation.

TOOT00_1029 is probably a COM radio source; the A-array map is bandwidth smeared and isn't presented here. The redshift estimated from HyperZ is close to the spectroscopic redshift; no reddening law was used in that calculation. The $z_{\rm K-z}$ estimate does not agree with the spectroscopic redshift.

TOOT00_1115 is probably a TJ radio source, since both A- and B-array radio maps are extended; here we present the A-array map. McLure et al. (2004) classify this object as a low-excitation-galaxy LEG (see Jackson & Rawlings 1997). The optical spectrum gives a secure redshift $z = 0.416$, and there is very good agreement with the photometric redshift.

TOOT00_1132 is possibly a TJ? radio source and a galaxy at $z = 0.183$. There is a fairly good agreement between the spectroscopic and photometric $z_{\rm BC}$ redshifts, although the $z_{\rm K-z}$ value is slightly higher.

TOOT00_1250 is a spectroscopically confirmed quasar at $z = 1.350$, with broad emission lines in the optical spectrum. The A- & B-array radio maps reveal a CD? radio structure; the A-array map shows clearly that both hot spots are compact (see Figure A1). The object is unresolved in the K-band. The value estimated from HyperZ disagrees with the spectroscopic and the $z_{\rm K-z}$ redshifts due to a poor fit to too few photometric data points.

TOOT00_1268 is a COM radio source at redshift $z = 2.015$, and it might be a reddened quasar. We classify it as a G? optically and a Q-F in the radio for a quasars with a flat radio spectral index. The A-array radio map is bandwidth smeared at the source position; we do not present here. The fact that there is no visible sign of a 4000 Å break spectroscopically and that the SED is relatively flat, makes it hard to estimate an accurate photometric redshift.

TOOT00_1251 is a CD radio source at $z = 2.490$, since the radio hotspots do not disappear in the A-array map. The Lyα line is obvious in the 2D optical spectrum. We do not trust the photometric redshift from HyperZ due to large errors on the photometry. The $z_{K_{\rm W}-z}$ value agrees with the tentative spectroscopic value.

TOOT00_1203 is a small CD? radio source at redshift $z = 1.397$. The photometric redshifts are slightly lower than the spectroscopic value. More photometric points could improve the HyperZ fit.

Table A1. Optical and near-IR photometry for the 47 TOOT00 radio sources that was used to calculate photometric redshifts with HyperZ: U, B, V, R and I, $2''$ Vega magnitudes are from the ODT survey (MacDonald et al. 2004) or they are measured from the spectra of each object (Figure A1) due to lack of imaging; $K-$ photometry was obtained by UKIRT; J^*, H^* and K^* magnitudes are provided by K. Inskip (complete photometry in five different apertures is shown in Table A2); errors on the magnitudes are in brackets below the values. **Column 1** shows the name of the TOOT00 object. In **Columns 2-7** we give $U-$, $B-$, $V-$, $R-$, $I-$band magnitude respectively; the character 's' shows measurement from the spectrum of each object; the character 'o' denotes ODT data. The errors on the magnitudes are shown below each magnitude value. **Columns 7 & 8** show photometry from the 'Inskip' catalogue on the J^*- and H^*-band, respectively, where they were measured with a $4''$ diameter aperture. **Column 9** presents $K-$band photometry from UKIRT measured with a $4''$ diameter aperture or the one from the 'Inskip' catalogue (see Section 2) marked with an '*'; the character 'o' denotes the value is provided by the ODT. Note: In the HyperZ photometric redshift calculation, all errors less than 10% on the near-IR magnitudes were taken as 10%.

(1)	(2)	(3)	(4)	(5)	(6)	(7)	(8)	(9)
Object	U (mag)	B (mag)	V (mag)	R (mag)	I (mag)	J^* (mag)	H^* (mag)	K (mag)
TOOT00_1140			25.2^{s}	22.8^{s}	21.0^{s}	18.8	18.0	17.0^{*}
			(0.38)	(0.38)	(0.38)	(0.08)	(0.06)	(0.04)
TOOT00_1099	23.3^{s}	23.2^{s}	22.1^{s}	21.1^{s}	20.2^{s}	18.6	17.5	16.5^{*}
	(0.38)	(0.38)	(0.38)	(0.38)	(0.38)	(0.07)	(0.04)	(0.04)
TOOT00_1125	17.6^{s}	18.0^{s}	17.6^{s}	17.4^{s}	17.0^{s}			15.6
	(0.38)	(0.38)	(0.38)	(0.38)	(0.38)			(0.01)
TOOT00_1143	23.0^{s}	22.8^{s}	21.3^{s}	20.1^{s}	19.2^{s}			16.0
	(0.38)	(0.38)	(0.38)	(0.38)	(0.38)			(0.01)
TOOT00_1233	18.9^{s}	19.1^{s}	18.6^{s}	18.3^{s}	17.8^{s}			15.3
	(0.38)	(0.38)	(0.38)	(0.38)	(0.38)			(0.01)
TOOT00_1022	25.7^{s}	$>26.2^{s}$	25.3^{s}	24.4^{s}	$>24.6^{s}$			19.4
	(0.23)	(0.23)	(0.23)	(0.23)	(0.23)			(0.19)
TOOT00_1204	22.1^{s}	23.0^{s}	21.7^{s}	20.6^{s}	19.6^{s}			16.3
	(0.38)	(0.38)	(0.38)	(0.38)	(0.38)			(0.01)
TOOT00_1235	20.9^{s}	21.9^{s}	21.6^{s}	21.3^{s}	20.4^{s}	18.8	17.8	17.0^{*}
	(0.38)	(0.38)	(0.38)	(0.38)	(0.38)	(0.09)	(0.05)	(0.04)
TOOT00_1224		25.8^{o}	23.9^{o}	24.1^{o}	24.0^{o}	22.0	20.9	19.7^{*}
		(0.35)	(0.14)	(0.25)	(0.45)	(0.51)	(0.29)	(0.23)
TOOT00_1291	24.6^{s}	23.9^{s}	22.7^{s}	22.1^{s}	21.3^{s}			17.3
	(0.11)	(0.11)	(0.11)	(0.11)	(0.11)			(0.02)
TOOT00_1107	23.9^{s}	23.1^{s}	21.4^{s}	20.8^{s}	20.3^{s}			18.1
	(0.38)	(0.38)	(0.38)	(0.38)	(0.38)			(0.06)
TOOT00_1180	23.6^{s}	23.9^{s}	23.7^{s}	23.0^{s}	22.4^{s}			18.3
	(0.38)	(0.38)	(0.38)	(0.38)	(0.38)			(0.08)
TOOT00_1027		$>26.2^{s}$	24.2^{s}	23.2^{s}	21.7^{s}			19.5
		(0.23)	(0.23)	(0.23)	(0.23)			(0.24)
TOOT00_1195				24.6^{s}	$>24.6^{s}$	19.5	18.9	18.1^{*}
				(0.23)	(0.23)	(0.12)	(0.10)	(0.08)
TOOT00_1069	22.8^{s}	23.3^{s}	22.3^{s}	22.9^{s}	24.0^{s}			> 20.3
	(0.08)	(0.08)	(0.08)	(0.08)	(0.08)			(1.09)
TOOT00_1094	26.1^{s}	25.8^{s}	24.7^{s}	23.6^{s}	23.0^{s}			18.3
	(0.23)	(0.23)	(0.23)	(0.23)	(0.23)			(0.13)
TOOT00_1149	21.0^{s}	20.8^{s}	19.0^{s}	18.4^{s}	17.5^{s}			14.6^{o}
	(0.23)	(0.23)	(0.23)	(0.23)	(0.23)			(0.01)
TOOT00_1298				24.4^{s}	21.1^{s}			17.3
				(0.23)	(0.23)			(0.04)
TOOT00_1200	21.6^{s}	22.9^{s}	22.3^{s}	21.6^{s}	20.5^{s}			17.4
	(0.23)	(0.23)	(0.23)	(0.23)	(0.23)			(0.04)
TOOT00_1215	22.6^{s}	21.7^{s}	20.0^{s}	19.3^{s}	18.7^{s}			15.0^{o}
	(0.38)	(0.38)	(0.38)	(0.38)	(0.38)			(0.01)
TOOT00_1240		22.2	21.7					18.9
		(0.11)	(0.11)					(0.35)
TOOT00_1289	24.8^{s}	$>26.2^{s}$	23.3^{s}	24.1^{s}				17.8
	(0.23)	(0.23)	(0.23)	(0.23)				(0.10)
TOOT00_1072		23.3^{s}	21.6^{s}	20.4^{s}	19.0^{s}			15.7
		(0.11)	(0.11)	(0.11)	(0.11)			(0.02)
TOOT00_1134		21.3^{s}	19.5^{s}	18.5^{s}	17.8^{s}			14.6
		(0.23)	(0.23)	(0.23)	(0.23)			(0.01)

Table A1. (continued)

(1)	(2)	(3)	(4)	(5)	(6)	(7)	(8)	(9)
Object	U (mag)	B (mag)	V (mag)	R (mag)	I (mag)	J^* (mag)	H^* (mag)	K (mag)
TOOT00_1244	$19.9^{\rm s}$	$20.9^{\rm s}$	$20.7^{\rm s}$	$20.3^{\rm s}$	$20.1^{\rm s}$			18.8
	(0.42)	(0.42)	(0.42)	(0.42)	(0.42)			(0.46)
TOOT00_1066				$24.5^{\rm s}$	$22.2^{\rm s}$	19.8	18.7	18.0*
				(0.11)	(0.11)	(0.13)	(0.08)	(0.07)
TOOT00_1066		$25.3^{\rm o}$	$24.6^{\rm o}$	$23.6^{\rm o}$	$22.5^{\rm o}$	19.8	18.7	18.0*
(HyperZ)		(0.29)	(0.05)	(0.05)	(0.05)	(0.13)	(0.08)	(0.07)
TOOT00_1261	$22.5^{\rm s}$	$22.4^{\rm s}$	$21.9^{\rm s}$	$21.9^{\rm s}$	$21.6^{\rm s}$			19.0
	(0.23)	(0.23)	(0.23)	(0.23)	(0.23)			(0.06)
TOOT00_1252				$> 25.4^{\rm s}$	$> 24.6^{\rm s}$			> 19.6
				(0.50)	(0.50)			(0.44)
TOOT00_1214	$22.9^{\rm s}$	$23.5^{\rm s}$	$22.7^{\rm s}$	$22.0^{\rm s}$	$22.0^{\rm s}$			18.6
(HyperZ)	(0.23)	(0.23)	(0.23)	(0.23)	(0.23)			(0.03)
TOOT00_1214	$23.0^{\rm o}$	$24.5^{\rm o}$	$23.3^{\rm o}$	$22.9^{\rm o}$	$22.1^{\rm o}$			18.6
	(0.06)	(0.15)	(0.07)	(0.08)	(0.09)			(0.03)
TOOT00_1152	$24.0^{\rm s}$	$25.7^{\rm s}$	$25.4^{\rm s}$					19.6
	(0.02)	(0.02)	(0.02)					(0.80)
TOOT00_1129	$24.4^{\rm s}$	$24.2^{\rm s}$	$24.0^{\rm s}$	$23.6^{\rm s}$	$23.8^{\rm s}$			20.2
	(0.02)	(0.02)	(0.02)	(0.02)	(0.02)			(1.13)
TOOT00_1090	$20.3^{\rm s}$	$20.0^{\rm s}$	$18.3^{\rm s}$	$17.7^{\rm s}$	$16.9^{\rm s}$			14.5
	(0.38)	(0.38)	(0.38)	(0.38)	(0.38)			(0.01)
TOOT00_1267	$23.5^{\rm s}$	$24.6^{\rm s}$	$24.0^{\rm s}$	$23.0^{\rm s}$	$21.7^{\rm s}$	19.0	18.2	17.1*
	(0.23)	(0.23)	(0.23)	(0.23)	(0.23)	(0.09)	(0.06)	(0.05)
TOOT00_1188	$23.2^{\rm s}$	$23.9^{\rm s}$	$23.5^{\rm s}$	$22.8^{\rm s}$	$22.7^{\rm s}$			18.3
	(0.23)	(0.23)	(0.23)	(0.23)	(0.23)			(0.01)
TOOT00_1196				$24.1^{\rm o}$	$22.4^{\rm o}$			18.4
				(0.20)	(0.12)			(0.11)
TOOT00_1173		$21.7^{\rm s}$	$20.2^{\rm s}$	$19.1^{\rm s}$	$18.3^{\rm s}$			15.3
		(0.38)	(0.38)	(0.38)	(0.38)			(0.02)
TOOT00_1228	$24.1^{\rm s}$	$24.1^{\rm s}$	$22.5^{\rm s}$	$21.8^{\rm s}$	$21.0^{\rm s}$			18.4
	(0.23)	(0.23)	(0.23)	(0.23)	(0.23)			(0.13)
TOOT00_1034	$25.1^{\rm s}$	$24.7^{\rm s}$	$21.6^{\rm s}$	$20.4^{\rm s}$	$19.4^{\rm s}$			16.1
	(0.23)	(0.23)	(0.23)	(0.23)	(0.23)			(0.03)
TOOT00_1255	$23.3^{\rm s}$	$24.6^{\rm s}$	$22.8^{\rm s}$	$21.4^{\rm s}$	$20.3^{\rm s}$	18.6	17.6	16.8*
(HyperZ)	(0.23)	(0.23)	(0.23)	(0.23)	(0.23)	(0.07)	(0.05)	(0.05)
TOOT00_1255		$24.6^{\rm o}$	$22.6^{\rm o}$	$21.5^{\rm o}$	$20.5^{\rm o}$	18.6	17.6	16.8*
		(0.18)	(0.05)	(0.02)	(0.02)	(0.07)	(0.05)	(0.05)
TOOT00_1048	$24.1^{\rm s}$	$25.2^{\rm s}$	$24.1^{\rm s}$					17.5
	(0.11)	(0.11)	(0.11)					(0.16)
TOOT00_1029	$23.8^{\rm s}$	$24.7^{\rm s}$	$23.2^{\rm s}$	$21.8^{\rm s}$	$20.1^{\rm s}$	18.4	17.6	15.9*
	(0.23)	(0.23)	(0.23)	(0.23)	(0.23)	(0.07)	(0.04)	(0.02)
TOOT00_1115	$22.6^{\rm s}$	$23.0^{\rm s}$	$21.6^{\rm s}$	$20.3^{\rm s}$	$19.5^{\rm s}$			15.9
	(0.23)	(0.23)	(0.23)	(0.23)	(0.23)			(0.02)
TOOT00_1132	$20.0^{\rm s}$	$20.3^{\rm s}$	$18.8^{\rm s}$	$18.3^{\rm s}$	$17.6^{\rm s}$			15.0
	(0.38)	(0.38)	(0.38)	(0.38)	(0.38)			(0.01)
TOOT00_1250	$23.7^{\rm s}$	$22.7^{\rm s}$	$22.5^{\rm s}$	$22.0^{\rm s}$	$22.0^{\rm s}$			18.0
(HyperZ)	(0.23)	(0.23)	(0.23)	(0.23)	(0.23)			(0.14)
TOOT00_1250		$22.9^{\rm o}$	$22.5^{\rm o}$	$21.9^{\rm o}$	$22.4^{\rm o}$			18.0
		(0.04)	(0.04)	(0.03)	(0.12)			(0.14)
TOOT00_1268	$23.1^{\rm s}$	$23.8^{\rm s}$	$23.7^{\rm s}$	$22.4^{\rm s}$	$21.0^{\rm s}$			17.6
	(0.38)	(0.38)	(0.38)	(0.38)	(0.38)			(0.11)
TOOT00_1251	$<25.3^{\rm s}$	$26.0^{\rm s}$	$<25.7^{\rm s}$	$23.5^{\rm s}$	$22.8^{\rm s}$			19.1
	(0.23)	(0.23)	(0.23)	(0.23)	(0.23)			(1.30)
TOOT00_1203				$22.4^{\rm s}$	$20.8^{\rm s}$	18.9	18.3	17.4*
				(0.38)	(0.38)	(0.09)	(0.07)	(0.05)

Table A2. Optical and near-IR photometry for the 47 TOOT00 radio sources; errors are in brackets below the values. **Column 1** shows the name of the TOOT00 object. **Column 2** gives the photometric band, where for the $K-$band from UKIRT we also provide the observing date; the J^*-, H^*- and K^*-band data are from the Inksip catalogue; the character 'o' denotes data from the ODT. **Column 3** gives the near-IR position of the object (RA in h m s & Dec in $^{o}\ '\ ''$; J2000.0). **Columns 4-8** present the photometry in different diameter aperture measurements, $3''$, $4''$, $5''$, $8''$ and $9''$ respectively, for near-IR data only. Note that for the optical photometry (see MacDonald et al. 2004) the magnitudes given are not measured in a 3-arcsec diameter aperture, but are given in the same column due to lack of space.

(1)	(2)	(3)	(4)	(5)	(6)	(7)	(8)
Object	Band	near-IR Position (J2000)	$3''$mag ($3''$ error)	$4''$mag ($4''$ error)	$5''$mag ($5''$ error)	$8''$mag ($8''$ error)	$9''$mag ($9''$ error)
TOOT00_1140	K-UFTI	00 08 30.8 +35 21 48.1	17.1	17.0	16.9	16.8	16.7
	25Jul2000		(0.02)	(0.02)	(0.03)	(0.04)	(0.05)
	J^*		18.9	18.8	18.8	18.6	18.7
			(0.09)	(0.08)	(0.09)	(0.10)	(0.12)
	H^*		18.0	18.0	17.9	17.8	17.8
			(0.06)	(0.06)	(0.06)	(0.08)	(0.09)
	K^*		17.0	17.0	16.9	16.7	16.7
			(0.04)	(0.04)	(0.04)	(0.04)	(0.04)
TOOT00_1099	K-UFTI	00 09 23.7 +35 05 05.5	16.7	16.6	16.5	16.5	16.4
	25Jul2000		(0.01)	(0.02)	(0.02)	(0.03)	(0.04)
	$J03^*$		18.7	18.6	18.5	18.5	18.6
			(0.08)	(0.08)	(0.08)	(0.10)	(0.12)
	$J04^*$		18.8	18.6	18.5	18.4	18.4
			(0.08)	(0.07)	(0.07)	(0.08)	(0.08)
	$H03^*$		17.7	17.5	17.4	17.4	17.3
			(0.04)	(0.04)	(0.04)	(0.05)	(0.05)
	$H04^*$		17.7	17.5	17.4	17.4	17.4
			(0.05)	(0.04)	(0.04)	(0.05)	(0.06)
	K^*		16.7	16.5	16.5	16.4	16.4
			(0.04)	(0.04)	(0.04)	(0.04)	(0.04)
TOOT00_1125	K-UFTI	00 09 36.6 +35 15 43.1	15.7	15.6	15.6	15.5	15.5
	27Jul2000		(0.01)	(0.01)	(0.01)	(0.01)	(0.02)
TOOT00_1143	K-UFTI	00 09 46.9 +35 23 44.8	16.0	[15.8]	[15.7]	[15.5]	[15.5]
	27Jul2000		(0.01)	(0.01)	(0.01)	(0.02)	(0.02)
TOOT00_1233	K-UFTI	00 09 53.2 +35 58 23.4	15.4	15.3	15.2	15.1	15.1
	25Jul2000		(0.01)	(0.01)	(0.01)	(0.01)	(0.01)
TOOT00_1022	K-UFTI	00 10 37.7 +34 41 23.1	19.0	19.4	19.6	20.0	20.0
	25Jul2000		(0.10)	(0.19)	(0.31)	(0.81)	(0.94)
TOOT00_1204	K-UFTI	00 10 40.6 +35 45 48.3	16.4	16.3	16.2	16.1	16.1
	25Jul2000		(0.01)	(0.01)	(0.01)	(0.02)	(0.03)
TOOT00_1235	K-UFTI	00 10 45.5 +35 59 51.3	17.0	16.9	16.8	16.8	16.8
	25Jul2000		(0.02)	(0.02)	(0.02)	(0.04)	(0.05)
	J^*		19.0	18.8	18.8	18.6	18.6
			(0.09)	(0.09)	(0.09)	(0.10)	(0.11)
	H^*		18.0	17.8	17.8	17.6	17.6
			(0.05)	(0.05)	(0.05)	(0.07)	(0.07)
	K^*		17.1	17.0	17.0	16.8	16.8
			(0.05)	(0.04)	(0.04)	(0.04)	(0.05)
TOOT00_1224	B^{o}	00 10 48.87 +35 55 51.5	25.8				
			(0.35)				
	V^{o}	00 10 49.24 +35 55 51.2	23.9				
			(0.14)				
	R^{o}	00 10 49.16 +35 55 51.4	24.1				
			(0.25)				
	I^{o}	00 10 49.00 +35 55 51.3	24.0				
			(0.45)				
	K-UFTI	00 10 48.8 +35 55 49.0	(too faint to measure)				
	25Jul2000						
	K-UFTI	00 10 48.8 +35 55 49.0	19.8	19.5	19.4	19.9	20.1
	8Sept2004		(0.12)	(0.13)	(0.14)	(0.41)	(0.56)

Table A2. (continued)

(1)	(2)	(3)	(4)	(5)	(6)	(7)	(8)
Object	Band	near-IR Position (J2000)	3″mag (3″ error)	4″mag (4″ error)	5″mag (5″ error)	8″mag (8″ error)	9″mag (9″ error)
TOOT00_1224	$J03^{*}$		22.4	22.2	21.5	21.4	21.2
			(0.79)	(0.88)	(0.63)	(1.05)	(1.01)
	$J04^{*}$		22.1	22.0	22.6	22.7	21.6
			(0.46)	(0.51)	(1.00)	(1.98)	(0.90)
	$H03^{*}$		21.0	20.5	20.1	19.6	19.5
			(0.33)	(0.29)	(0.27)	(0.32)	(0.33)
	$H04^{*}$		21.1	20.9	20.6	20.7	20.8
			(0.27)	(0.29)	(0.28)	(0.58)	(0.76)
	K^{*}		19.8	19.7	19.5	19.4	19.5
			(0.21)	(0.23)	(0.23)	(0.39)	(0.51)
TOOT00_1291	K-UIST	00 10 51.4 +36 28 29.7	17.4	17.3	17.3	17.2	17.2
	26Jan2003		(0.02)	(0.02)	(0.02)	(0.04)	(0.05)
	K-UFTI	00 10 51.4 +36 28 29.6	17.3	17.2	17.0	17.2	17.2
	15Sep2004		(0.03)	(0.04)	(0.04)	(0.10)	(0.10)
TOOT00_1107	$B^{\rm o}$	00 11 12.22 +35 07 21.0	26.7				
			(1.21)				
	$V^{\rm o}$	00 11 12.45 +35 07 20.6	23.9				
			(0.24)				
	$R^{\rm o}$	00 11 12.47 +35 07 20.8	23.4				
			(0.14)				
	$I^{\rm o}$	00 11 12.40 +35 07 20.2	22.6				
			(0.12)				
	K-UFTI	00 11 12.30 +35 07 20.6	18.3	18.1	18.0	18.1	18.0
	25Jul2000		(0.05)	(0.06)	(0.07)	(0.13)	(0.14)
TOOT00_1180	$B^{\rm o}$	00 11 12.94 +35 38 0.3	23.5				
			(0.09)				
	$V^{\rm o}$	00 11 12.94 +35 38 0.3	23.5				
			(0.09)				
	$R^{\rm o}$	00 11 12.89 +35 38 0.9	23.3				
			(0.11)				
	$I^{\rm o}$	00 11 12.90 +35 37 59.9	18.1				
			(0.16)				
	$K^{\rm o}$	00 11 12.97 +35 38 0.2	18.1				
			(0.12)				
	K-UFTI	00 11 12.90 +35 38 0.1	18.4	18.3	18.3	18.5	18.6
	27Jul2000		(0.06)	(0.08)	(0.10)	(0.23)	(0.30)
TOOT00_1027	K-UFTI	00 11 17.0 +34 43 33.8	19.5	19.5	19.8	19.6	19.4
	27Jul2000		(0.18)	(0.24)	(0.42)	(0.61)	(0.61)
TOOT00_1195	$B^{\rm o}$	00 11 52.68 +35 42 20.6	25.4				
			(0.24)				
	$V^{\rm o}$	00 11 52.62 +35 42 19.1	25.5				
			(0.58)				
	$R^{\rm o}$	00 11 52.35 +35 42 20.8	23.2				
			(0.10)				
	$I^{\rm o}$	00 11 52.35 +35 42 20.2	22.1				
			(0.07)				
	$K^{\rm o}$	00 11 52.37 +35 42 20.5	18.5				
			(0.32)				
	K-UFTI	00 11 52.40 +35 42 20.0	18.4	18.3	18.3	18.2	18.2
	27Jul2000		(0.06)	(0.08)	(0.11)	(0.17)	(0.20)
	$J03^{*}$		20.1	20.0	19.9	19.9	20.0
			(0.18)	(0.19)	(0.20)	(0.31)	(0.38)
	$J04^{*}$		19.7	19.5	19.4	19.1	19.0
			(0.12)	(0.12)	(0.12)	(0.13)	(0.14)
	H^{*}		19.1	18.9	18.7	18.4	18.3
			(0.10)	(0.10)	(0.11)	(0.14)	(0.15)
	K^{*}		18.2	18.1	18.0	17.9	17.9
			(0.08)	(0.08)	(0.08)	(0.11)	(0.12)

Table A2. (continued)

(1)	(2)	(3)	(4)	(5)	(6)	(7)	(8)
Object	Band	near-IR Position (J2000)	$3''$mag ($3''$ error)	$4''$mag ($4''$ error)	$5''$mag ($5''$ error)	$8''$mag ($8''$ error)	$9''$mag ($9''$ error)
TOOT00_1069	$B^{\rm o}$	00 12 12.91 +34 58 30.4	26.2 (0.76)				
	$V^{\rm o}$	00 12 13.11 +34 58 32.9	24.9 (0.30)				
	$R^{\rm o}$	00 12 12.92 +34 58 29.8	24.4 (0.24)				
	$I^{\rm o}$	00 12 11.95 +34 58 31.9	22.5 (0.30)				
	$K^{\rm o}$	00 12 13.83 +34 58 31.6	18.7 (0.41)				
	K-UIST 26Jan2003	00 12 12.58 +34 58 30.9		> 20.3			
	K-UFTI 15Sep2004	00 12 12.58 + 34 58 30.9		> 19.2 (object at edge of image - unreliable value)			
TOOT00_1094	$B^{\rm o}$	00 12 16.60 +35 04 25.8	25.8 (0.53)				
	$V^{\rm o}$	00 12 16.56 +35 04 25.6	25.4 (0.47)				
	$R^{\rm o}$	00 12 16.53 +35 04 23.3	24.9 (0.62)				
	$I^{\rm o}$	00 12 16.42 +35 04 22.5	22.3 (0.26)				
	K-UIST 26Jan2003	00 12 16.3 +35 04 23.4		> 20.6			
	K-UFTI 15Sep2004	00 12 16.3 +35 04 23.4	18.6 (0.13)	18.2 (0.13)	17.8 (0.11)	17.5 (0.15)	17.6 (0.19)
TOOT00_1149	$B^{\rm o}$	00 12 17.99 +35 27 29.4	21.1 (0.01)				
	$V^{\rm o}$	00 12 18.00 +35 27 29.0	19.5 (0.01)				
	$R^{\rm o}$	00 12 18.06 +35 27 29.1	18.6 (0.01)				
	$I^{\rm o}$	00 12 17.98 +35 27 29.2	18.1 (0.01)				
	$K^{\rm o}$	00 12 18.01 +35 27 29.1	14.6 (0.01)				
TOOT00_1298	K-UFTI 27Jul2000	00 12 24.20 +35 33 10.5	17.3 (0.03)	17.3 (0.04)	17.2 (0.04)	17.2 (0.08)	17.1 (0.09)
TOOT00_1200	$U^{\rm o}$	00 12 31.19 +35 43 33.0	22.4 (0.03)				
	$B^{\rm o}$	00 12 31.21 +35 43 33.2	22.7 (0.02)				
	$V^{\rm o}$	00 12 31.25 +35 43 33.3	22.0 (0.02)				
	$R^{\rm o}$	00 12 31.22 +35 43 33.6	21.3 (0.02)				
	$I^{\rm o}$	00 12 31.20 +35 43 33.0	20.4 (0.01)				
	K-UFTI 27Jul2000	00 12 31.3 +35 43 33.2	17.5 (0.03)	17.4 (0.04)	17.4 (0.05)	17.4 (0.08)	17.4 (0.10)
TOOT00_1215	$U^{\rm o}$	00 12 45.95 +35 52 19.2	21.8 (0.03)				
	$V^{\rm o}$	00 12 45.92 +35 52 19.7	19.6 (0.01)				
	$R^{\rm o}$	00 12 45.89 +35 52 19.4	18.7 (0.01)				
	$I^{\rm o}$	00 12 45.92 +35 52 19.5	18.2 (0.01)				
	$K^{\rm o}$	00 12 45.92 +35 52 19.1	15.0 (0.01)				

Table A2. (continued)

(1)	(2)	(3)	(4)	(5)	(6)	(7)	(8)
Object	Band	near-IR Position (J2000)	$3''$mag ($3''$ error)	$4''$mag ($4''$ error)	$5''$mag ($5''$ error)	$8''$mag ($8''$ error)	$9''$mag ($9''$ error)
TOOT00_1240	K-UIST 26Jan2003	00 13 05.30 +36 01 51.0	18.8 (0.25)	18.9 (0.35)	18.6 (0.34)	[15.6] (0.04)	[15.6] (0.04)
TOOT00_1289	K-UFTI 14Sep2004	00 13 12.2 +36 27 16.1	18.1 (0.05)	17.8 (0.05)	17.8 (0.06)	17.8 (0.11)	17.7 (0.11)
TOOT00_1072	B^{o}	00 13 13.35 +34 59 41.6	23.4 (0.05)				
	V^{o}	00 13 13.28 +34 59 41.0	21.5 (0.01)				
	R^{o}	00 13 13.35 +34 59 41.3	20.3 (0.01)				
	I^{o}	00 13 13.25 +34 59 41.3	19.1 (0.01)				
	K^{o}	00 13 13.35 +34 59 40.9	15.7 (0.04)				
	K-UFTI 14Jan2001	00 13 13.3 +34 59 40.8	15.9 (0.02)	15.7 (0.02)	15.6 (0.02)	15.4 (0.03)	15.3 (0.04)
TOOT00_1134	B^{o}	00 13 21.21 +35 20 08.2	21.3 (0.01)				
	V^{o}	00 13 21.17 +35 20 07.6	19.7 (0.01)				
	R^{o}	00 13 21.09 +35 20 10.5	18.9 (0.01)				
	I^{o}	00 13 21.00 +35 20 10.2	18.3 (0.01)				
	K^{o}	00 13 21.15 +35 20 08.6	14.2 (0.01)				
	K-UFTI 25Jul2000	00 13 21.2 +35 20 07.6	14.9 (0.01)	14.6 (0.01)	[14.4] (0.01)	[13.9] (0.01)	[13.8] (0.01)
TOOT00_1244	U^{o}	00 13 30.11 +36 03 49.7	20.2 (0.01)				
	V^{o}	00 13 30.07 +36 03 50.3	20.7 (0.01)				
	R^{o}	00 13 30.05 +36 03 50.0	20.3 (0.01)				
	I^{o}	00 13 30.06 +36 03 50.2	20.1 (0.02)				
	K^{o}	00 13 30.11 +36 03 51.0	18.8 (0.46)				
TOOT00_1066	B^{o}	00 13 48.34 +34 56 57.9	25.3 (0.29)				
	V^{o}	00 13 48.31 +34 56 58.1	26.0 (0.83)				
	R^{o}	00 13 48.36 +34 56 58.3	23.3 (0.09)				

Table A2. (continued)

(1) Object	(2) Band	(3) near-IR Position (J2000)	(4) $3''$mag ($3''$ error)	(5) $4''$mag ($4''$ error)	(6) $5''$mag ($5''$ error)	(7) $8''$mag ($8''$ error)	(8) $9''$mag ($9''$ error)
TOOT00_1066	I^{o}	00 13 48.27 +34 56 58.3	21.9 (0.18)				
	K^{o}	00 13 48.23 +34 56 57.8	18.9 (0.36)				
	K-UIST 26Jan2003	00 13 48.3 +34 56 57.6	17.9 (0.06)	17.7 (0.07)	17.7 (0.09)	18.2 (0.23)	18.5 (0.36)
	$J03^{*}$		19.9 (0.14)	19.8 (0.15)	19.7 (0.14)	19.3 (0.15)	19.3 (0.17)
	$J04^{*}$		20.0 (0.14)	19.8 (0.13)	19.7 (0.13)	19.3 (0.14)	19.3 (0.15)
	$H03^{*}$		19.0 (0.09)	18.8 (0.09)	18.7 (0.10)	18.5 (0.12)	18.4 (0.13)
	$H04^{*}$		19.0 (0.08)	18.7 (0.08)	18.6 (0.08)	18.3 (0.08)	18.3 (0.09)
	K^{*}		18.1 (0.07)	18.0 (0.07)	17.9 (0.07)	17.7 (0.07)	17.6 (0.07)
TOOT00_1261	U^{o}	00 14 6.64 +36 08 26.9	22.3 (0.04)				
	V^{o}	00 14 6.60 +36 08 26.9	22.7 (0.05)				
	R^{o}	00 14 6.59 +36 08 26.5	23.0 (0.11)				
	I^{o}	00 14 6.60 +36 08 26.8	22.1 (0.09)				
	K-UFTI 13Jan2002	00 14 6.6 +36 08 27.3	19.3 (0.05)	19.0 (0.06)	19.0 (0.07)	18.9 (0.12)	18.8 (0.13)
TOOT00_1252	K-UFTI 14Sep2004	00 14 30.6 +36 06 44.4		> 19.6			
TOOT00_1214	U^{o}	00 14 43.51 +35 52 05.0	23.0 (0.06)				
	B^{o}	00 14 43.53 +35 52 05.4	24.5 (0.15)				
	V^{o}	00 14 43.54 +35 52 05.4	23.3 (0.07)				
	R^{o}	00 14 43.53 +35 52 05.7	22.9 (0.08)				
	I^{o}	00 14 43.53 +35 52 05.9	22.1 (0.09)				
	K-UFTI 08Jan2002	00 14 43.6 +35 52 05.4	18.6 (0.03)	[18.3] (0.03)	[18.1] (0.03)	[17.9] (0.05)	[17.9] (0.06)
TOOT00_1152	U^{o}	00 14 49.09 +35 28 7.4	25.3 (0.97)				
	B^{o}	00 14 49.88 +35 28 11.6	25.7 (0.43)				
	V^{o}	00 14 49.10 +35 28 7.2	26.3 (1.16)				
	R^{o}	00 14 49.10 +35 28 7.4	25.0 (0.40)				
	I^{o}	00 14 49.49 +35 28 9.2	24.2 (1.51)				
	K^{o}	00 14 49.08 +35 28 7.2	21.1 (3.19)				
	K-UIST 26Jan2003	00 14 49.7 +35 28 11.1	19.6 (0.6)	19.6 (0.8)	21.2 (4.3)		

Table A2. (continued)

(1) Object	(2) Band	(3) near-IR Position (J2000)	(4) 3″mag (3″ error)	(5) 4″mag (4″ error)	(6) 5″mag (5″ error)	(7) 8″mag (8″ error)	(8) 9″mag (9″ error)
TOOT00_1129	U^{o}	00 15 4.32 +35 19 1.1	22.7 (0.11)				
	B^{o}	00 15 4.33 +35 19 1.1	23.4 (0.07)				
	V^{o}	00 15 4.33 +35 19 1.1	23.0 (0.06)				
	R^{o}	00 15 4.37 +35 19 1.4	22.7 (0.04)				
	I^{o}	00 15 4.34 +35 19 1.4	22.7 (0.13)				
	K^{o}	00 15 4.30 +35 19 0.9	18.5 (0.50)				
	K-UIST 27Jan2003	00 15 4.3 +35 18 56.7	20.2 (0.85)	20.2 (1.13)	21.9 (7.10)		
TOOT00_1090	R^{o}	00 15 16.00 +35 03 28.0	17.9 (0.01)				
	I^{o}	00 15 15.91 +35 03 27.9	17.4 (0.01)				
	K-UFTI 28Dec2000	00 15 15.9 +35 03 27.7	14.7 (0.01)	14.6 (0.01)	14.4 (0.01)	14.2 (0.01)	14.2 (0.01)
TOOT00_1267	K-UIST 27Jan2003	00 15 31.0 +36 12 16.5	17.6 (0.08)	17.5 (0.09)	17.5 (0.11)	17.5 (0.21)	17.7 (0.29)
	$J03^{*}$		19.3 (0.12)	19.2 (0.12)	19.0 (0.11)	19.1 (0.15)	19.1 (0.18)
	$J04^{*}$		19.1 (0.09)	19.0 (0.09)	18.9 (0.09)	18.8 (0.12)	18.9 (0.13)
	H^{*}		18.3 (0.07)	18.2 (0.06)	18.1 (0.07)	18.1 (0.09)	18.0 (0.10)
	K^{*}		17.3 (0.05)	17.1 (0.05)	17.1 (0.05)	16.9 (0.05)	16.9 (0.05)
TOOT00_1188	U^{o}	00 15 56.37 +35 39 49.8	26.3 (1.37)				
	B^{o}	00 15 56.33 +35 39 51.8	23.5 (0.06)				
	V^{o}	00 15 56.34 +35 39 52.4	23.2 (0.08)				
	R^{o}	00 15 56.39 +35 39 52.2	22.5 (0.05)				
	I^{o}	00 15 56.32 +35 39 52.2	21.9 (0.08)				
	K^{o}	00 15 56.36 +35 39 51.8	18.0 (0.19)				
	K-UIST 27Jan2003	00 15 56.33 +35 39 52.1	18.1 (0.12)	18.3 (0.20)	18.9 (0.42)		
TOOT00_1196	R^{o}	00 16 36.76 +35 42 23.1	24.1 (0.2)				
	I^{o}	00 16 36.76 +35 41 23.1	22.4 (0.12)				
	K-UIST 27Jan2003	00 16 35.74 +35 42 22.9	18.5 (0.09)	18.4 (0.11)	18.3 (0.13)	18.9 (0.37)	19.3 (0.65)
	K-UFTI 15Sep2004	00 16 35.71 +35 42 22.8	17.4 (0.04)	17.4 (0.06)	17.3 (0.07)	17.1 (0.10)	16.9 (0.10)

Table A2. (continued)

(1)	(2)	(3)	(4)	(5)	(6)	(7)	(8)
Object	Band	near-IR Position (J2000)	3″mag (3″ error)	4″mag (4″ error)	5″mag (5″ error)	8″mag (8″ error)	9″mag (9″ error)
TOOT00_1173	U^{o}	00 16 59.49 +35 34 36.2	22.6				
			(0.09)				
	B^{o}	00 16 59.54 +35 34 35.6	21.6				
			(0.02)				
	V^{o}	00 16 59.52 +35 34 36.0	20.4				
			(0.01)				
	R^{o}	00 16 59.55 +35 34 36.3	19.4				
			(0.01)				
	I^{o}	00 16 59.53 +35 34 36.3	18.7				
			(0.01)				
	K-UFTI	00 16 59.5 +35 34 35.9	15.6	15.3	15.2	15.1	15.1
	14Jan2001		(0.02)	(0.02)	(0.02)	(0.04)	(0.04)
TOOT00_1228	V^{o}	00 17 2.99 +35 56 19.0	25.4				
			(0.57)				
	K^{o}	00 17 2.79 +35 56 19.9	19.3				
			(1.49)				
	K-UFTI	00 17 3.00 +35 56 18.4	18.5	18.5	18.5	18.3	18.6
	14Jan2001		(0.10)	(0.13)	(0.18)	(0.28)	(0.41)
TOOT00_1034	R^{o}	00 17 4.87 +34 46 57.2	20.4				
			(0.01)				
	I^{o}	00 17 4.79 +34 46 57.1	19.5				
			(0.01)				
	K-UIST	00 17 4.8 +34 46 56.5	16.2	16.1	15.9	15.8	15.8
	27Jan2003		(0.03)	(0.03)	(0.03)	(0.05)	(0.06)
TOOT00_1255	B^{o}	00 17 28.30 +36 7 27.3	24.6				
			(0.18)				
	V^{o}	00 17 28.29 +36 7 27.8	22.6				
			(0.05)				
	R^{o}	00 17 28.23 +36 7 27.7	21.5				
			(0.02)				
	I^{o}	00 17 28.23 +36 7 27.8	20.5				
			(0.02)				
	K-UFTI	00 17 28.2 +36 07 27.2	17.5	17.4	17.3	[16.7]	[16.7]
	08Jan2001		(0.03)	(0.04)	(0.04)	(0.05)	(0.05)
	$J03^*$		18.9	18.7	18.5	18.2	17.8
			(0.10)	(0.09)	(0.09)	(0.09)	(0.07)
	$J04^*$		18.8	18.6	18.5	18.0	17.7
			(0.08)	(0.07)	(0.07)	(0.07)	(0.06)
	H^*		17.8	17.6	17.5	17.1	16.7
			(0.05)	(0.05)	(0.05)	(0.05)	(0.04)
	K^*		17.0	16.8	16.7	16.5	16.3
			(0.05)	(0.05)	(0.05)	(0.05)	(0.05)
TOOT00_1048	K-UIST	00 18 16.5 +34 50 36.2	18.0	17.5	17.4	17.2	17.2
	27Jan2003		(0.19)	(0.16)	(0.18)	(0.27)	(0.33)
TOOT00_1029	K-UFTI	00 18 28.0 +34 44 49.5	16.0	15.9	15.8	15.4	[15.4]
	28Dec2000		(0.02)	(0.02)	(0.02)	(0.03)	(0.03)
	J^*		18.6	18.4	18.3	18.1	18.1
			(0.08)	(0.07)	(0.07)	(0.08)	(0.09)
	H^*		17.7	17.6	17.5	17.4	17.5
			(0.05)	(0.04)	(0.04)	(0.06)	(0.06)
	K_a^*		16.8	16.6	16.5	16.4	16.4
			(0.04)	(0.03)	(0.03)	(0.04)	(0.04)
	K_b^*		16.8	16.6	16.5	16.4	16.4
			(0.04)	(0.04)	(0.04)	(0.04)	(0.04)
TOOT00_1115	K-UFTI	00 18 53.9 +35 10 11.4	16.0	15.9	15.7	15.4	15.4
	28Dec2000		(0.02)	(0.02)	(0.02)	(0.03)	(0.03)
TOOT00_1132	K-UFTI	00 19 20.1 +35 19 36.2	15.1	15.0	14.9	14.8	14.8
	14Jan2001		(0.01)	(0.01)	(0.01)	(0.02)	(0.03)

Table A2. (continued)

(1) Object	(2) Band	(3) near-IR Position (J2000)	(4) $3''$mag ($3''$ error)	(5) $4''$mag ($4''$ error)	(6) $5''$mag ($5''$ error)	(7) $8''$mag ($8''$ error)	(8) $9''$mag ($9''$ error)
TOOT00_1250	$B^{\rm o}$	00 19 54.43 +36 06 21.7	22.9 (0.04)				
	$V^{\rm o}$	00 19 54.40 +36 06 22.2	22.5 (0.04)				
	$R^{\rm o}$	00 19 54.34 +36 06 22.3	21.9 (0.03)				
	$I^{\rm o}$	00 19 54.33 +36 06 22.4	22.4 (0.12)				
	K-UFTI 28Dec2000	00 19 54.4 +36 06 22.2	18.2 (0.13)	18.0 (0.14)	17.8 (0.16)	18.5 (0.50)	18.4 (0.57)
TOOT00_1268	K-UIST 27Jan2003	00 21 52.0 +36 12 18.4	17.6 (0.08)	17.6 (0.11)	17.5 (0.12)	17.5 (0.21)	[17.4] (0.21)
TOOT00_1251	K-UFTI 28Dec2000	00 22 19.0 +36 06 29.6	17.85 (0.32)	19.1 (1.30)			
TOOT00_1203	K-UFTI 14Jan2001	00 23 31.6 +35 45 04.2	17.6 (0.04)	17.4 (0.05)	17.0 (0.05)	[15.7] (0.02)	[15.7] (0.03)
	J^*		19.2 (0.10)	18.9 (0.09)	18.4 (0.07)	16.8 (0.04)	16.8 (0.04)
	H^*		18.5 (0.07)	18.3 (0.07)	17.8 (0.06)	16.3 (0.03)	16.2 (0.03)
	K^*		17.6 (0.06)	17.4 (0.05)	17.1 (0.05)	15.8 (0.03)	15.8 (0.03)

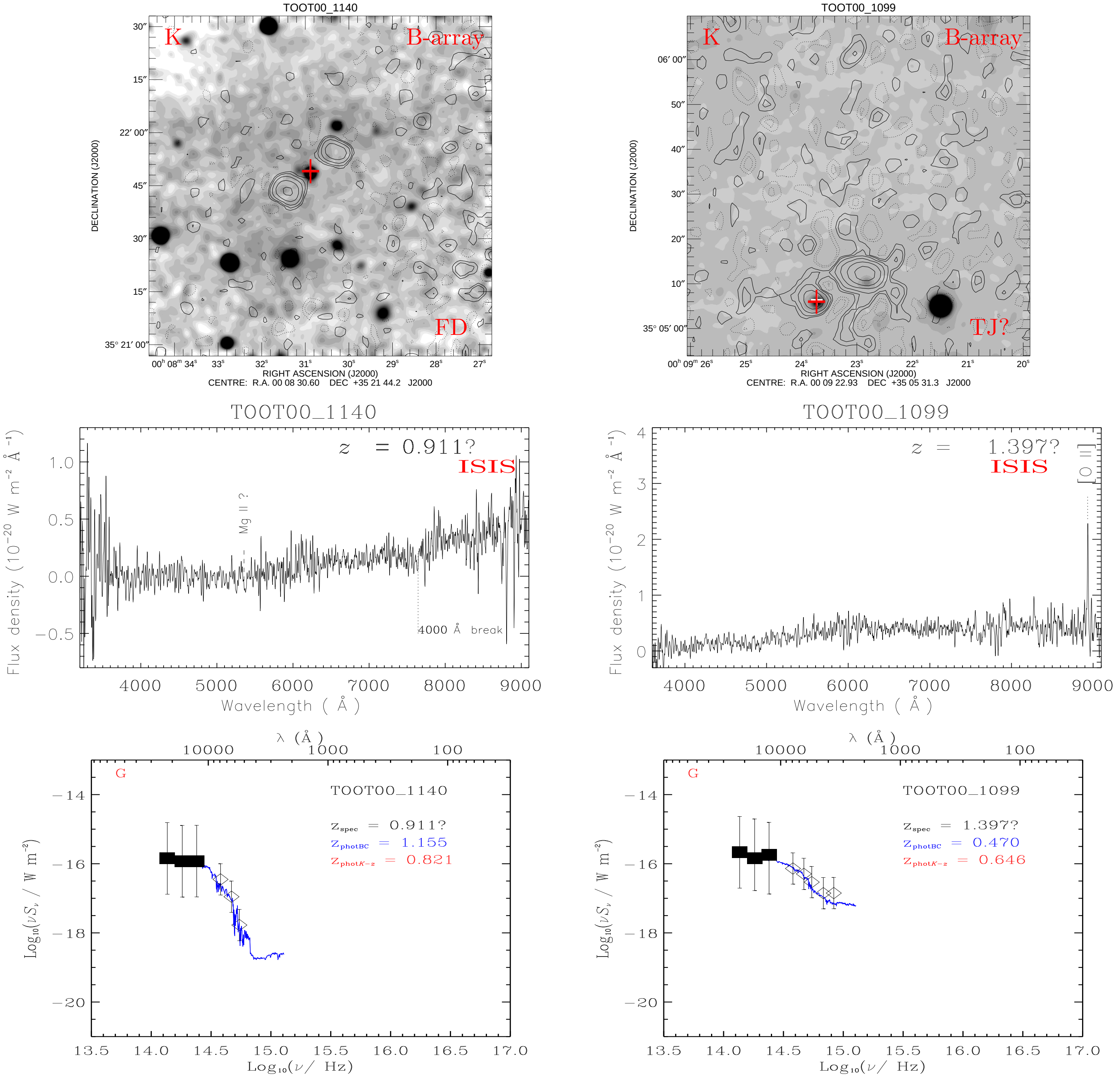

Figure A1. At the **top** of each panel we present the K-band images and overlaid radio contours from the VLA (B- or A-array as stated). The contour levels follow: $2^{n_{\rm contour}-1} \times \sigma$, where $\rm n_{contour}$ is the number of contours and σ the noise level. A white/red cross indicates the position of the assumed near-ID. In the **middle** we give the optical spectrum of the object, as described in Section 2. The blue and red part of each spectrum have been combined at ~ 6000 Å. We haven't corrected for atmospheric absorption, which is labelled as 'A' in the spectrum; 'S' denotes a sky line; 'F' denotes fringing; and 'C' a cosmic ray effect. At the **bottom** we give the SED and the results from the HyperZ fit on the photometric data. Symbols: filled squares denote photometric points, whereas open diamonds denote that the fluxes were estimated from the optical spectra. Note: for object TOOT00_1240 we also provide a zoomed-in $K-$band/radio overlay and a DSS/radio overlay. The positions of an M-star and a galaxy G ($z = 0.191$) close to the position of TOOT00_1240 are marked with an 'M' and a 'G' respectively. For TOOT00_1252 both A- and B-array radio maps are presented; the K position is not marked since it is a limit at K. The red arrow in the K-band/B-array overlay in TOOT00_1196 shows the 7C radio position.

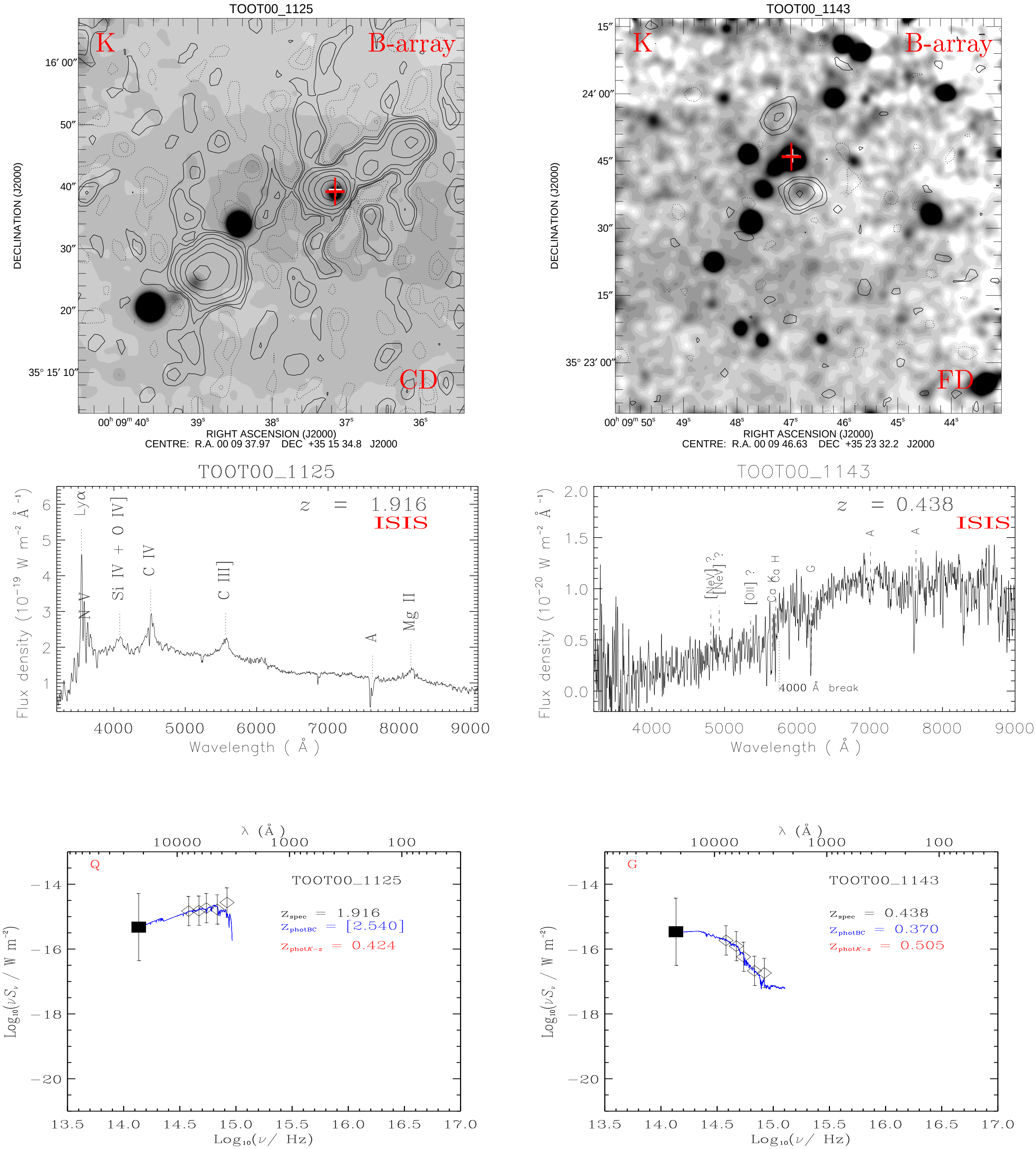

Figure A1. (continued)

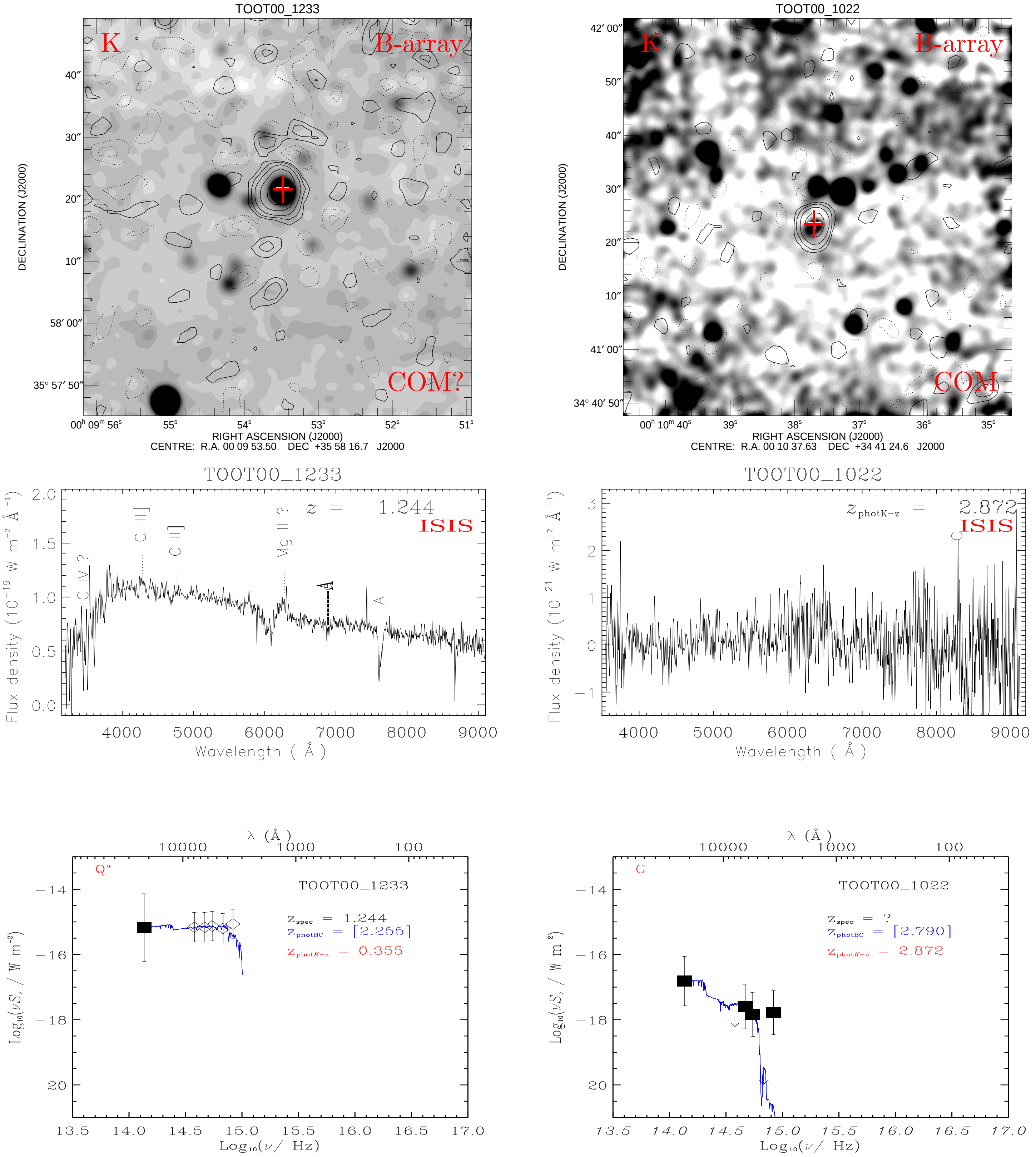

Figure A1. (continued)

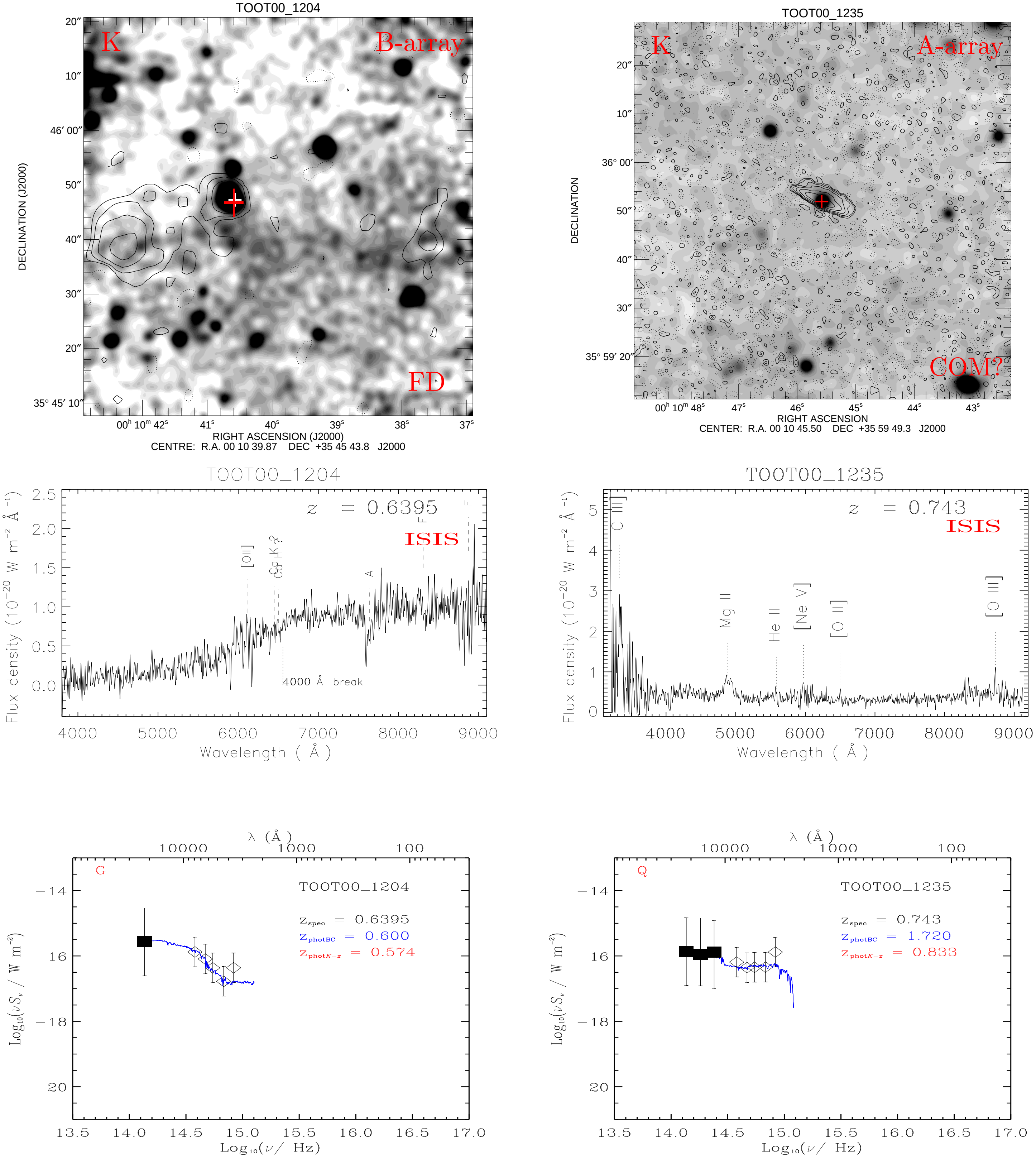

Figure A1. (continued)

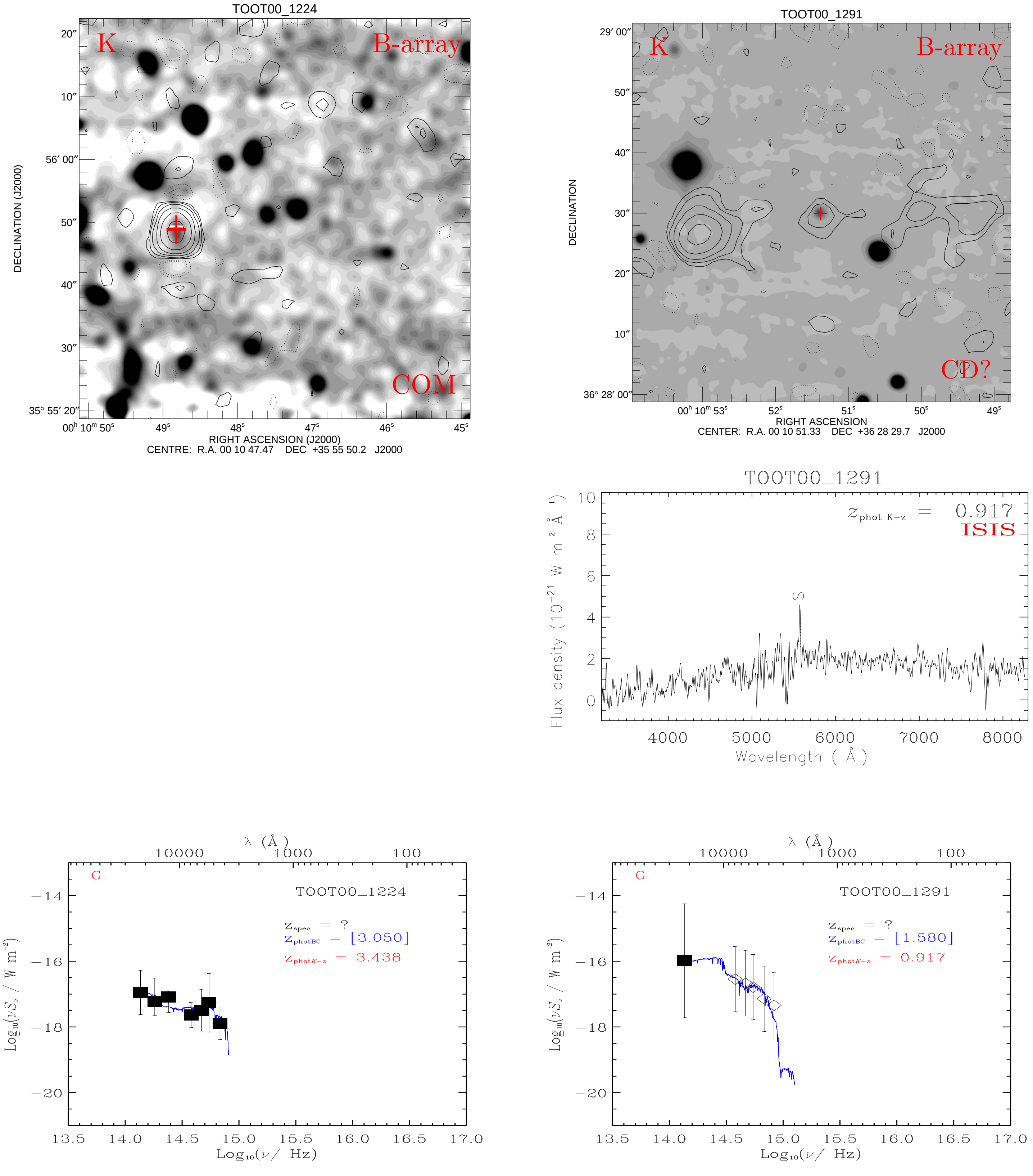

Figure A1. (continued)

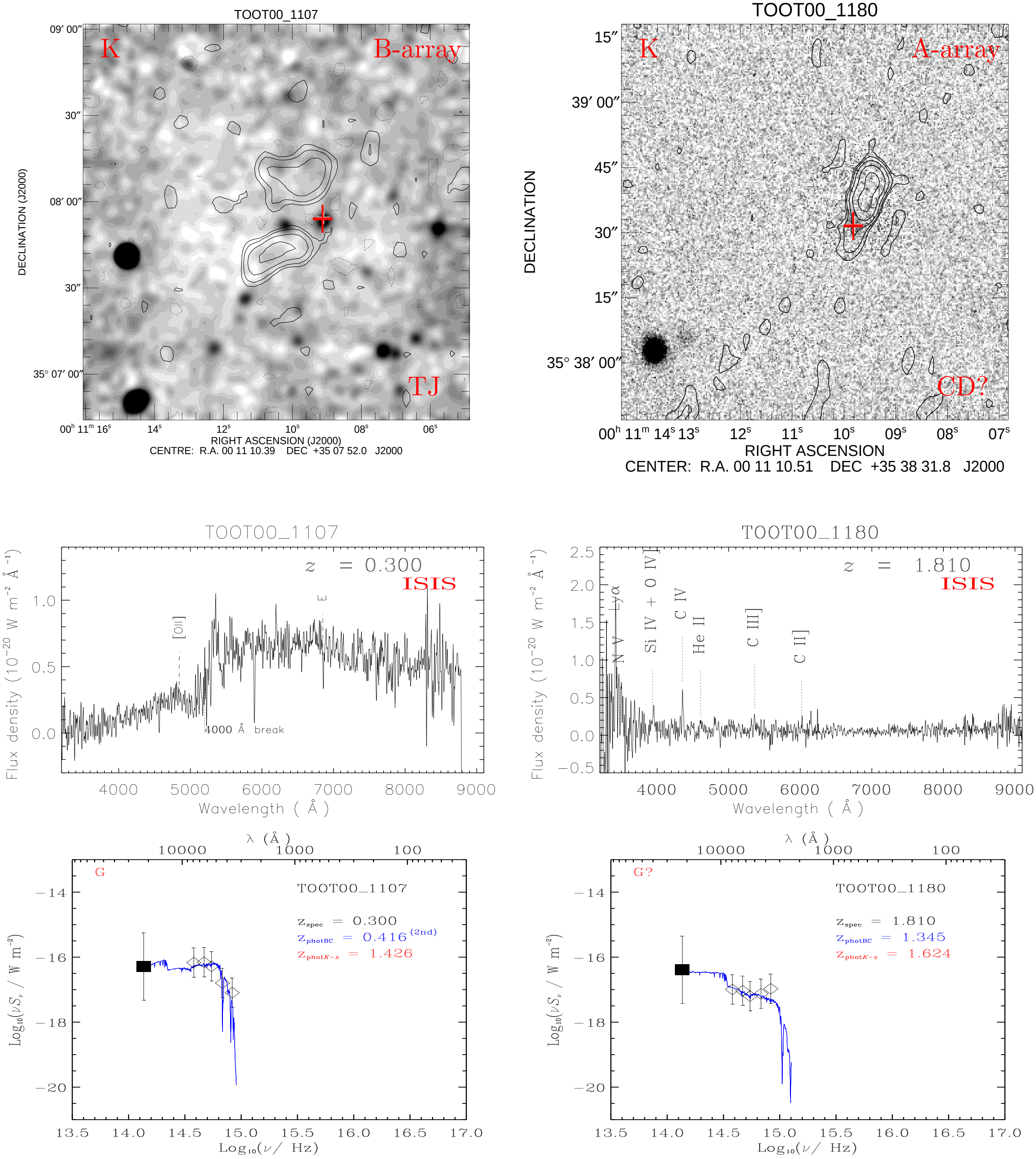

Figure A1. (continued)

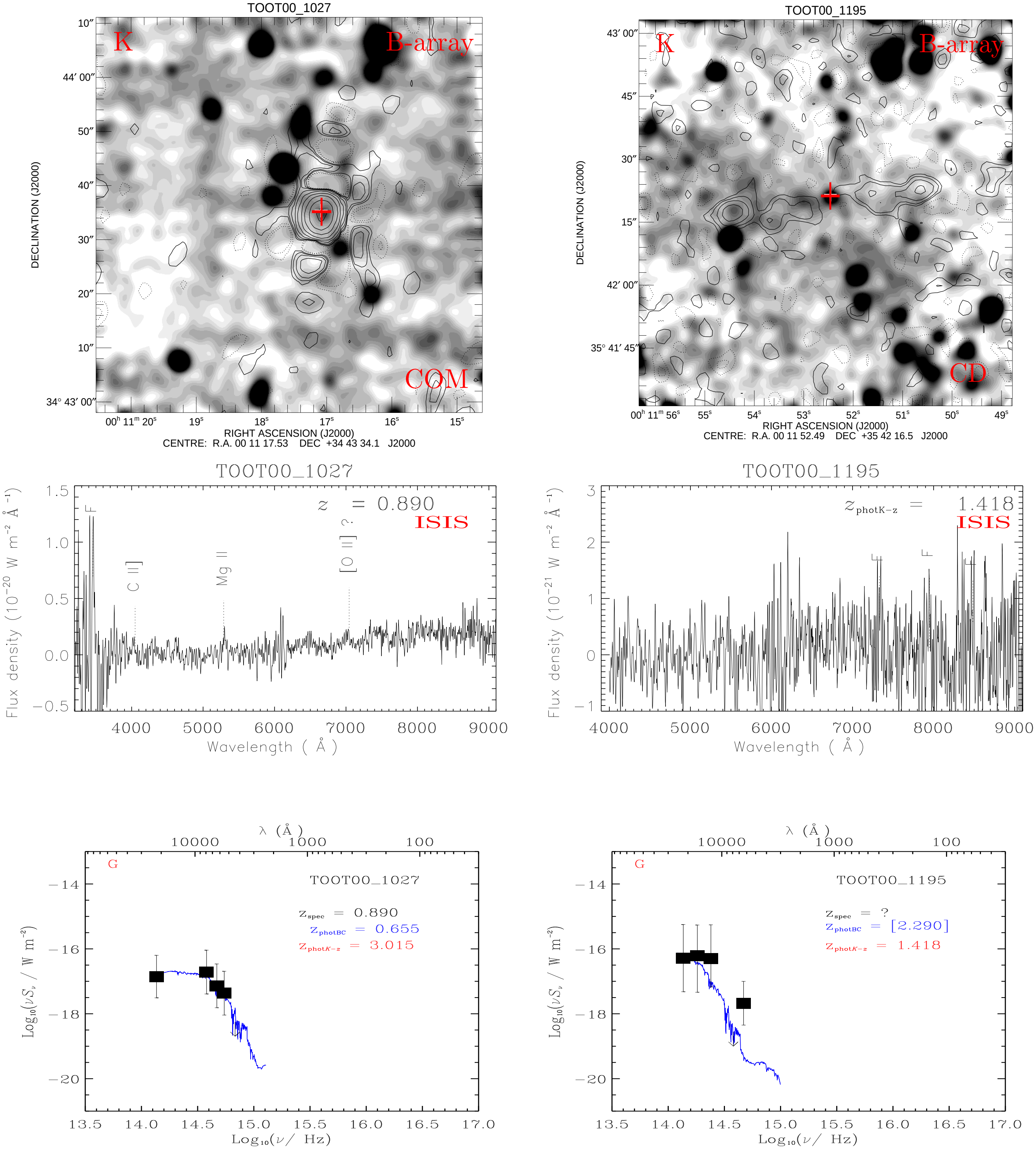

Figure A1. (continued)

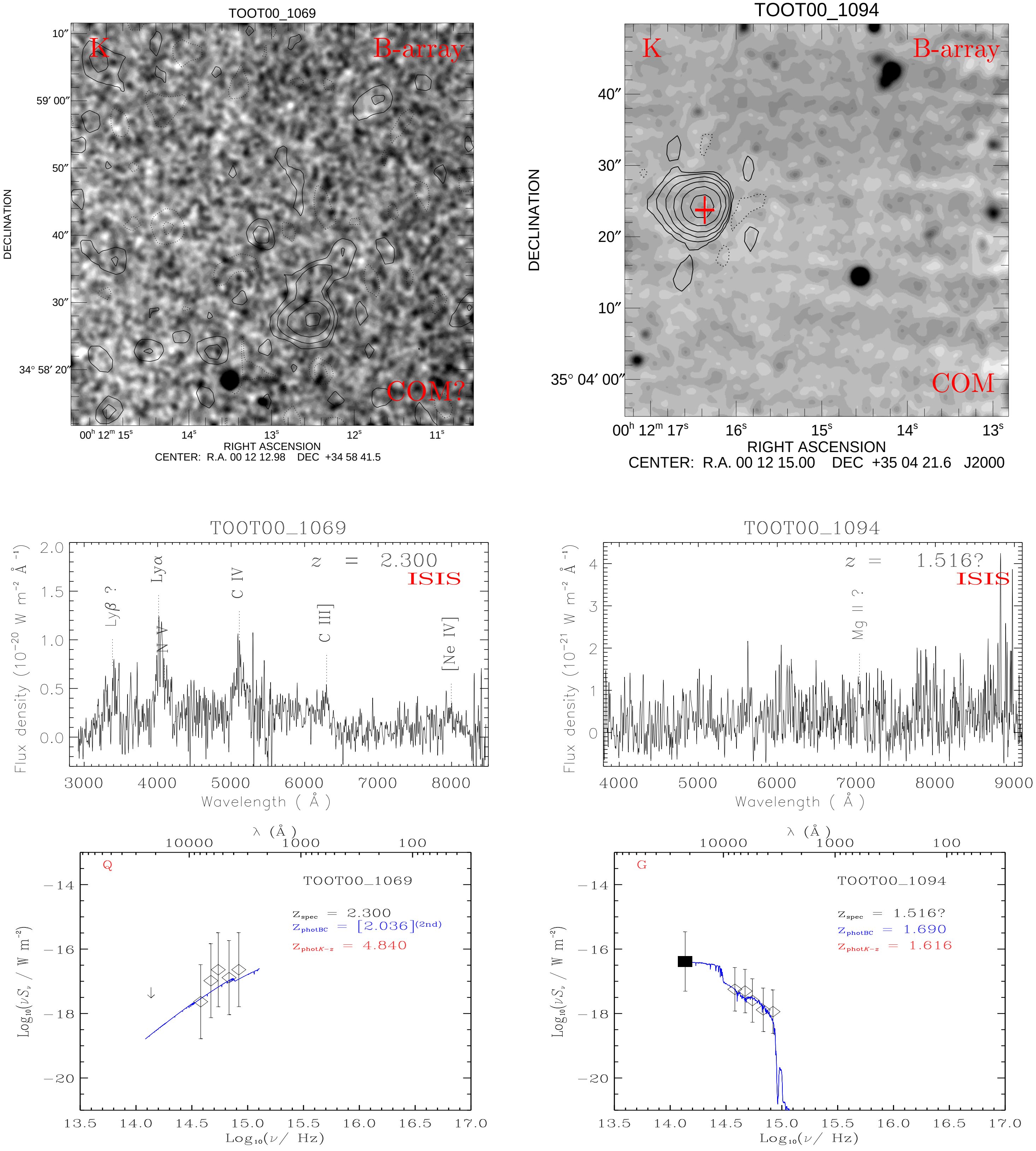

Figure A1. (continued)

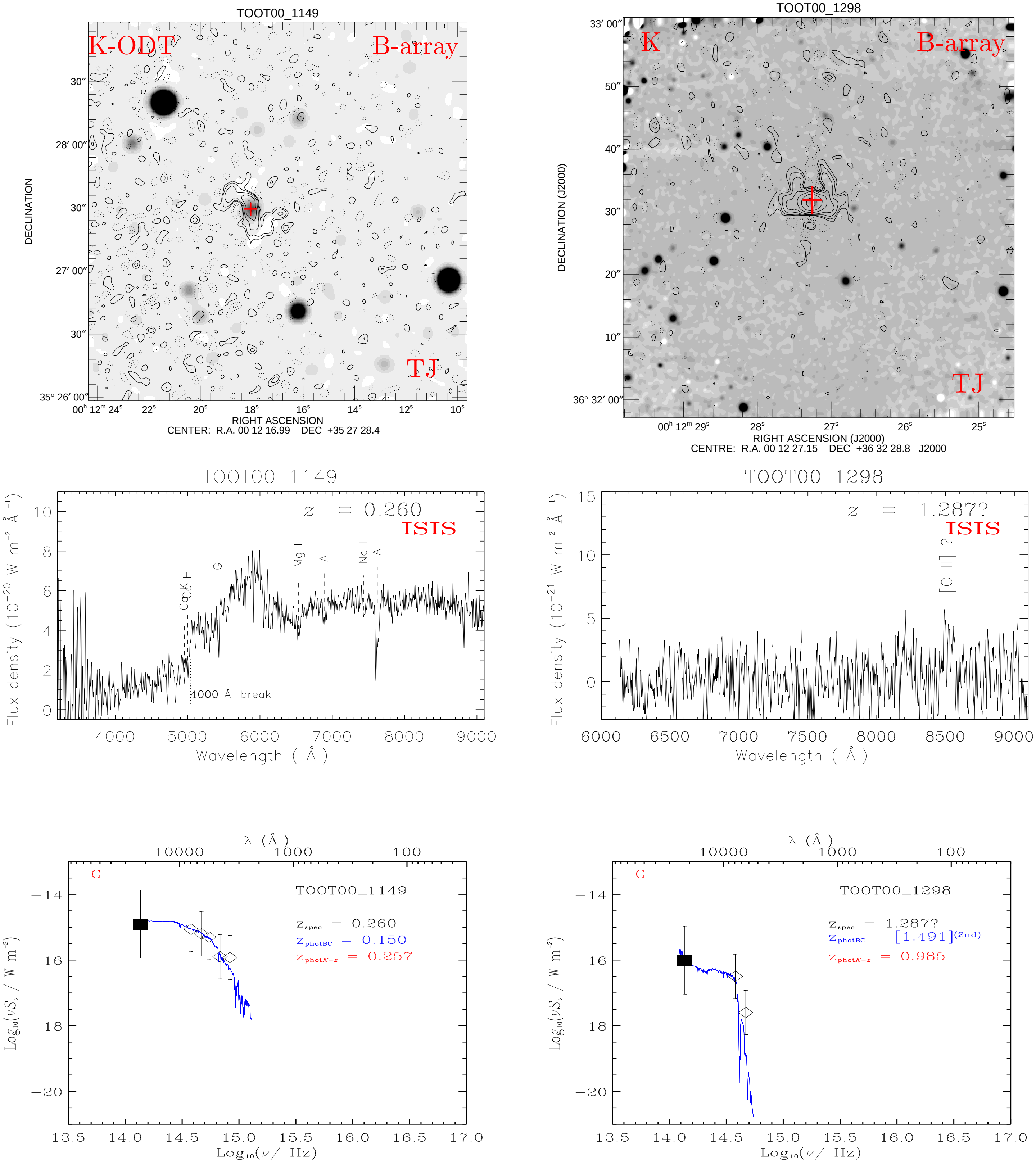

Figure A1. (continued)

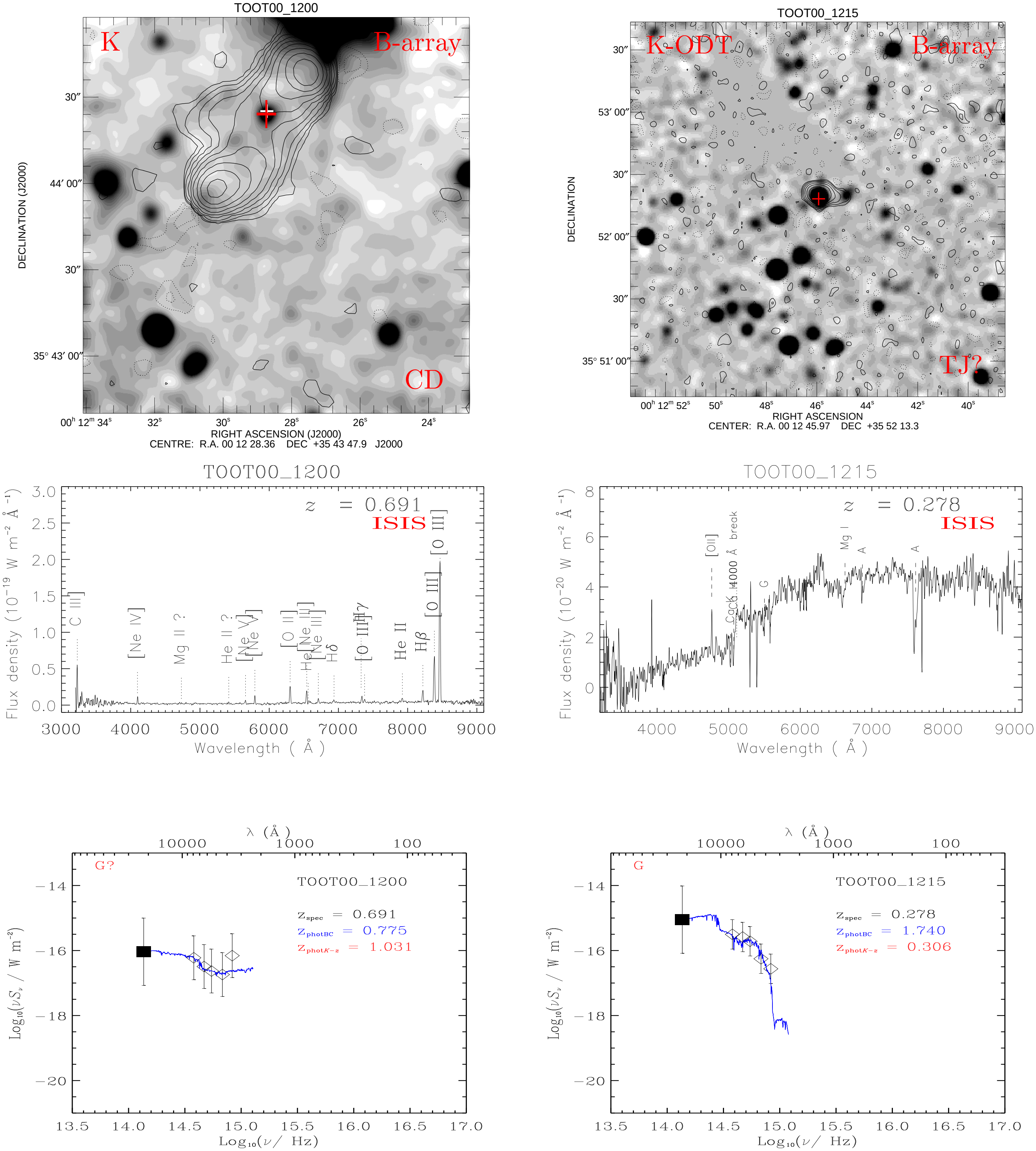

Figure A1. (continued)

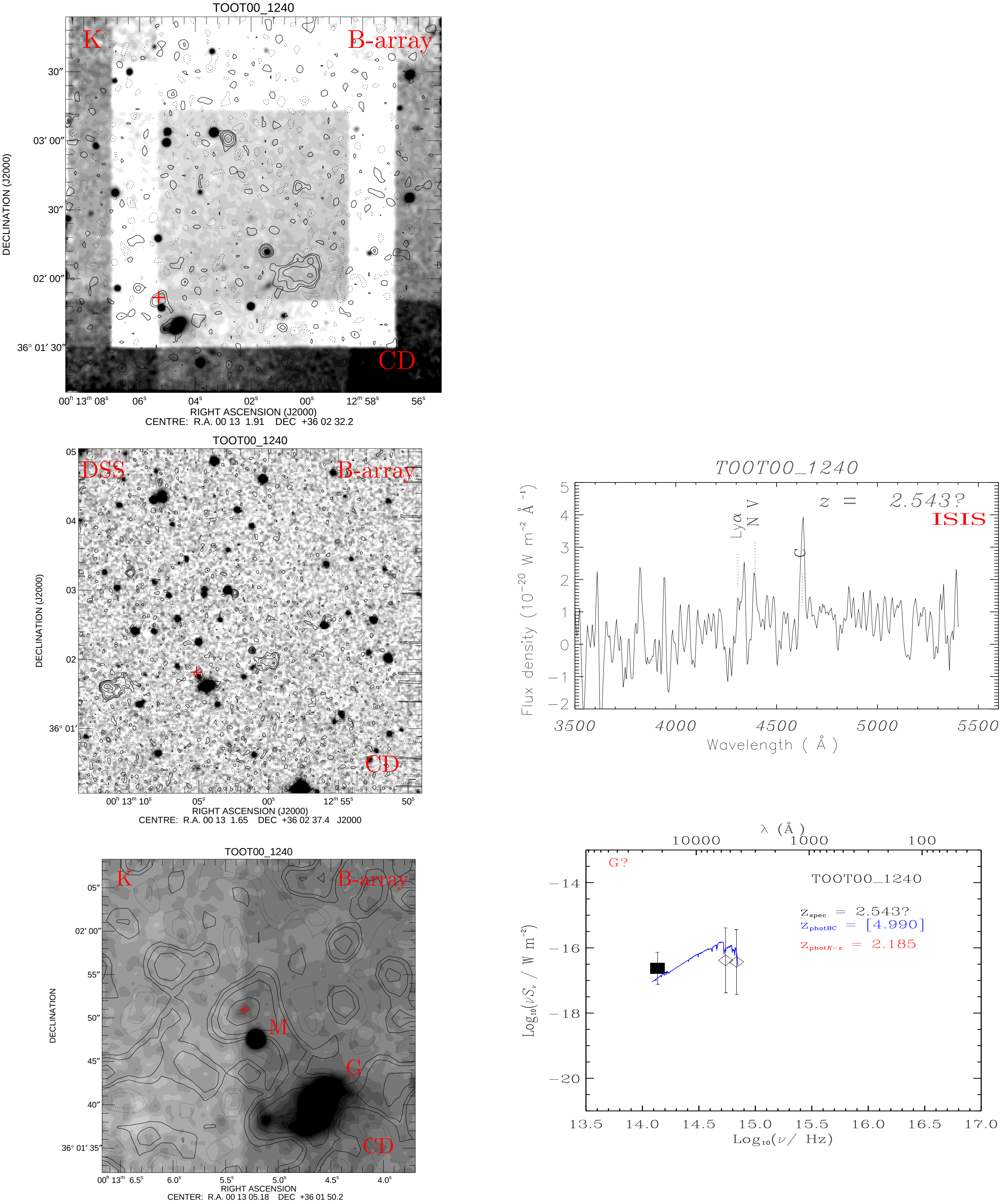

Figure A1. (continued)

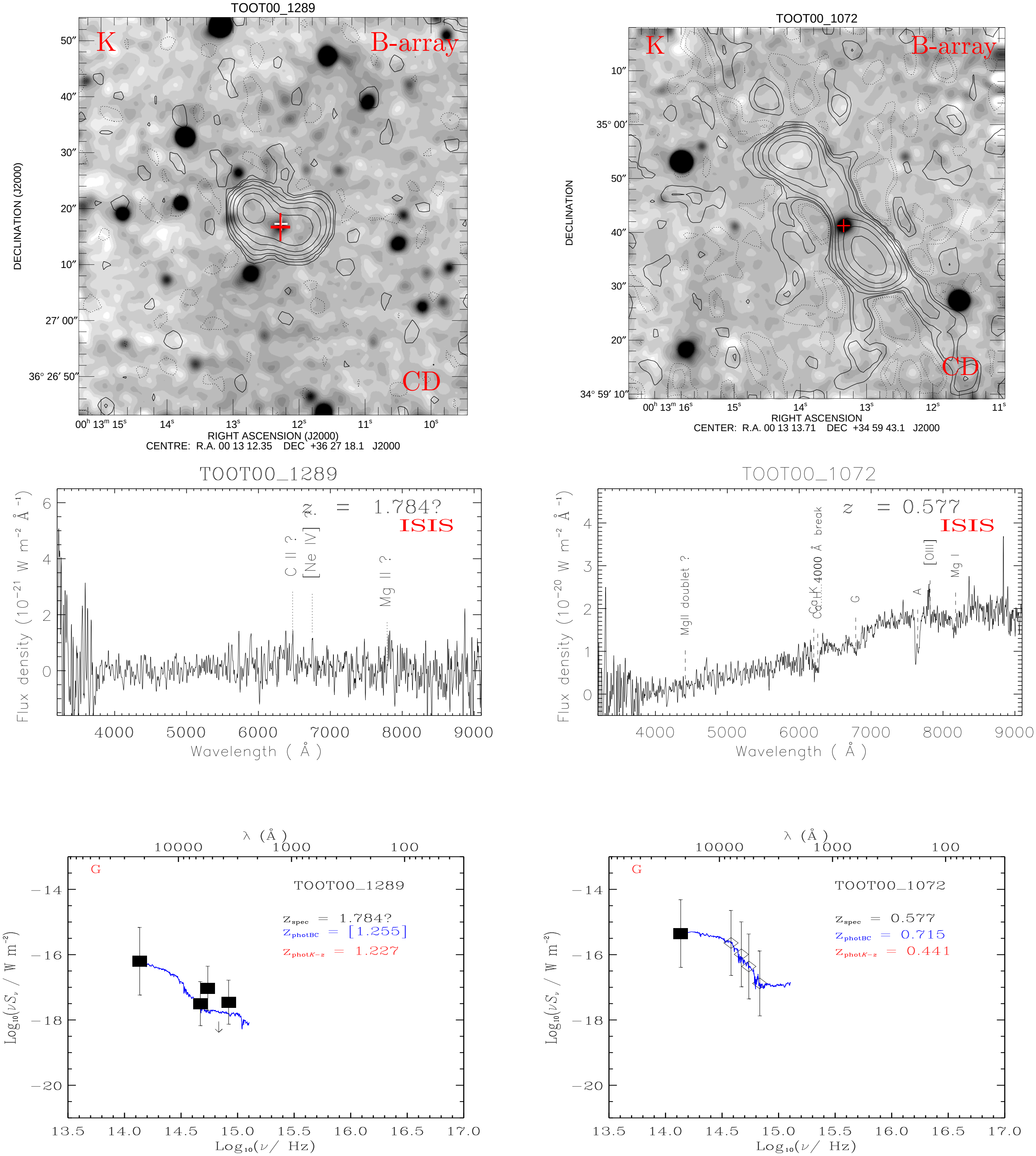

Figure A1. (continued)

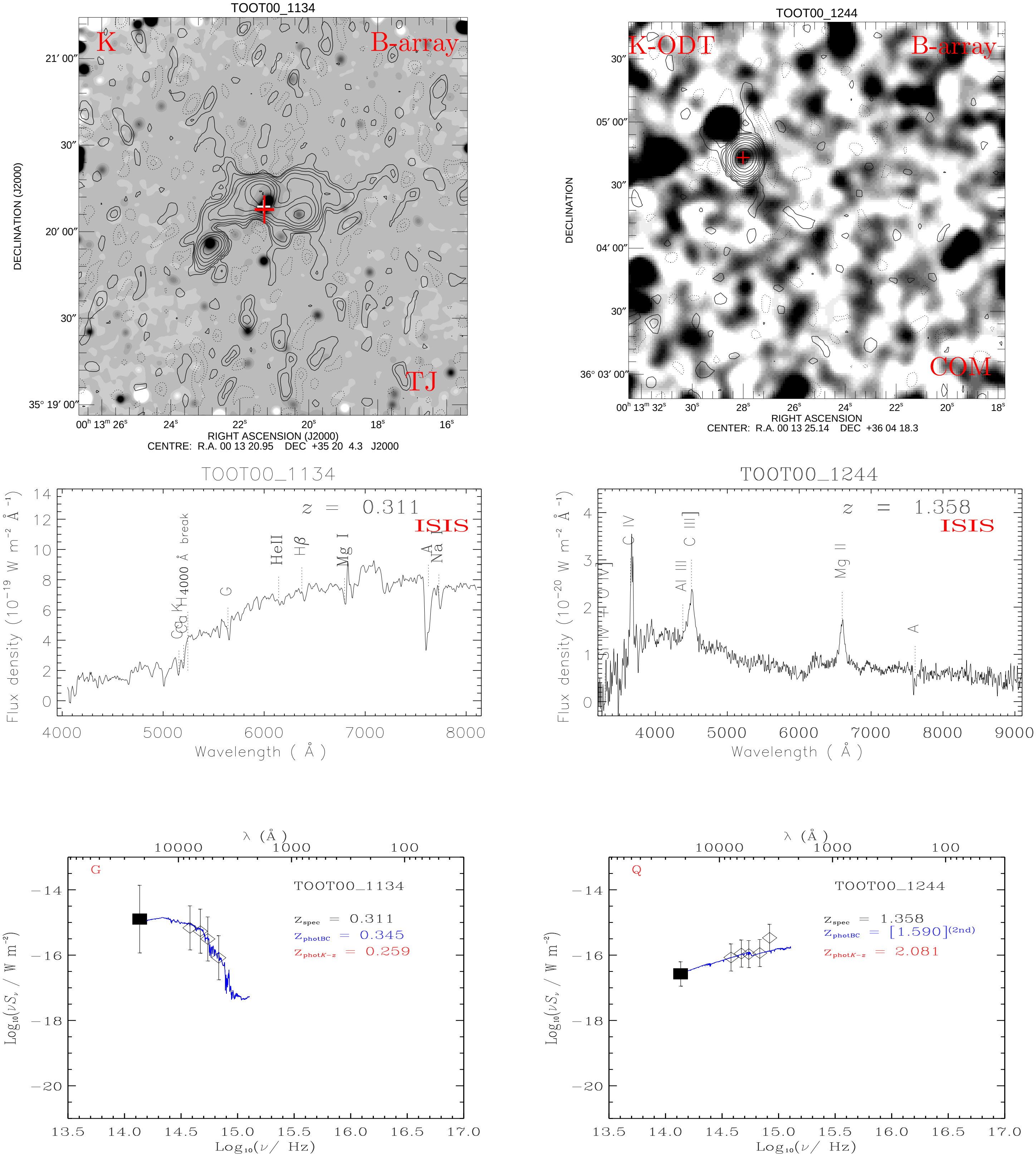

Figure A1. (continued)

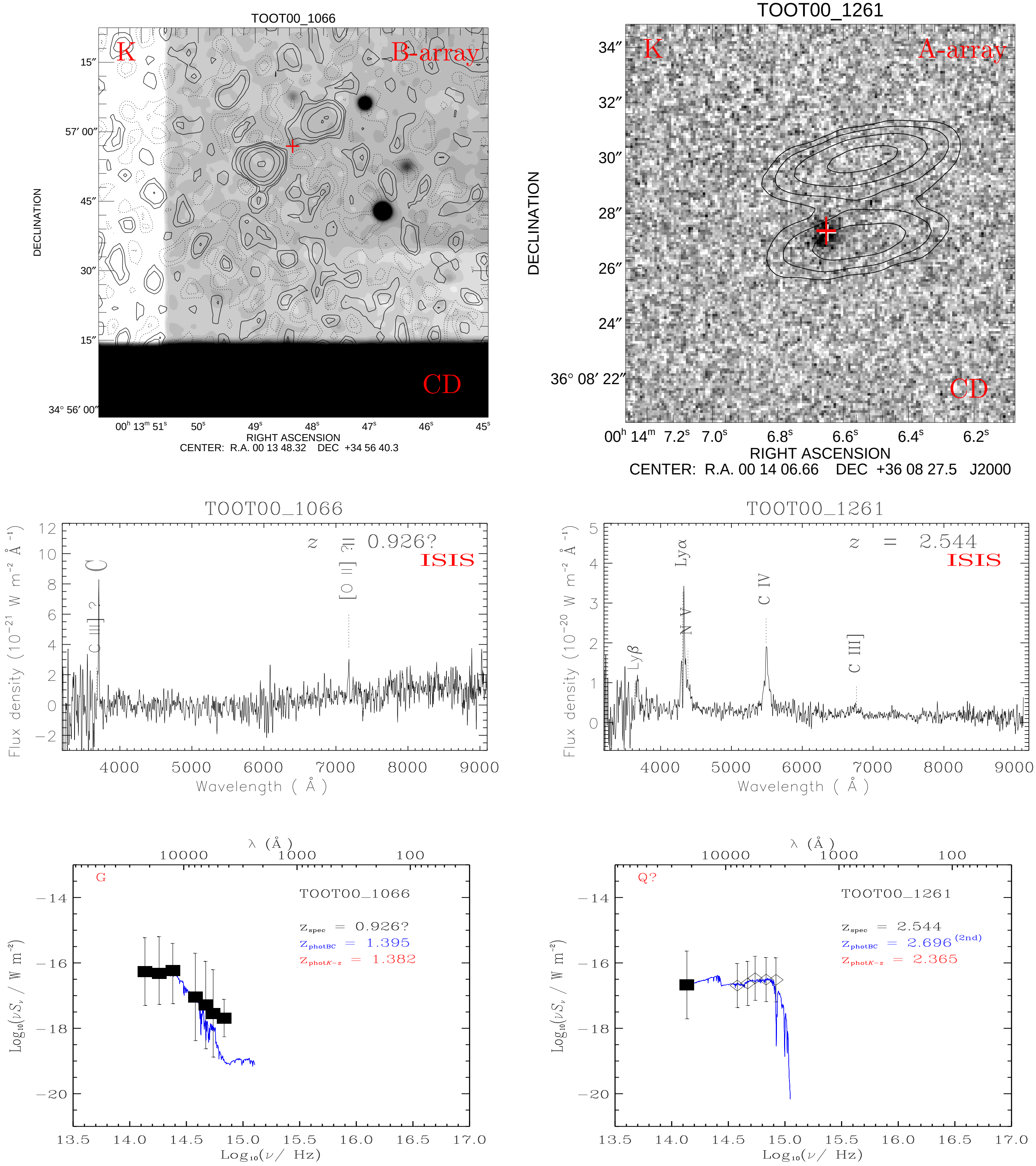

Figure A1. (continued)

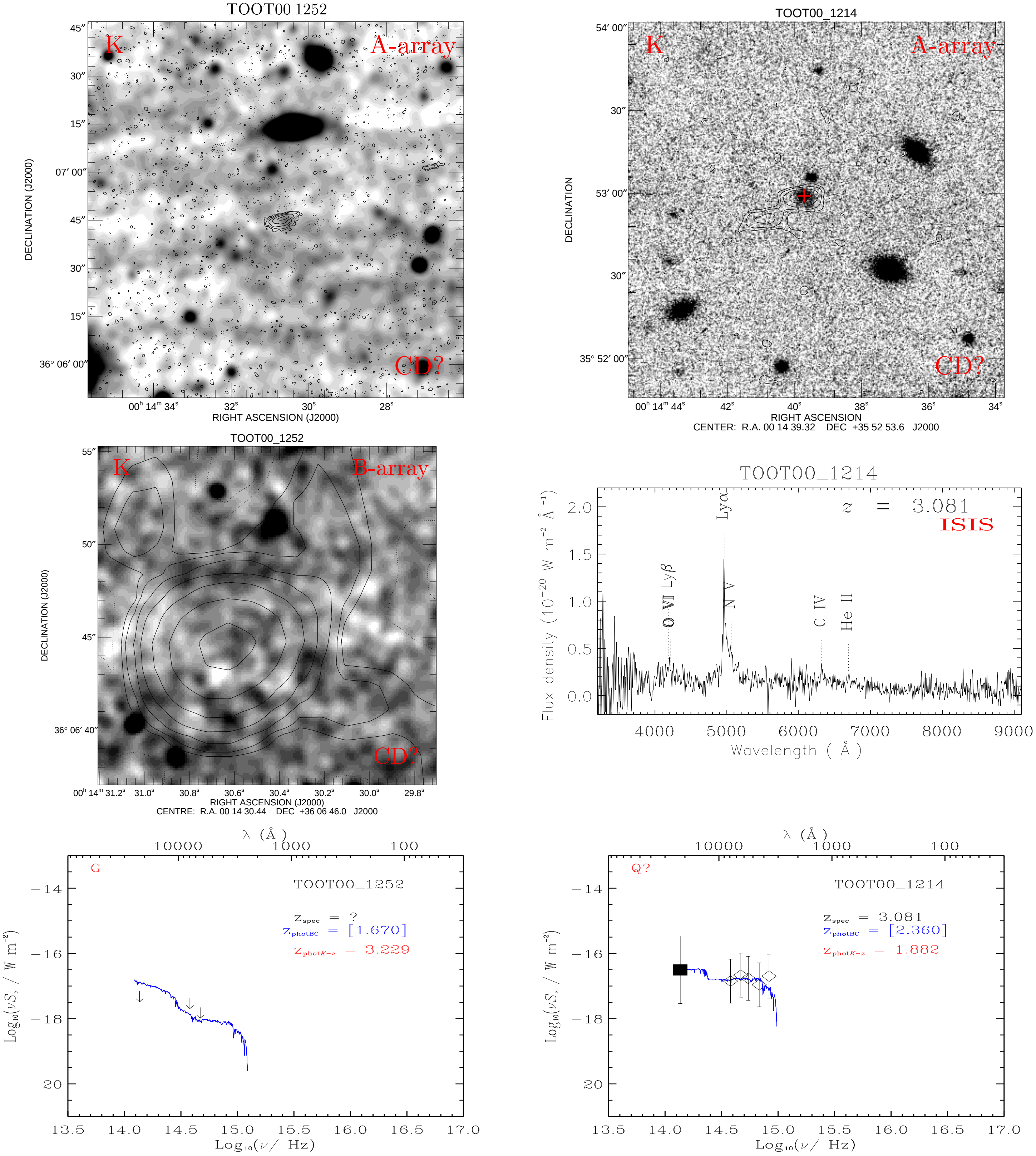

Figure A1. (continued)

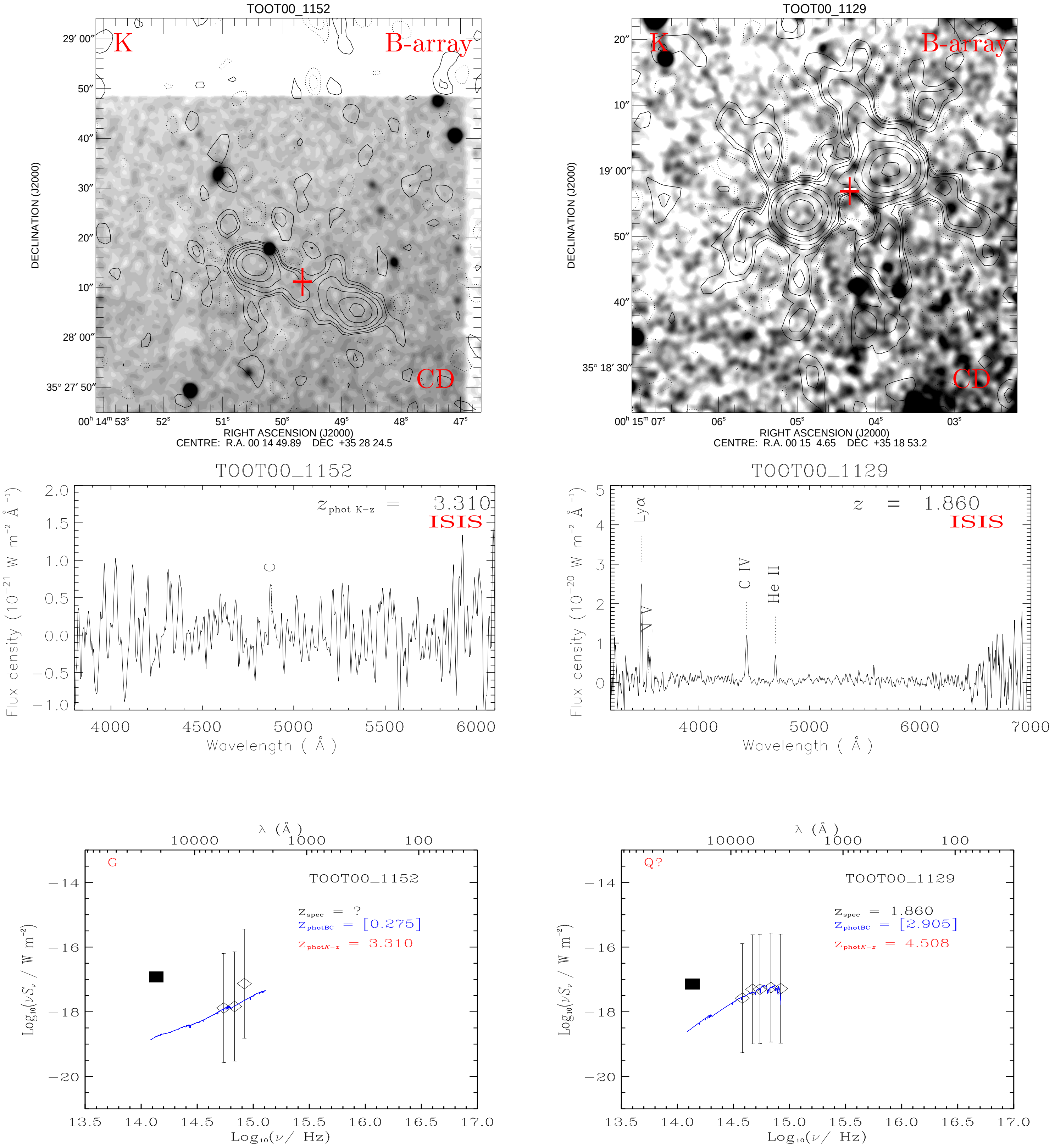

Figure A1. (continued)

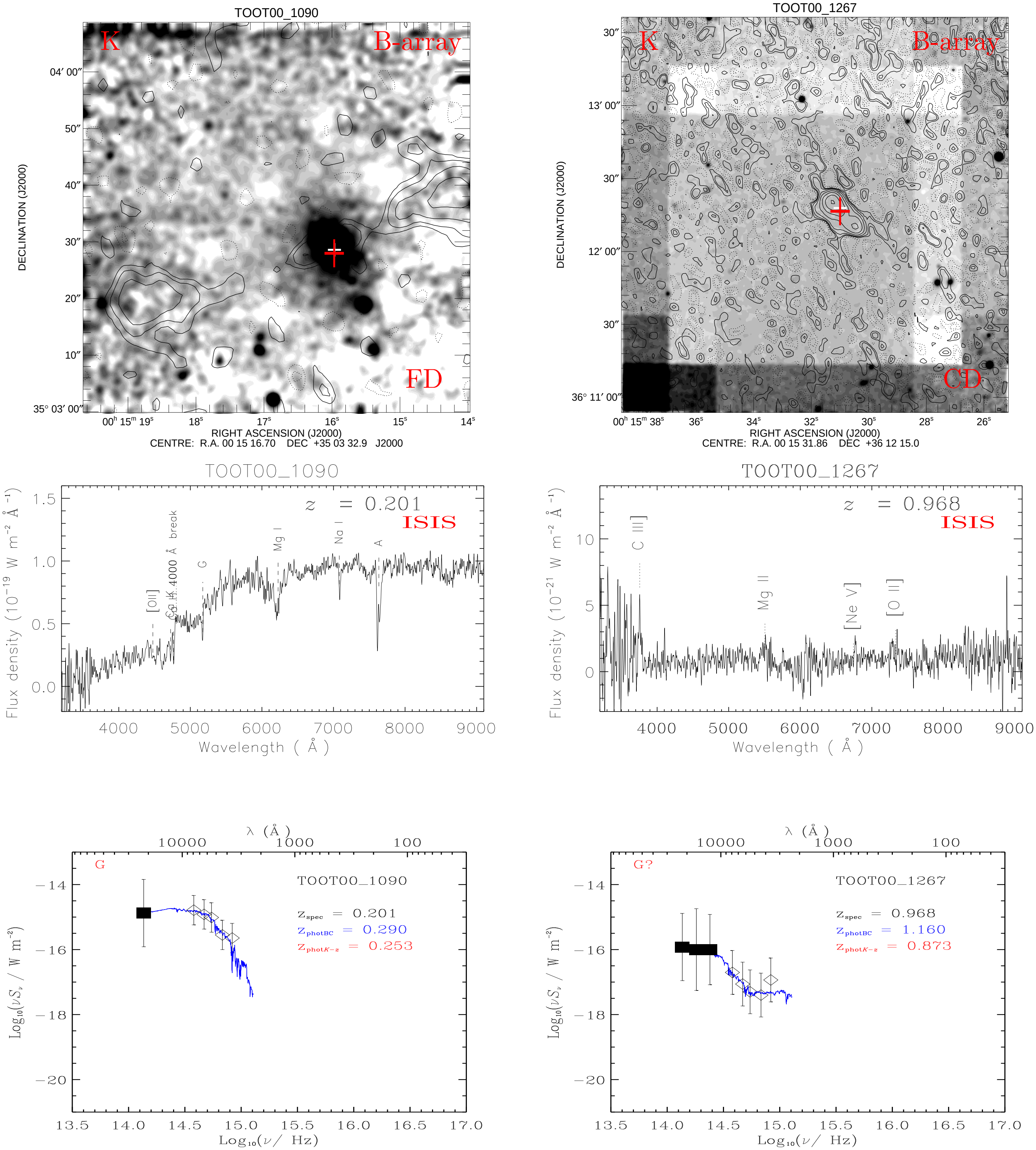

Figure A1. (continued)

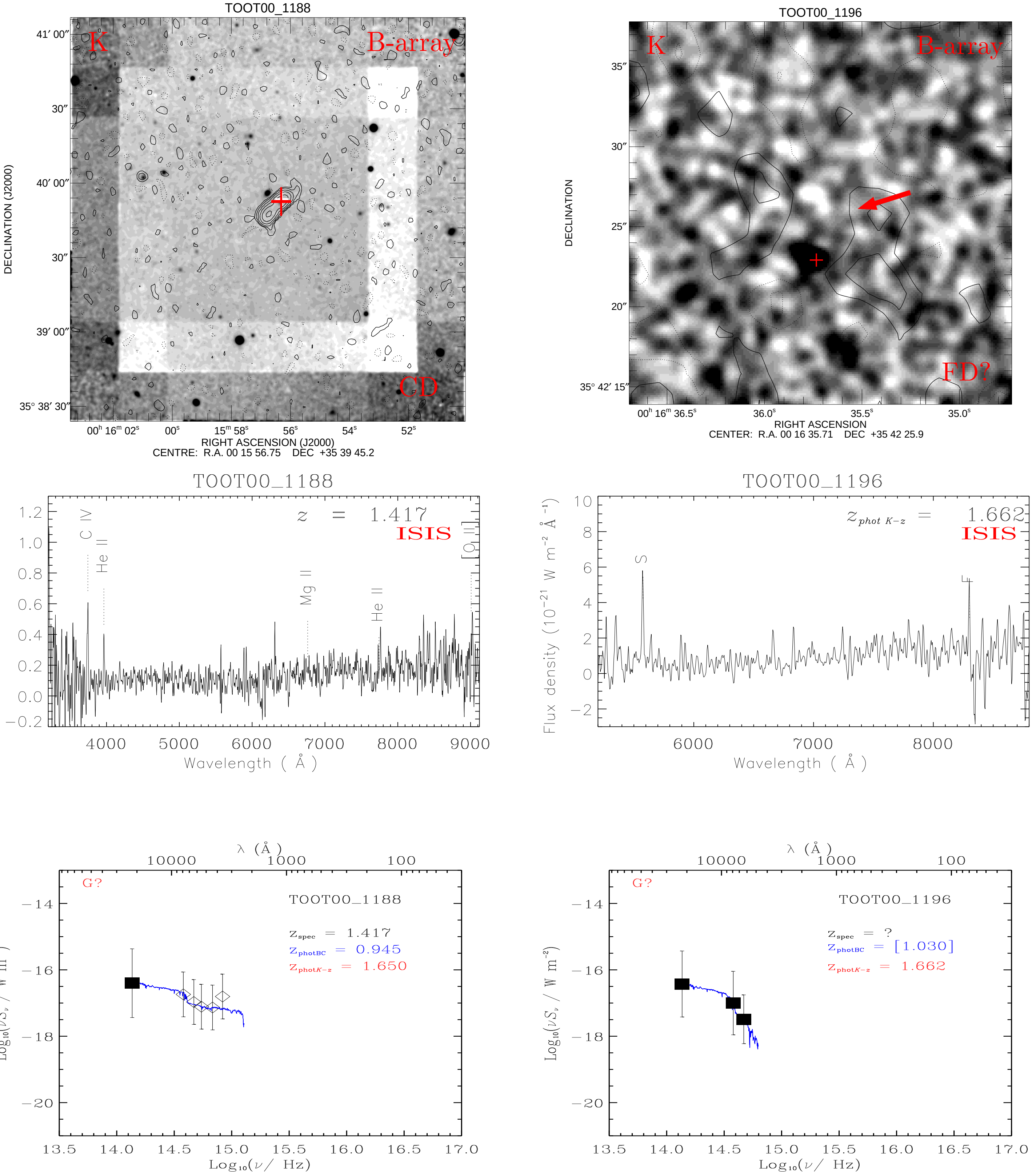

Figure A1. (continued)

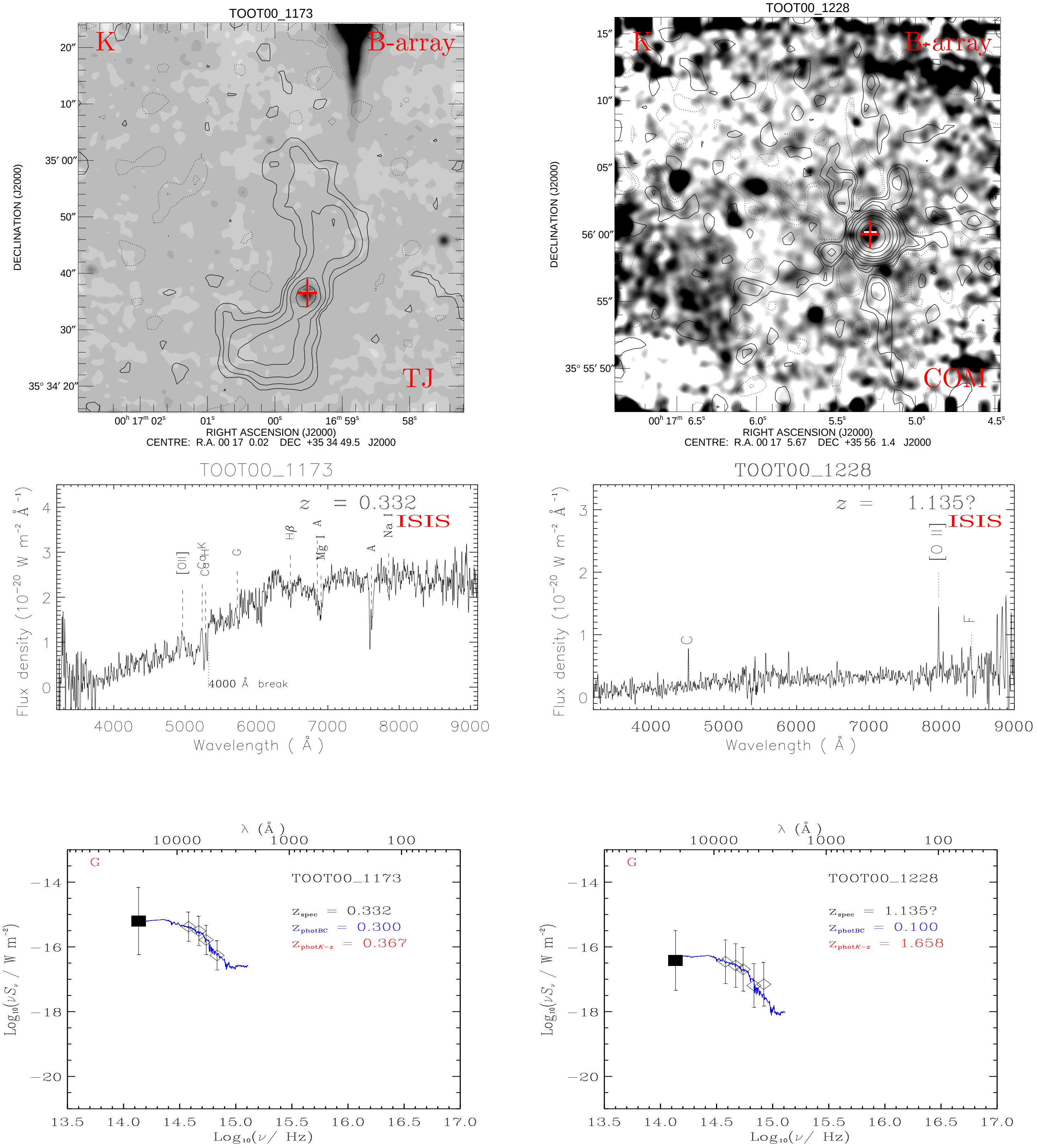

Figure A1. (continued)

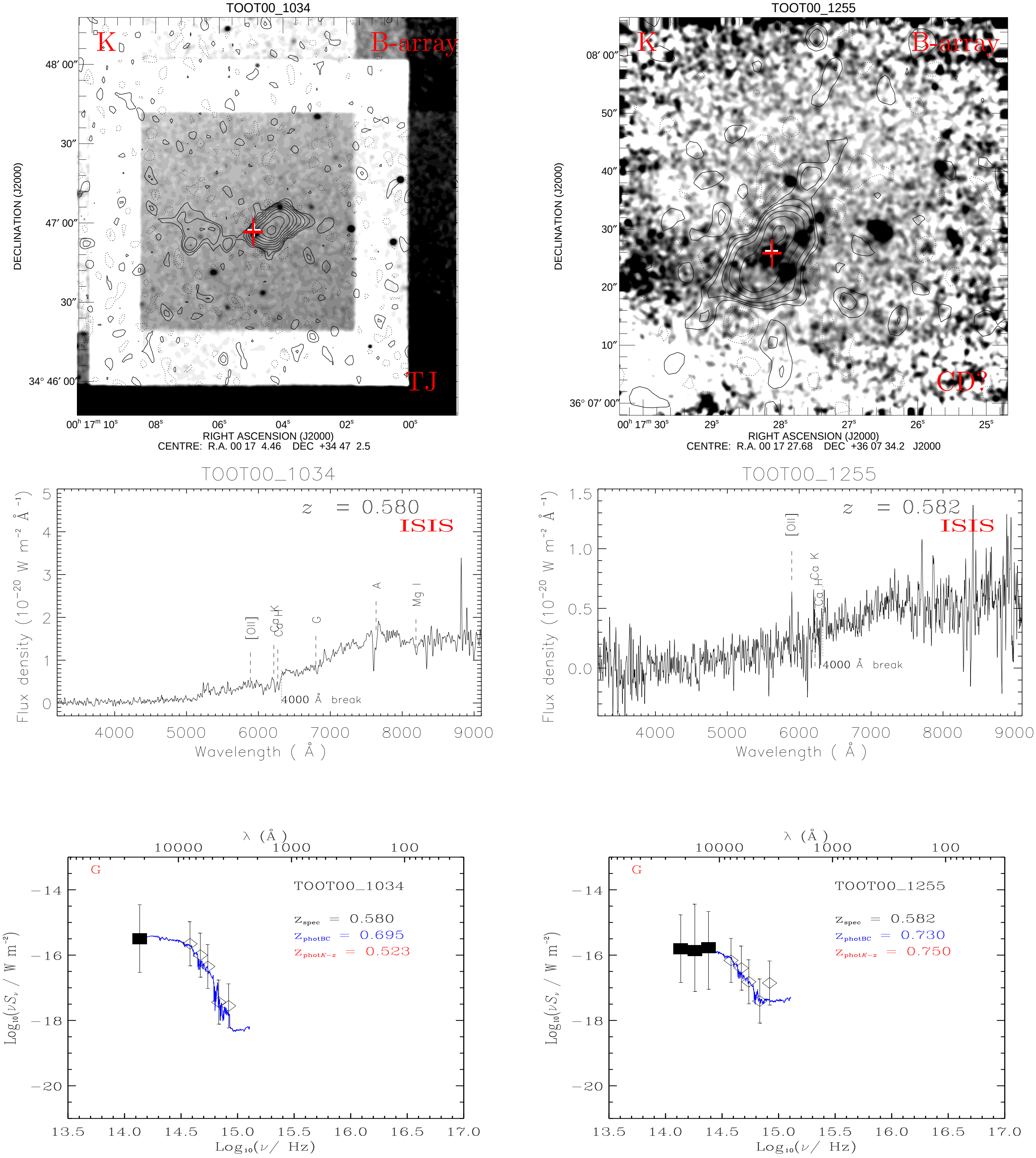

Figure A1. (continued)

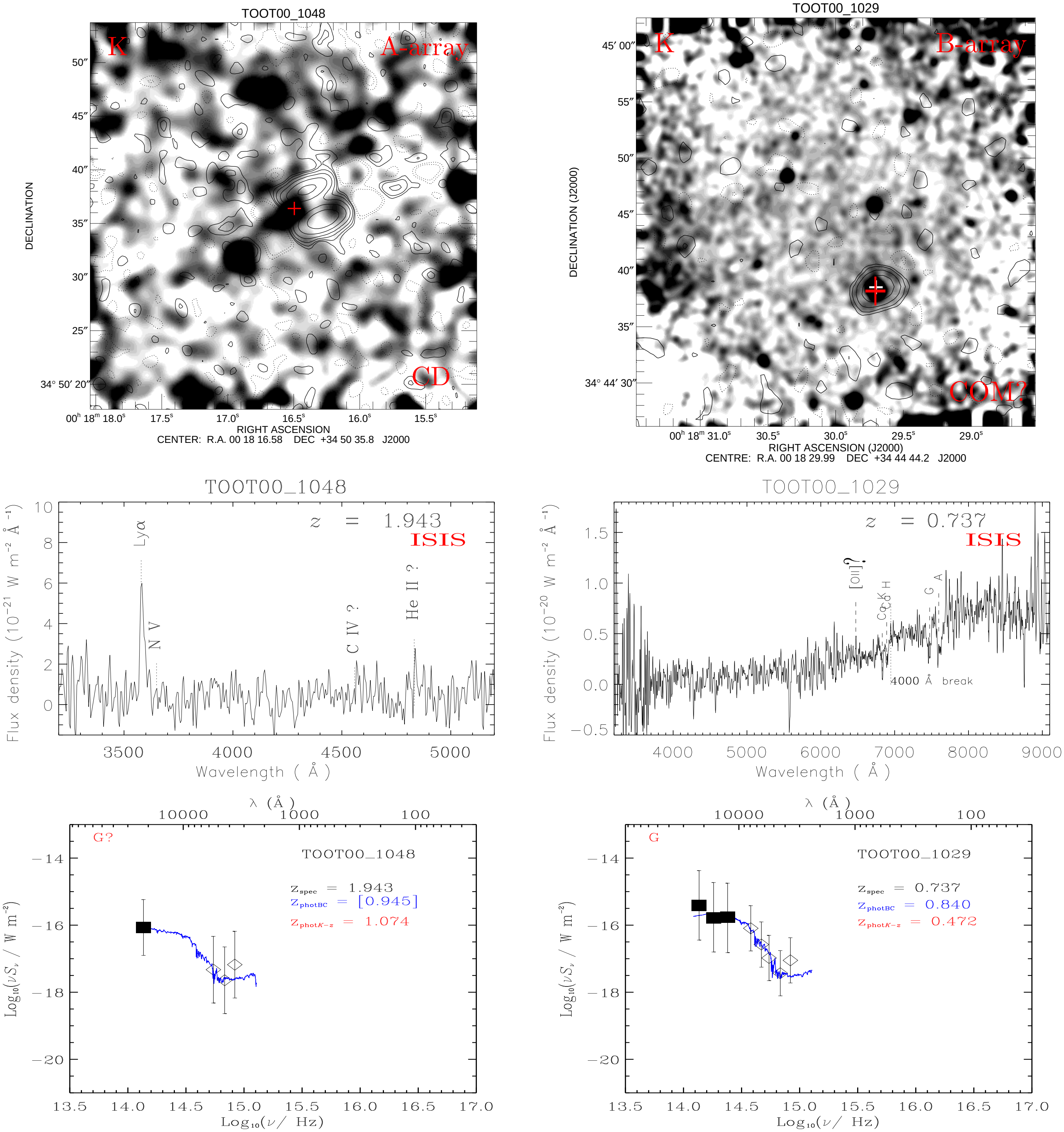

Figure A1. (continued)

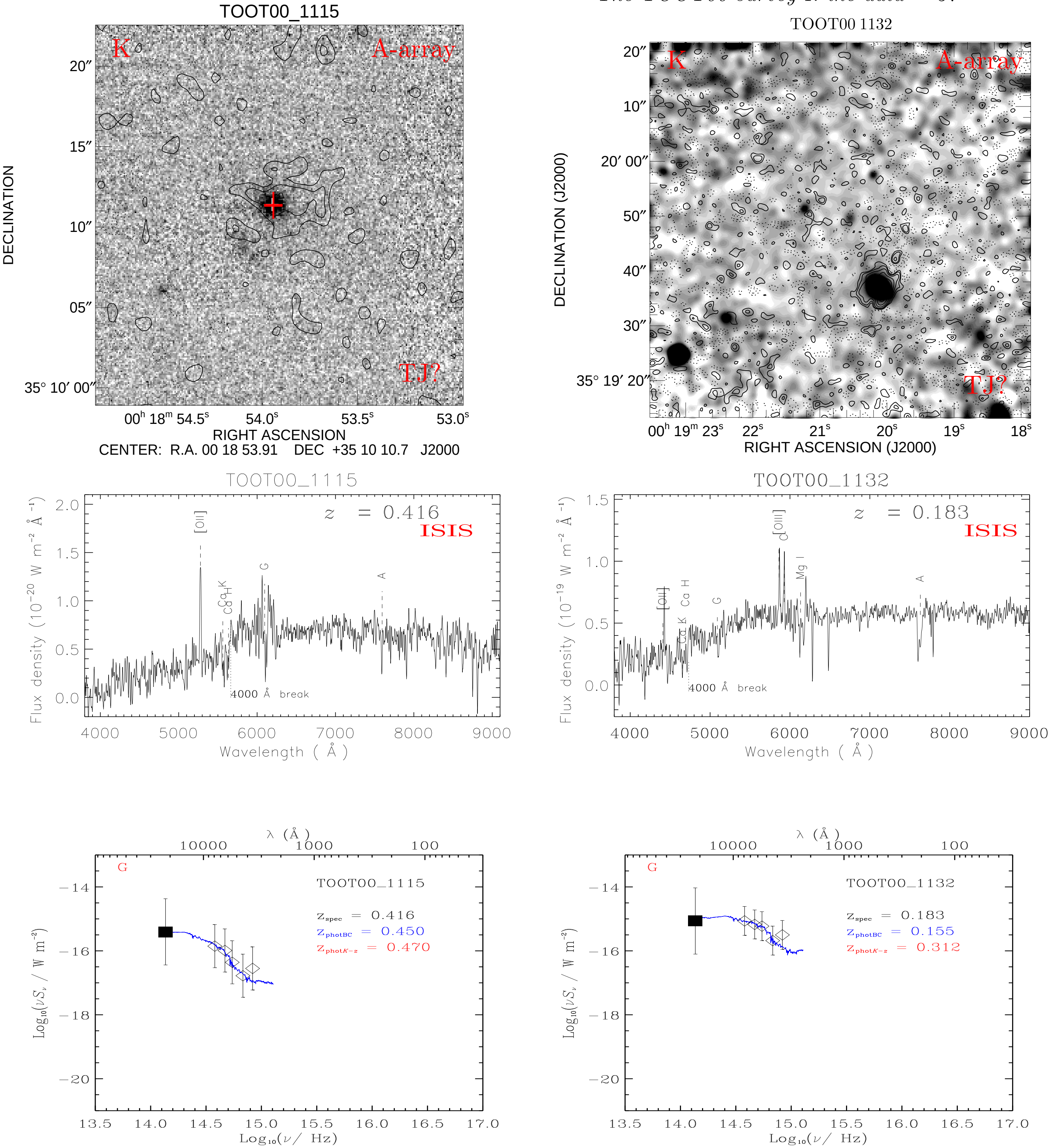

Figure A1. (continued)

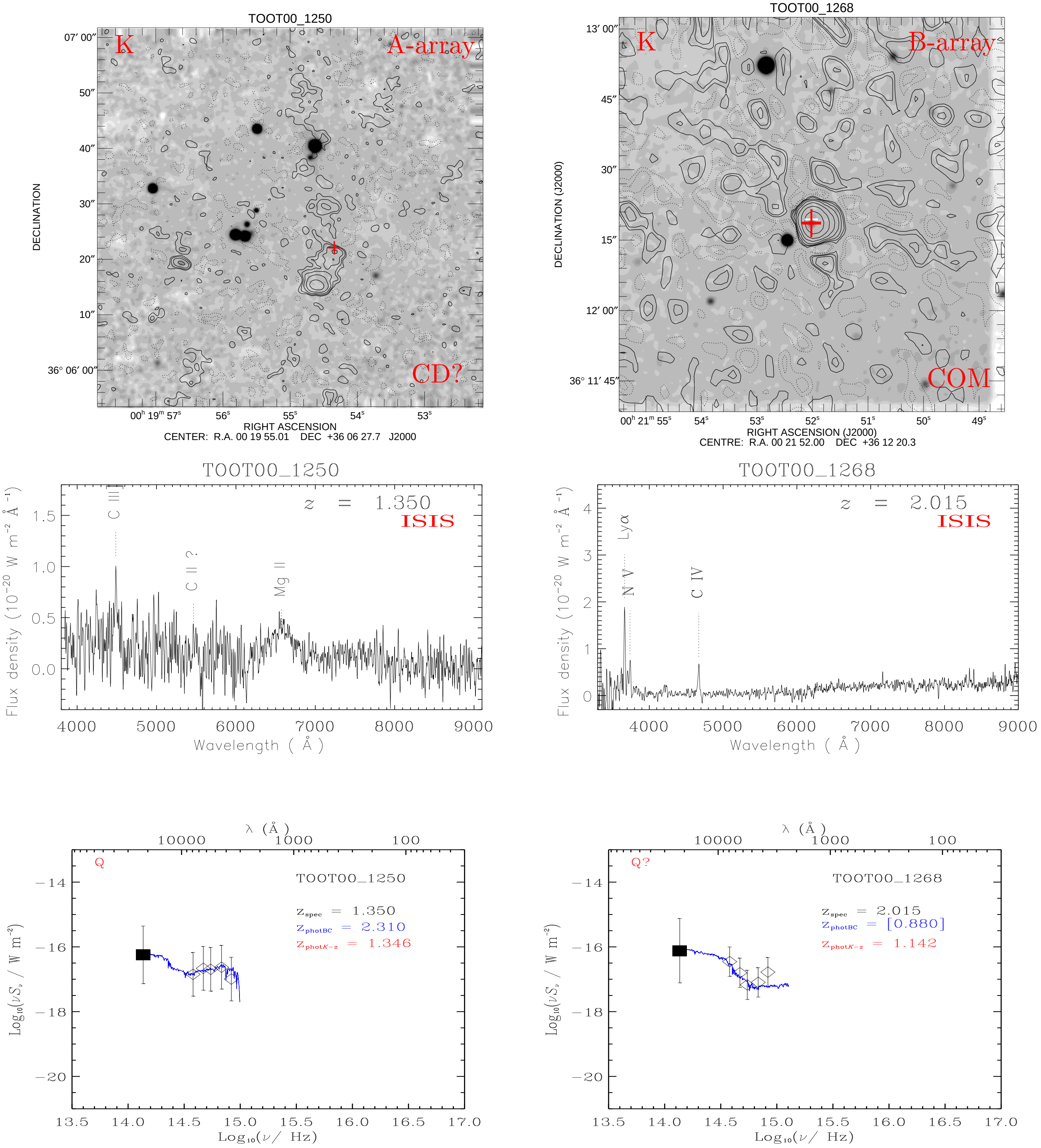

Figure A1. (continued)

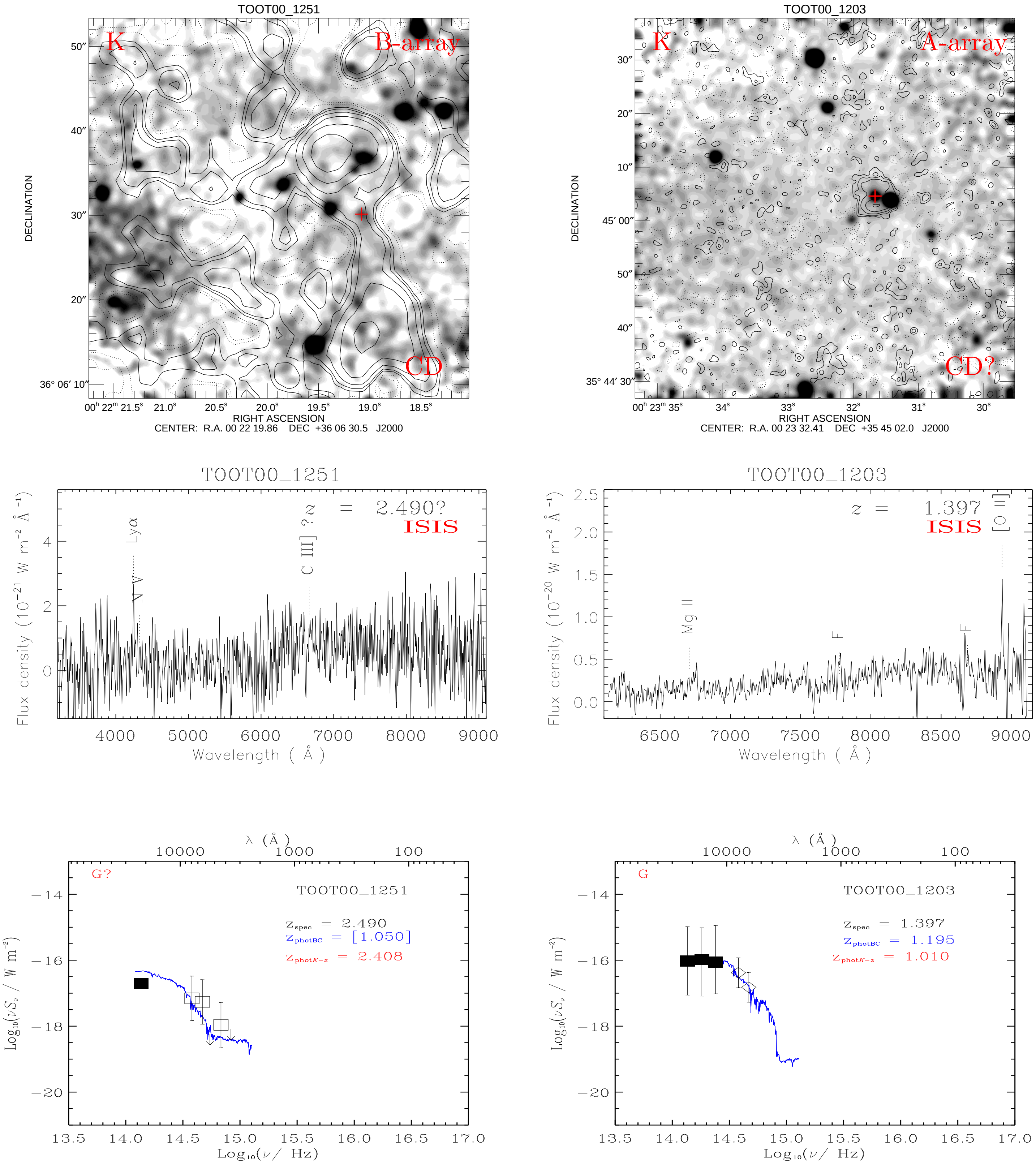

Figure A1. (continued)